

Diploma Thesis

**A Prototype Ion Source  
for the Functionality Test of the  
KATRIN Transport Section**

by Michael Schöppner

August 2008

angefertigt im  
Institut für Kernphysik,  
vorgelegt der  
Mathematisch-Naturwissenschaftlichen Fakultät  
der  
Westfälischen Wilhelms-Universität Münster



---

Ich versichere, dass ich die Arbeit selbständig verfasst und keine anderen als die angegebenen Quellen und Hilfsmittel benutzt, sowie Zitate kenntlich gemacht habe.

Michael Schöppner

Referent: Prof. Dr. C. Weinheimer

Korreferent: Prof. Dr. G. Drexlin

---



# Contents

<b>1</b>	<b>Introduction</b>	<b>11</b>
<b>2</b>	<b>The KATRIN-Experiment</b>	<b>21</b>
2.1	Tritium Beta-Decay . . . . .	21
2.2	Experimental Overview . . . . .	23
2.3	Energy Analysis and Electron Detection . . . . .	24
2.4	Tritium Source . . . . .	27
2.5	Transport Section . . . . .	28
2.5.1	Differential Pumping Section . . . . .	29
2.5.2	Cryogenic Pumping Section . . . . .	29
2.6	Tritium Ions in the KATRIN Source and Transport Section . . . . .	30
2.7	Requirements for the Test Ion Source . . . . .	32
<b>3</b>	<b>Investigation of Possible Ion Sources</b>	<b>35</b>
3.1	Ionization Process . . . . .	35
3.2	Different Methods of Ionization . . . . .	38
3.2.1	Electron Impact Ionization . . . . .	39
3.2.2	Photoionization . . . . .	41
3.2.3	Ion Impact Ionization . . . . .	43
3.3	Determination of Optimum Ion Source . . . . .	44
3.3.1	Electrons from Field and Thermionic Emission . . . . .	45
3.3.2	Electrons from Photoelectrical Effect . . . . .	46
3.3.3	Basic Concept of a Photoelectron Impact Ion Source . . . . .	47
<b>4</b>	<b>Development, Design and Setup of the Prototype Ion Source</b>	<b>49</b>
4.1	Experimental Overview . . . . .	49
4.2	Design Parameters of the Prototype Ion Source . . . . .	52
4.3	Components of the Prototype Ion Source . . . . .	53
4.3.1	UV-Lamp, Window and Photocathode . . . . .	53
4.3.2	Electrode System . . . . .	57
4.3.3	Ion Detection . . . . .	60
4.3.4	Vacuum Setup and Gas Injection . . . . .	61
4.3.5	Design of the Magnet . . . . .	63
4.3.6	Data Acquisition and Slow Control . . . . .	65
4.4	Commissioning . . . . .	66
4.4.1	Vacuum System and Gas Injection . . . . .	66
4.4.2	Magnet Calibration . . . . .	68

*Contents*

<b>5</b>	<b>Measurements and Results</b>	<b>69</b>
5.1	Photoelectron Production . . . . .	69
5.1.1	Experimental Procedure . . . . .	69
5.1.2	Dependencies of Electron Current . . . . .	71
5.2	Ion Production . . . . .	80
5.2.1	Experimental Procedure . . . . .	80
5.2.2	Dependencies of Ion Current . . . . .	82
5.3	Discussion of Measurements . . . . .	92
<b>6</b>	<b>Summary and Outlook</b>	<b>95</b>
	<b>Appendices</b>	<b>99</b>
A:	List of Equipment . . . . .	99
B:	Magnet Calibration . . . . .	100
C:	Flow Diagram of the Prototype Ion Source . . . . .	101
D:	Technical Drawings . . . . .	102
	<b>Bibliography</b>	<b>105</b>
	<b>Acknowledgment (Danksagung)</b>	<b>109</b>

# List of Figures

1.1	The Hierarchical and the Quasi-Degenerated Mass Scale of Neutrinos . . .	15
2.1	Electron Energy Spectrum of the Tritium $\beta$ -Decay . . . . .	22
2.2	Reference design of the KATRIN experiment . . . . .	23
2.3	MAC-E-Filter Principle . . . . .	25
2.4	Schematic Overview of the WGTS . . . . .	27
2.5	The Tritium Related Parts of the KATRIN Experiment . . . . .	29
2.6	Principle of the CPS . . . . .	29
3.1	Electron Impact Ionization Scheme . . . . .	39
3.2	Electron Impact Ionization Cross Section for Deuterium . . . . .	40
3.3	Photoionization Scheme . . . . .	41
3.4	Photoionization Cross Section for Hydrogen . . . . .	42
3.5	Ion Impact Ionization Cross Section for Argon . . . . .	43
3.6	Electron Production Area in a Magnetic Field . . . . .	45
3.7	Principle of Photoelectron Ion Source . . . . .	47
4.1	Gas and Vacuum Setup of the Prototype Ion Source . . . . .	50
4.2	Main Components of the Prototype Ion Source . . . . .	50
4.3	Picture of the Vacuum Chamber of the Prototype Ion Source . . . . .	51
4.4	Picture of the Prototype Ion Source Setup . . . . .	51
4.5	Lot-Oriel Pen-Ray Lamp . . . . .	54
4.6	Quartz Transmission Function . . . . .	56
4.7	Photocathode (Copper) . . . . .	58
4.8	Electrodes . . . . .	59
4.9	Mounted Photocathode and Electrode System . . . . .	59
4.10	Faraday Cup . . . . .	60
4.11	Vacuum Diagram of the Prototype Setup . . . . .	62
4.12	Electrical Feed-Throughs . . . . .	62
4.13	Magnet Coil . . . . .	64
4.14	Map of selected magnetic field lines. . . . .	67
4.15	Calculated Magnetic Field Strength along the Axis of the Coil . . . . .	68
5.1	Standard Potential Distribution for the Electron Production . . . . .	70
5.2	Electron Current over Lamp Intensity . . . . .	73
5.3	Electron Current over Magnetic Field . . . . .	75
5.4	Electron Current over Cathode Potential . . . . .	77

*List of Figures*

5.5	Electron Current over Pressure . . . . .	79
5.6	Standard Potential Distribution for the Electron Production . . . . .	81
5.7	Ion Current over Magnetic Field . . . . .	83
5.8	Ion Current over Electron Extraction Electrode Potential . . . . .	85
5.9	Ion Current over Cylinder Potential . . . . .	86
5.10	Ion Current over Ion Extraction Electrode Potential . . . . .	87
5.11	Ion Current over Pressure . . . . .	89
5.12	Ion Current with and w/o Gas Flow . . . . .	90
6.1	Drawing of Electrode System . . . . .	102
6.2	Drawing of Ion Source . . . . .	103
6.3	Drawing of Ion Source with Magnet . . . . .	104

# List of Tables

1.1	The Twelve Fundamental Fermions of the Standard Model . . . . .	11
4.1	Photocathode Materials . . . . .	57
4.2	Pressure Gauges in the Prototype Ion Source Setup . . . . .	61
5.1	Results of Different Photocathodes . . . . .	71
5.2	Configuration for Electron Current over Lamp Intensity . . . . .	72
5.3	Potential Distribution for Electron Current over Lamp Intensity . . . . .	72
5.4	Configuration for Electron Current over Magnetic Field . . . . .	74
5.5	Potential Distribution for Electron Current over Magnetic Field . . . . .	74
5.6	Configuration for Electron Current over Cathode Potential . . . . .	76
5.7	Potential Distribution for Electron Current over Cathode Potential . . . . .	76
5.8	Configuration for Electron Current over Pressure . . . . .	78
5.9	Potential Distribution for Electron Current over Pressure . . . . .	78
5.10	Configuration for Ion Current over Magnetic Field . . . . .	82
5.11	Potential Distribution for Electron Current over Magnetic Field . . . . .	82
5.12	Configuration for Ion Current over Potential Distribution . . . . .	84
5.13	Potential Distribution for Electron Current over Potential Distribution . . . . .	84
5.14	Configuration for Ion Current over Pressure . . . . .	88
5.15	Potential Distribution for Electron Current over Pressure . . . . .	88

*List of Tables*

# 1 Introduction

Neutrinos are the second most particles in the universe<sup>1</sup>. They are electrically neutral leptons, so that they are influenced neither by electromagnetic interaction nor the strong interaction. They are affected only by the weak interaction and their small cross section makes them experimentally difficult to detect. Therefore, their research is a difficult task, that forms an actual and revolving field of nuclear and astroparticle physics.

In 1930 the neutrino was postulated by Wolfgang Pauli to explain the continuous energy spectrum of the  $\beta$ -decay. This continuous spectrum could not be explained with the model of a two body decay, where the energy and angular momentum conservation would be violated. With the additional particle, the neutrino, the  $\beta$ -decay could be described as a ternary (three-body) reaction and the discrepancy could be solved.

In 1934 the neutrino was included in Fermi's theory of the  $\beta$ -decay as a particle without rest mass. This is still an actual assumption in nowadays V-A-theory of the weak force. The Standard Model of elementary particle physics defines leptons (and quarks) as elementary fermions. The twelve known leptons and quarks are sorted in three families, so that there are three different kinds of neutrinos: the electron neutrino  $\nu_e$ , the myon neutrino  $\nu_\mu$  and the tau neutrino  $\nu_\tau$  [Yao06]. They are named after their partners in charged currents of the weak interaction: the electron  $e$ , the myon  $\mu$  and the tauon  $\tau$ . The classification of the twelve fundamental fermions is shown in Table 1.1. In the Standard Model of particle physics every fermion has an anti-fermion with the same mass, but opposite charge, color and third component of the weak isospin.

In 1956 neutrinos were detected experimentally for the first time. Reines and Cowan proved the existence of the electron anti-neutrinos from the inverse  $\beta$ -decay in a reactor [Rei59]:

$$\bar{\nu}_e + p \rightarrow n + e^+ \tag{1.1}$$

---

<sup>1</sup>The number of neutrinos is  $10^9$  times higher than the number of baryons. Only photons are more frequent.

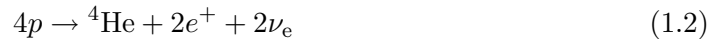
**Table 1.1: The twelve fundamental fermions of the standard model.** Sorted with increasing mass of the charged leptons.

<b>Family:</b>	<b>1</b>	<b>2</b>	<b>3</b>
Leptons:	$\begin{pmatrix} \nu_e \\ e^- \end{pmatrix}$	$\begin{pmatrix} \nu_\mu \\ \mu^- \end{pmatrix}$	$\begin{pmatrix} \nu_\tau \\ \tau^- \end{pmatrix}$
Quarks:	$\begin{pmatrix} u \\ d \end{pmatrix}$	$\begin{pmatrix} c \\ s \end{pmatrix}$	$\begin{pmatrix} t \\ b \end{pmatrix}$

## 1 Introduction

Originally the standard model of particle physics defined the neutrino as a particle without rest mass, because the experimental data was congruent with that. But during the last years experimental results gave rise to a non-vanishing neutrino mass. This will be explained in the following.

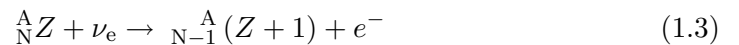
Neutrino sources are found for example in atmospheric reactions, supernovas and suns, but also in reactors and accelerators. Solar neutrinos are generated in thermonuclear fusion processes in the sun. Hydrogen becomes helium, which is shown in the following net reaction [Sch97]:



This reaction creates only electron neutrinos. Solar neutrinos are originating from the core of the sun, where the fusion takes place. Due to their extreme small cross section, they can leave the sun almost undisturbed. But the measured flow rates of electron neutrinos have been smaller than it was expected from the calculations from the standard model of the sun.

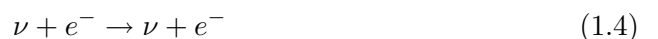
The following experiments aimed for the measurement of solar neutrinos:

- The Homestake experiment, the Gallex<sup>2</sup>/GNO experiment and the SAGE<sup>3</sup> experiment used radiochemical methods for the detection of neutrinos. With the used neutrino capture reaction only electron neutrinos could be detected:



The Homestake experiment used  ${}^{37}\text{Cl}$ , the Gallex/GNO and the SAGE experiment used  ${}^{71}\text{Ga}$  as a target. In all of these experiments the measured solar neutrino flow rates were smaller than the expected value by a factor of 2-3 [Dav94, Ham99, Abd04].

- The Kamiokande experiments (Kamiokande I-III and Super-Kamiokande) used the elastic neutrino scattering on electrons for the detection of all three kinds of neutrinos:



The cross sections for the elastic scattering of myon and tau neutrinos on electrons are smaller by a factor of seven than the according cross section of electron neutrinos. Therefore, the detection of electron neutrinos outweigh the other two neutrino kinds. The detection is done by photomultipliers surrounding a water basin. Inside of the water the hitted electrons can emit Cerenkov light, which can be detected by the photomultipliers. With this method the energy and direction of the detected neutrinos can be reconstructed. Therefore, neutrinos of solar origin can be distinguished. The measured flow rate of solar electron neutrinos amounts only to 40 % of the expected flow rate.

---

<sup>2</sup>Gallium Experiment,

<sup>3</sup>Soviet American Gallium Experiment

The following experiment aimed for the measurement of reactor neutrinos:

- The KamLAND<sup>4</sup> experiment detects electron anti-neutrinos from the inverse  $\beta$ -decay:



The measured flow rate of electron anti-neutrinos from the KamLAND experiment is also below the expected flow rate [Egu04].

This deficit in the flow rate of (solar) electron neutrinos can be explained with neutrino flavor oscillation. If the neutrinos would oscillate, at least one rest mass would be non-vanishing. E.g. on its way from the sun to the earth an electron neutrino could be transformed into a myon neutrino. This idea of neutrino oscillation origins in 1958 and was developed from Pontecorvo. In 2001 the SNO experiment could support this model:

- The Sudbury Neutrino Observatory SNO experiment uses heavy water  $D_2O$  to detect neutrinos from three different reactions.

1. Elastic scattering of neutrinos on electrons (cp. Kamiokande experiment):



Due to the smaller cross sections of myon and tau neutrinos, this reaction is preferred to detect electron neutrinos. The measurements of this reaction also showed a deficit in solar electron neutrinos in consistence with the Super-Kamiokande results.

2. Charged currents:



This reaction is only possible with electron neutrinos. Therefore it also detected the deficit in the flow rate of solar electron neutrinos.

3. Neutral currents:



This reaction is sensitive to all three kinds of neutrinos. The measured total flow rate of solar neutrinos is congruent to the prediction from the standard model of the sun.

The combination of these results from the SNO experiment is taken as a evidence, that neutrino oscillations exist [SNO02].

Neutrino oscillations are only possible, if all three kinds of neutrinos have different masses, i.e. have a rest mass. The model of neutrino oscillation can be explained with the superposition of three different mass eigenstates. This means that the three flavor

---

<sup>4</sup>Kamioka Liquid Scintillator Anti Neutrino Detector

## 1 Introduction

eigenstates  $|\nu_\alpha\rangle$  with  $\alpha = e, \mu, \tau$  are not identical with the three mass eigenstates  $|\nu_i\rangle$  with  $i = 1, 2, 3$ . Instead they are coupled by the unitary transformation

$$|\nu_\alpha\rangle = \sum_i U_{\alpha i}^* |\nu_i\rangle \quad (1.9)$$

and respectively

$$|\nu_i\rangle = \sum_\alpha U_{\alpha i} |\nu_\alpha\rangle \quad (1.10)$$

The unitary matrix  $U$  causes a superposition of the three mass eigenstates to create the three neutrino flavors. The time dependency of the mass eigenstates  $\nu_i$  is given by the multiplication with the time development operator:

$$|\nu_i(t)\rangle = e^{-iE_i t/\hbar} |\nu_i\rangle \quad (1.11)$$

with the energy

$$E_i = \sqrt{p^2 c^2 + m_i^2 c^4} \quad (1.12)$$

The transition probability  $P$  from one flavor  $|\nu_\alpha\rangle$  into another  $|\nu_\beta\rangle$  is given by

$$P(\alpha \rightarrow \beta, t) = |\langle \nu_\beta | \nu(t) \rangle|^2 \quad (1.13)$$

$$= \sum_i |U_{\alpha i} U_{\beta i}^*|^2 + 2 \cdot \text{Re} \sum_{k>i} U_{\alpha i} U_{\alpha k}^* U_{\beta i}^* U_{\beta k} e^{-i(E_i - E_k)t/\hbar} \quad (1.14)$$

The first term contains the average transition probability, the second term contains the time-dependent transition probability.

Solar neutrinos  $\nu_e$  can oscillate into another flavor  $\nu_x$  with  $\nu_x$  being a linear combination of  $\nu_\mu$  and  $\nu_\tau$ . For the simplification of only two neutrino flavors, e.g.  $\nu_e$  and  $\nu_\mu$ , the superposition of mass eigenstates can be written as

$$\begin{pmatrix} \nu_e \\ \nu_\mu \end{pmatrix} = \begin{pmatrix} \cos \theta & \sin \theta \\ -\sin \theta & \cos \theta \end{pmatrix} \begin{pmatrix} \nu_1 \\ \nu_2 \end{pmatrix} \quad (1.15)$$

with the mixing angle  $\theta$ . And respectively the mass eigenstates can be written as a superposition of flavor eigenstates:

$$\begin{pmatrix} \nu_1 \\ \nu_2 \end{pmatrix} = \begin{pmatrix} \cos \theta & -\sin \theta \\ \sin \theta & \cos \theta \end{pmatrix} \begin{pmatrix} \nu_e \\ \nu_\mu \end{pmatrix} \quad (1.16)$$

Then the probability  $P$  to find a neutrino  $\nu_e$  of the energy  $E$  in a distance  $L$  as a neutrino  $\nu_\mu$  is given by:

$$P(\nu_e \rightarrow \nu_\mu, L) = \sin^2 2\theta \cdot \sin^2 \left( \frac{\Delta m^2 L}{4E} \right) \quad (1.17)$$

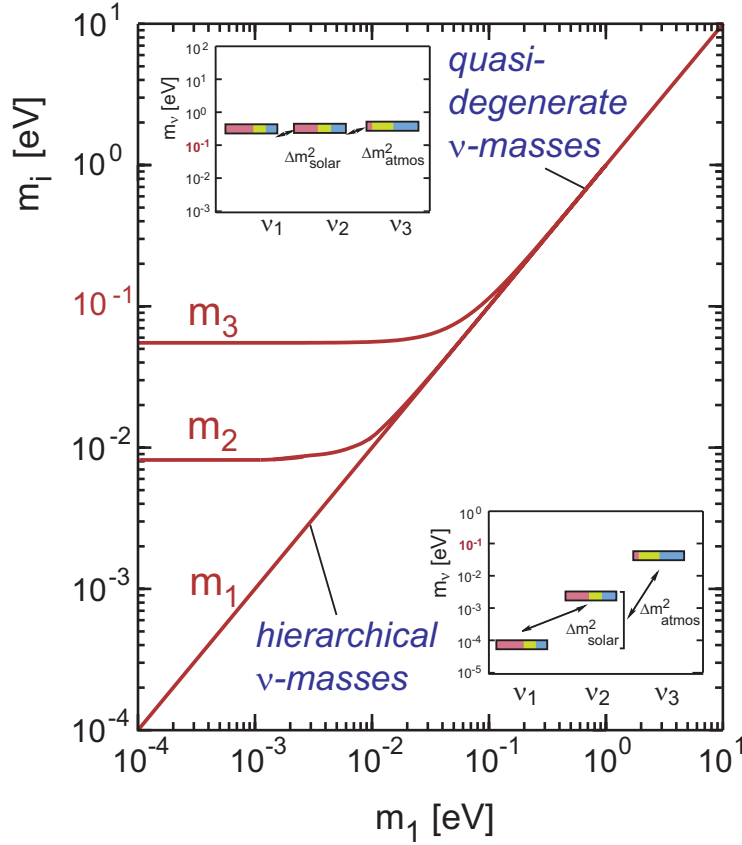


**Figure 1.1: The hierarchical and the quasi-degenerated mass scale of neutrinos.** [KAT04] The figure shows the three neutrino masses  $m_i$  ( $i = 1, 2, 3$ ) as functions of the lowest mass eigenstate  $m_1$ .

Neutrino oscillation experiments can not determine the absolute mass of the neutrinos, but only the difference of the squared masses  $\Delta m^2 = |m_i^2 - m_j^2|$  from Equation 1.17. In case of matter effects (e.g. solar neutrinos) the hierarchy of  $m_i$  and  $m_j$  can be resolved. The results from the above mentioned solar and reactor neutrino experiments lead to a difference of the squared masses for the oscillation  $\nu_e \rightarrow \nu_{\mu,\tau}$  [Eid04]:

$$\Delta m_{\text{solar/react}}^2 = (8.0_{-0.4}^{+0.6}) \cdot 10^{-5} \text{ eV}^2/c^4 \quad (1.18)$$

Furthermore, the Super-Kamiokande experiment determined the difference of the squared masses for the oscillation  $\nu_{\mu} \rightarrow \nu_{\tau}$  [Eid04]:

$$1.9 \cdot 10^{-3} \text{ eV}^2/c^4 < \Delta m_{\text{atmos}}^2 < 3.0 \cdot 10^{-3} \text{ eV}^2/c^4 \quad (1.19)$$

## 1 Introduction

The theory of the generation of neutrino masses leads to two different scenarios (see also Figure 1.1):

- The hierarchical composition of the neutrino masses: The three masses are below  $0.1 \text{ eV}/c^2$  and are different from each other  $m_1 \ll m_2 \ll m_3$  or  $m_1 \leq m_2 \ll m_3$  [Gel79, Yan78].
- The quasi-degenerated composition of the neutrino masses: The three masses are in the range of  $0.1 - 2 \text{ eV}/c^2$  and similar to each other  $m_1 \approx m_2 \approx m_3$  [Rab97, Moh02].

The determination of the absolute mass scale of the neutrinos is of interest not only for particle physics, but also in cosmology. The big bang generated among other particles photons and neutrinos. The photons from the big bang can still be measured nowadays as the 2.7 K background radiation [Fuk06]. Those relic neutrinos from the big bang also still exist. Today the relic neutrinos have a temperature of  $T_{\nu 0} \approx 1.95 \text{ K}$ . Their particle density is estimated to be  $334 / \text{cm}^3$ . Therefore, the number of neutrinos in the universe is  $10^9$  higher than the number of baryons. Due to their low energy their cross section is extreme small ( $\sigma \approx 10^{-54} \text{ cm}^2$ ). Therefore, their detection is not possible yet.

Since the discovery of dark matter the question of its composition is unsolved. Dependent on their absolute mass the neutrinos could contribute to the total mass of dark matter with a factor between  $0.2 - 10 \%$  [Han04]. This is important for the development of the universe and its structure. Therefore, the knowledge of the absolute neutrino mass is important for cosmology and astroparticle physics.

In general the determination of the absolute neutrino mass can be done in two different ways. The indirect methods are model-dependent, i.e. the result is valid for the used model. The direct methods are model-independent, i.e. they need no further assumptions.

The indirect methods are:

- Cosmological estimations: Through cosmological observations the absolute neutrino mass can be estimated. Massive neutrinos influence for example the formation of galaxy structures and also the 2.7 K background radiation. The determination of the absolute neutrino mass from cosmological observation is sensitive, but also strongly model-dependent. The upper limit for the sum of all three masses is  $\sum_i m_i < (0.7 - 2) \text{ eV}/c^2$ . [Han06]
- Neutrinoless double- $\beta$ -decay: It is possible that two  $\beta$ -decays in one nucleus happen at the same time, i.e. a  $\beta^- \beta^-$ -decay or a  $\beta^+ \beta^+$ -decay. In the following the  $\beta^- \beta^-$ -decay is taken as an example:

$$(A, Z) \rightarrow (A, Z + 2) + 2e^- + 2\bar{\nu}_e \quad (1.20)$$

In a neutrinoless  $\beta^- \beta^-$ -decay ( $0\nu\beta\beta$ ) the two anti-neutrinos would not be emitted, but exchanged between the decay points as virtual particles.

This is only possible, if

1. neutrinos are majorana particles, i.e. particle and anti-particle are identical, which is possible for a neutral particle like the neutrino.
2. the emitted neutrinos have a mixed helicity. This is, because the neutrino, that is emitted as a left handed particle, must be absorbed as a right handed particle. A mixed helicity of the neutrinos is only possible with massive neutrinos (or the admixture of right-hand weak charged currents).

If the  $0\nu\beta\beta$ -decay can be detected, it is possible to calculate the neutrino mass from the known nucleus matrix element and the measured half life of the  $\beta$ -decay. If the  $0\nu\beta\beta$ -decay can not be detected, it is still possible to determine an upper limit for the neutrino mass<sup>5</sup>. The Heidelberg-Moscow experiment published their successful detection of the  $0\nu\beta\beta$ -decay from the  $^{76}\text{Ge}$ -decay:



There is an unconfirmed claim by a part of the collaboration [Kla04] of a positive  $0\nu\beta\beta$ -detection and a neutrino mass of:

$$m_{\nu_e} = 0.39 \text{ eV}/c^2 \quad (1.22)$$

This result is controversial and could not be confirmed from other experiments. Upcoming experiments like GERDA and EXO-200 want to verify these results.

The direct methods are:

- Time of flight (ToF): It is possible to measure the time, that a neutrino of a certain energy needs for an certain path length. From this measurement the mass of the neutrino can be calculated with the relativistic energy-momentum relation:

$$E^2 = p^2c^2 + m^2c^4 \quad (1.23)$$

A time of flight measurement could be accomplished for the first time with the supernova SN1987A. From this an upper limit of the electron neutrino could be determined [Yao06]:

$$m_{\nu_e} < 5.7 \text{ eV}/c^2 \quad (1.24)$$

- Measurements of the kinematics of weak decays: These methods do not detect the neutrinos themselves, but the decay products of a neutrino-emitting, weak decay. The energy- and momentum-conversion give a possibility to calculate the neutrino mass from the measurements of the decay products. It is the most sensitive direct method to determine the absolute neutrino mass. (In fact the three neutrino

---

<sup>5</sup>Only with the assumption, that neutrinos are majorana particles.

## 1 Introduction

masses are mixed from the three mass eigenstates.) The masses of all three different neutrino flavors have been examined:

- Tau neutrino mass: Tau pairs are produced at  $e^+e^-$ -colliders and the decays are examined. If many pions are created, the kinetic energy of the tau neutrino is small. Then the rest mass of the neutrino can be determined from the detection of the pions:

$$\begin{aligned}\tau^- &\rightarrow \pi^- \pi^- \pi^- \pi^+ \pi^+ (\pi^0) + \nu_\tau \\ \tau^+ &\rightarrow \pi^+ \pi^+ \pi^+ \pi^- \pi^- (\pi^0) + \bar{\nu}_\tau\end{aligned}\quad (1.25)$$

The actual upper limit for the mass of the tau neutrino is [Bar98]

$$m_{\nu_\tau} < 18.2 \text{ MeV}/c^2 \quad (1.26)$$

- Myon neutrino mass: With the pion decay it is possible to determine the mass of the myon neutrino.

$$\begin{aligned}\pi^- &\rightarrow \mu^- + \bar{\nu}_\mu \\ \pi^+ &\rightarrow \mu^+ + \nu_\mu\end{aligned}\quad (1.27)$$

From measurements of the mass of the pion and of the mass and momentum of the myon it is possible to determine the upper limit of the myon neutrino mass [PDG04]:

$$m_{\nu_\mu} < 190 \text{ keV}/c^2 \quad (1.28)$$

- Electron anti-neutrino mass: From the tritium  $\beta$ -decay a helium atom, an electron and an electron anti-neutrino are emitted:

$${}^3\text{H} \rightarrow {}^3\text{He} + e^- + \bar{\nu}_e \quad (1.29)$$

If the endpoint region of the spectrum of the decay electrons is precisely measured, the electron anti-neutrino mass can be calculated. The most sensitive measurements of  $m_{\nu_e}$  is reached with spectrometers of the MAC-E filter principle. The actual upper limit of the electron anti-neutrino mass was determined in the experiments in Mainz and Troitsk [Bo07a]:

$$m_{\nu_e} < 2.3 \text{ eV}/c^2 \quad (1.30)$$

Due to the results from the neutrino oscillation experiments, it is sufficient to determine the neutrino mass of one flavor. Then the absolute mass scale with the other two masses is also determined. Since the mass of the electron neutrino has been narrowed to the eV-range, tritium  $\beta$ -decay experiments offer a higher sensitivity than other experiments, that determine the mass of the myon or tau neutrino.

The experiments in Mainz and Troitsk reached their maximum sensitivity. The results from cosmological observations (WMAP etc.) and from the  $0\nu\beta\beta$ -experiments reveal, that the next generation of tritium  $\beta$ -decay experiments needs a sensitivity in the sub-eV range.

The present diploma thesis has been accomplished for the KATRIN experiment, a next generation tritium decay experiment to determine the electron anti-neutrino mass with a sub-eV sensitivity. It is build up by an international collaboration at Forschungszentrum Karlsruhe. The sensitivity improvement of one order of magnitude will be achieved by a much stronger windowless gaseous tritium source and a large electron spectrometer of the MAC-E filter type. In the KATRIN experiment the tritium flow rate from the tritium source into the spectrometer has to be reduced to minimize the background. The necessary reduction of the tritium flow rate is achieved in the transport section.

However, one has to distinguish between neutral tritium and charged tritium. The tritium ions are bound to a strong axial magnetic field and cannot be removed by active pumping. It is planned to install diagnostic tools to measure the ion flow rate and to remove the ions from the beamline by appropriate electromagnetic fields. These mechanisms have to be tested before their application during the tritium operation. Therefore, an ion source is necessary for the test experiments at the KATRIN transport section. The present thesis treats the development, design and test of this ion source.

The thesis is structured as follows:

- In Chapter 2 the KATRIN experiment is introduced in detail. This leads to the determination of the requirements of the test ion source.
- In Chapter 3 different ionization principles are examined to evaluate the optimum method for the test ion source. This leads to the principle design of the test ion source and shows that a prototype is needed.
- In Chapter 4 the chosen design is outlined. This includes the design of the prototype ion source, the vacuum system and a magnetic coil.
- In Chapter 5 the results from the measurements are presented and discussed.
- In Chapter 6 the presented work is summarized and an outlook for the test ion source is given.
- The Appendix contains a list of the used equipment, calibration measurements and technical diagrams and sketches.

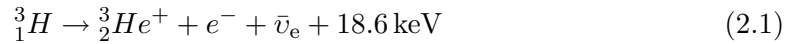
## *1 Introduction*

## 2 The KATRIN-Experiment

This chapter will explain the physical background of the KATRIN components and their relevance to the present thesis. Therefore, the level of detail is biased to certain parts of the experiment, namely the tritium source and the transport section. The requirements for the test ion source are summarized in Section 2.7. Further information about KATRIN can be found in the Design Report [KAT04].

### 2.1 Tritium Beta-Decay

The KATRIN-Experiment is based on the spectroscopy of the radioactive decay of tritium. One tritium atom consists of one proton and two neutrons. It is the heaviest isotope of hydrogen and decays via  $\beta^-$ -decay. In  $\beta^-$ -decay one neutron is converted into a proton and tritium becomes helium-3. Charge conservation dictates the generation of an electron, which is being emitted together with an electron-anti-neutrino<sup>1</sup>.



The decay energy of 18.6 keV is distributed to the neutrino, the electron and the new nucleus. It is also the maximum energy, that the electron can receive, i.e. the endpoint energy of the electron's continuous spectrum. The mass of helium-3 (3 u) is high compared to the masses of the electron and the neutrino. Therefore the variation in its recoil momentum is only about 6 meV in a region of 50 eV around the endpoint energy of the electron [KAT04]. Hence, it can be neglected in the present calculations and it is assumed that the two leptons receive all energy from the decay. The shape of the electron energy spectrum is given by Fermi's Golden Rule [Alt03]:

$$\frac{d^2N}{dt dE} = A \cdot F(E, Z + 1) p(E + m_e) (E_0 - E) \sqrt{(E_0 - E)^2 - m_\nu^2} \Theta(E_0 - E - m_\nu) \quad (2.2)$$

With the speed of light  $c = 1$  and the following notation:

$E$	Kinetic energy of the electron
$p$	Momentum of the electron
$m_\nu$	Mass of the electron anti-neutrino <sup>2</sup>

---

<sup>1</sup>From now on the electron-anti-neutrino will be called neutrino, where confusion is excluded.

<sup>2</sup>Instead of  $m_{\bar{\nu}_e}$  the mass of the electron anti-neutrino is shortened to  $m_\nu$ , because particle and anti-particle have the same mass.

## 2 The KATRIN-Experiment

$E_0$	Endpoint energy of the spectrum
$F$	Fermi-function with the atomic number of the product ( $Z + 1$ ), for the coulomb interaction of the electrons in the final state
$\Theta$	Step function for the case, that the available energy is smaller than the neutrino's rest mass <sup>3</sup> .

$A$  Constant, with

$$A = \frac{G_F^2}{2\pi^3 \hbar^7} \cos^2 \theta_C |\mathcal{M}_{\text{had}}^2|$$

and

$G_F$  Fermi-Constant

$\theta_C$  Cabibbo-Angle

$\mathcal{M}_{\text{had}}$  Hadronic Element of the Transition matrix

As seen in Equation 2.2 the shape of the electron spectrum contains information about the mass of the neutrino. The neutrino mass  $m_\nu$  has no influence on  $\mathcal{M}$  and  $F$ ; it changes the shape of the  $\beta^-$ -spectrum only by the phase space factor. The impact of different neutrino masses on the spectrum is shown in Figure 2.1. If the shape in the endpoint region is adequately known, the calculation of the neutrino mass will be possible. The count rate in the endpoint region is very small; for tritium only  $\approx 2 \cdot 10^{-13}$  of all  $\beta^-$ -decays are in the range of 1 eV below the endpoint [KAT04].

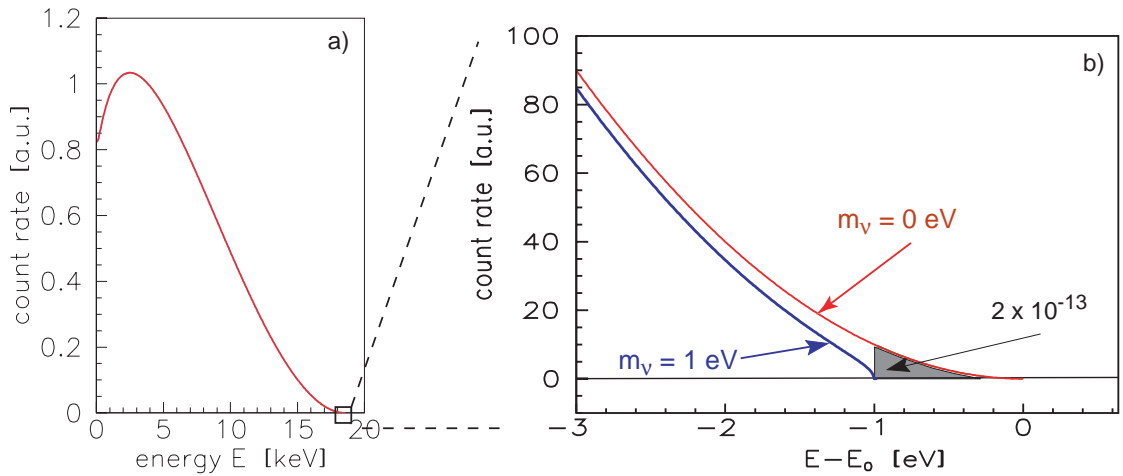


**Figure 2.1: Electron energy spectrum.** [KAT04] Part (a) shows the complete spectrum of the tritium  $\beta^-$ -decay. Part (b) zooms in on the endpoint region. The difference in the shape of the  $\beta^-$ -spectrum is shown for different neutrino masses.

<sup>3</sup>A neutrino can only be created from  $\beta$ -decay when there is enough energy left for its rest mass.

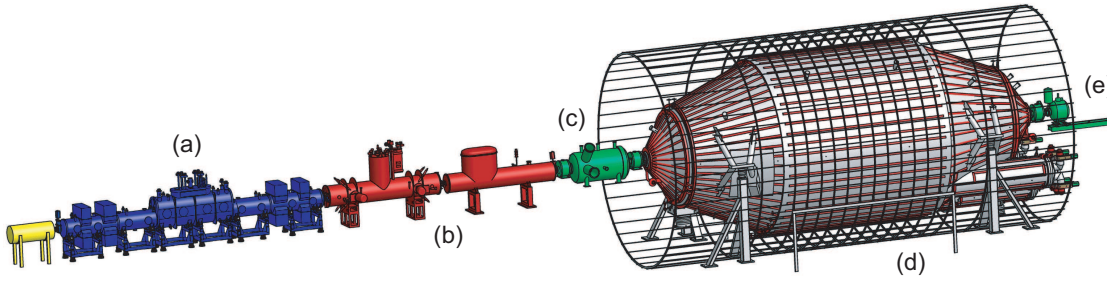


**Figure 2.2: Reference design of the KATRIN experiment.** [Thü07] The figure shows the overview of the KATRIN beamline:

- (a) tritium source
- (b) transport section
- (c) pre-spectrometer
- (d) main-spectrometer
- (e) detector

## 2.2 Experimental Overview

The aim of any tritium decay experiment is to have a tritium source with a high specific activity as well as a spectrometer with a high energy resolution. A strong source results in low statistical uncertainties. Then the slope of the spectrum's endpoint can be precisely measured and the neutrino mass calculated. The advantages of tritium as source material are:

- It has the second lowest endpoint energy (18.575 keV), which means that the relative difference in the neutrino mass sensitive region is large.
- It has only one shell electron, which simplifies the calculation of the final states.
- The half-life is only 12.3 years, so that high count rates can be achieved with relatively low source densities.

The principal design of the KATRIN experiment contains four basic elements. Gaseous tritium is inserted into the *source*, where it decays. The  $\beta^-$ -electrons are guided through the *transport section*, where the tritium is actively removed in order to prevent it from entering the spectrometer section. The *tandem-spectrometer* is a two stage high pass filter, that sorts out all electrons with an energy below an adjusted threshold. At the end of the beamline the *detector* counts all electrons, that passed the energy filter. By varying the high pass threshold the whole  $\beta^-$ -spectrum can be scanned and an integrated spectrum is acquired. The requirements for a high sensitivity are a high resolution in the tandem-spectrometer as well as a low background.

The last generation of tritium decay experiments were conducted in Troitsk and Mainz. There an upper limit of the neutrino mass was determined; the Troitsk experiment found  $m_\nu \leq 2.5$  eV and accordingly in Mainz  $m_\nu \leq 2.3$  eV [Bo07a]. KATRIN will improve

the sensitivity of its predecessor experiments by one order of magnitude<sup>4</sup> and reach a sensitivity of 0.2 eV in the determination of the electron neutrino mass.

### 2.3 Energy Analysis and Electron Detection

The KATRIN experiment uses a pre- and a main-spectrometer as an energetic filter and a detector to count the passing electrons. In both spectrometers the MAC-E filter principle is applied [KAT04], which is explained separately in the following.

**MAC-E Filter**<sup>5</sup> Two magnets create a inhomogeneous magnetic guiding field with an angular acceptance of  $2\pi$  for the electrons. The electrons are moving on cyclotron trajectories along the magnetic field lines. The magnetic field strength drops by several orders of magnitude from the entrance to the middle of the MAC-E-Filter (the analyzing plane). The magnetic gradient force transforms the cyclotron energy  $E_{\perp}$  of the electrons into longitudinal energy  $E_{\parallel}$ . In the analyzing plane the electrons are moving almost parallel to the field lines. This is illustrated in Figure 2.3 by the transformation of the momentum vector. The magnetic field changes slowly compared to one cyclotron cycle, therefore the transformation of the momentum is adiabatic. Hence, the magnetic dipole moment is preserved:

$$\mu = \frac{E_{\perp}}{B} = \text{const.} \quad (2.3)$$

This means, that the  $\beta$ -electrons are isotropically emitted in the source and transformed by the MAC-E filter into a beam of trajectories parallel to the magnetic field lines. The electrodes create a electrostatic retarding potential, that reflect all electrons with an energy below this potential. The electrons, that can pass this filter, are guided to the detector. This means, that the MAC-E-Filter works as an integrating high-energy pass filter. The relative sharpness of the filter is determined by the ratio of the maximum magnetic field strength  $B_{\text{max}}$  and the magnetic field strength  $B_A$  in the analyzing plane:

$$\frac{\Delta E}{E} = \frac{B_A}{B_{\text{max}}} \quad (2.4)$$

The integrated energy spectrum of the  $\beta$ -electrons can be measured by varying the retarding potential<sup>6</sup>. For more details of the MAC-E filter used in the KATRIN experiment see [KAT04].

---

<sup>4</sup>In order to achieve an improvement of one order of magnitude, the determination of  $m_{\nu}^2$  from Equation 2.2 must be improved by two orders of magnitude.

<sup>5</sup>Magnetic Adiabatic Collimation with an Electrostatic Filter

<sup>6</sup>or the source potential respectively

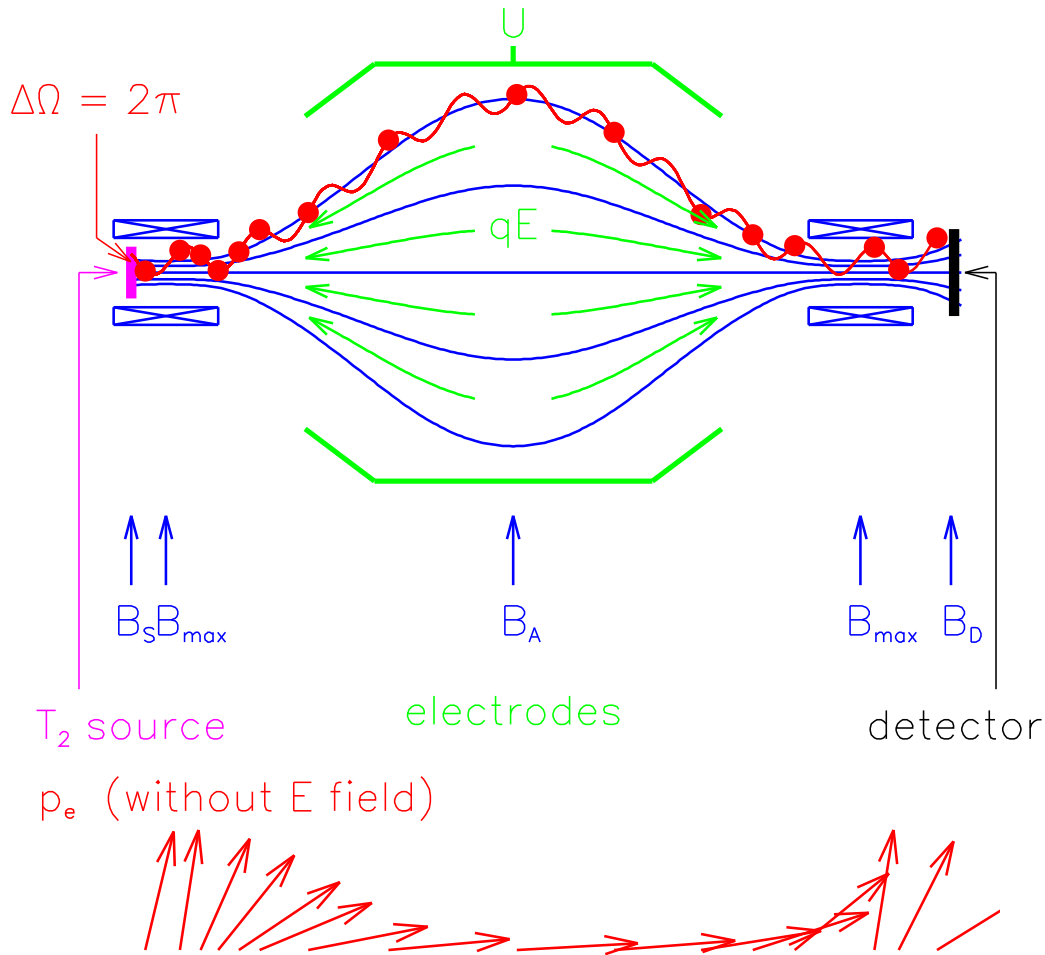


**Figure 2.3: Principle of the MAC-E-filter.** [KAT04] The electrons are emitted from the source in the left solenoid and guided along the magnetic field lines. In the middle between the superconducting magnets the field strength has dropped by several orders of magnitude and the momentum of the electrons has been transformed adiabatically into the longitudinal direction. Only electrons with sufficient energy  $E \geq |eU|$  can pass the potential barrier, that is created by the cylindrical electrode system, and will be guided to the detector. Thus a high pass filter is created.

**Pre-Spectrometer** The KATRIN pre-spectrometer is a MAC-E-Filter and does the first filtering of the  $\beta$ -electrons. It is a cylindrical vacuum chamber with a length of 3.38 m and a diameter of 1.7 m. The maximum energy of the electrons is 18.6 keV. The filter potential will be set to  $-18.3$  kV, which is 300 V below the  $T_2$  endpoint. Hence, only electrons above 18.3 keV can pass the pre-spectrometer to the main-spectrometer. The pre-spectrometer is being operated at a pressure of  $p < 10^{-11}$  mbar in order to reduce the background count rate from ionization processes inside. The electron flow rate into the main-spectrometer is reduced by a factor of  $10^6$ . This is necessary to suppress the background from residual gas ionization processes in the main-spectrometer. Currently the pre-spectrometer is being tested as a prototype of the main-spectrometer on-site of Forschungszentrum Karlsruhe.

**Main-Spectrometer** The task of the main-spectrometer is to analyze precisely the energy of the electrons in the endpoint region of the  $T_2 - \beta$ -spectrum. The principal setup is similar to the setup of the pre-spectrometer, but due to the high resolution, the conservation of magnetic flux and the adiabatic energy transformation the dimensions of the cylindrical vacuum chamber are larger. The main-spectrometer is 23.3 m long with a diameter of 10 m. It is also being operated at a pressure of  $p < 10^{-11}$  mbar. The inhomogeneous magnetic field, that is necessary for a MAC-E filter, is created by two superconducting magnets, each on one end of the spectrometer. Additional air coils will be installed for field shaping and the compensation of the earth magnetic field. The main-spectrometer has been delivered to Forschungszentrum Karlsruhe in December 2006.

The inner surface of the chamber will be laid out with a modular wire electrode system. The wire electrode consists of two layers. The inner layer of the wire electrode will be operated at the actual filter potential of  $\approx -18.6$  kV. Together with a decrease of the magnetic field strength by more than four orders of magnitude ( $B_A/B_{\max}$ ) an energy resolution of 0.93 eV can be achieved. The complex system of wire electrodes has been designed in Münster and is currently being manufactured there, too. It is planned to install them into the main-spectrometer in autumn 2008.

The background, that can possibly be created in the main-spectrometer, plays a significant role for the sensitivity, that can be reached. Only  $\approx 1$  mHz of background is allowed. In order to minimize the background the outer layer of the wire electrode will be operated at a potential of about +100 eV higher than the potential of the inner layer. This potential difference will reflect electrons coming from the spectrometer wall<sup>7</sup>. This means, that the wire electrode will reduce the background coming from the outside.

The second possible source of background is tritium, that would reach the spectrometer section. Tritium in the spectrometer can contribute to the background in two ways. It increases the probability for residual gas ionization processes and it can decay. The decay can lead to low energy secondary electrons, which can be accelerated and collimated towards the detector. There they would be counted with an energy close to the retarding energy  $|eU|$ . To prevent this the flow rate of tritium into the spectrometer has to be

---

<sup>7</sup>Possible sources of electrons are cosmic rays and environmental radioactivity.

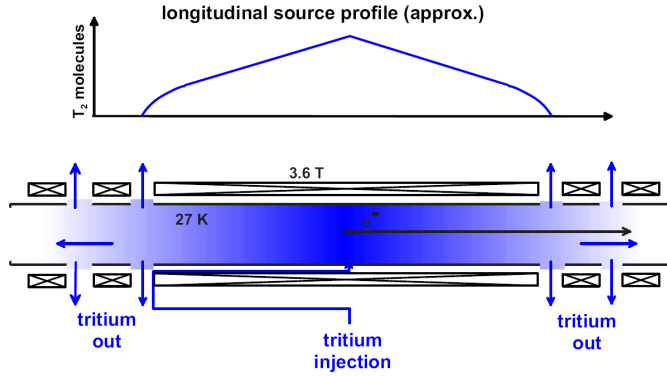


**Figure 2.4: Schematic overview of the windowless gaseous tritium source (WGTS).** [KAT04] The tritium is injected in middle of the WGTS and pumped out at both ends (bottom). A constant density profile is created (top).

minimized. This will be accomplished by the transport section, which will be explained in Section 2.5.

**Detector** The detector is the last part of the beamline and has to count all transmitted electrons. For this task it must have a high efficiency of  $\varepsilon > 0.9$  for electrons at 18.6 keV. Especially for the investigation of the transport properties and the homogeneity of the tritium source it is necessary to have a detector with a good spatial resolution. The background from the detector itself should not exceed 1 mHz, while being able to measure high count rates of  $\approx 1$  MHz for test measurements. These requirements are met by a segmented pin diode (SPD) with a radial and azimuthal segmentation of 148 pixels [Thü07]. Test measurements with an  $8 \times 8$  pin diode are conducted at the pre-spectrometer at the moment.

## 2.4 Tritium Source

The KATRIN experiment uses a windowless gaseous tritium source, named WGTS. The use of a gaseous tritium source has the advantage of high luminosity and small systematic uncertainties. It has to be windowless, so that the decay electrons can adiabatically leave the source. The WGTS of KATRIN is a 10 m long tube with a diameter of 90 mm. The tritium gas is injected continuously in the middle of the tube through capillaries. The tritium molecules move freely from the middle of the tube to both ends, where several turbomolecular pumps are installed. These two pumping systems, one at each end, are called DPS1-R and DPS1-F<sup>8</sup>. They remove most of the tritium ( $\approx 99\%$ ) from the beamline. This creates a constant density profile of tritium molecules along the source tube, see Figure 2.4.

<sup>8</sup>Differential Pumping Section One - R = Rear; F = Forward

The KATRIN tritium source must fulfill the following requirements:

- A constant column density of  $\varrho d = 5 \cdot 10^{17}$  molecules per  $\text{cm}^2$  must be established. This corresponds to  $9.5 \cdot 10^{10}$  decays per second. For this the tritium must be injected with a flow rate of  $1.853 \frac{\text{mbar l}}{\text{s}}$ . This equals 40 g of tritium per day.
- The column density  $\varrho d$  must be stable within 0.1 % to reduce systematic uncertainties. This requires the following parameters to be stable:
  - The purity of the injected tritium must be  $> 95$  %.
  - The injection rate as well as the collection rate at both ends of the source must be precise to 0.1 %.
  - The temperature of 27 K must be precise to 0.1 %.

The tritium source tube is installed inside of superconducting magnets. The latter create a magnetic guidance field for the electrons. The maximum field strength is  $B = 3.6$  T. The decay electrons are bound to the field lines, so that half of them are moving along the field lines towards the transport section; the other half will move to the other end of the source, where a rear wall will be installed, which absorbs those electrons.

The throughput of 40 g tritium per day can only be realized with a closed tritium loop. The test experiment TILO showed that this is possible [Kaz07]. An injection/collection system is currently being tested. The tritium, that can not be collected at the downstream end of the WGTS will flow into the transport section ( $\approx 10^{-2} \frac{\text{mbar l}}{\text{s}}$ ). At present the WGTS is under manufacture at the company ACCEL and the delivery is planned for 2010.

## 2.5 Transport Section

The task of the transport section is twofold:

- It has to guide the  $\beta$ -electrons from the tritium source adiabatically into the spectrometers. This is done with superconducting magnets and high magnetic fields. The electrons will be guided along the magnetic field lines and their energy will not be changed.
- It has to reduce the tritium flow rate from the source into the spectrometers. The background contribution of tritium in the spectrometer must not exceed  $\approx 1$  mHz. The maximum permitted tritium flow rate into the spectrometers is  $10^{-14} \frac{\text{mbar l}}{\text{s}}$ . Therefore the reduction factor must be  $\geq 10^{12}$ .

The transport section is divided into two parts: The differential pumping section DPS2-F and the cryogenic pumping section CPS. The maximum magnetic field inside of the transport section is 5.6 T. The magnetic field guides the electrons along the beamline, while the neutral part of the tritium gas is pumped. All tritium ions are also guided along the field lines and cannot be pumped. The behavior and handling of tritium ions is treated in Section 2.6.

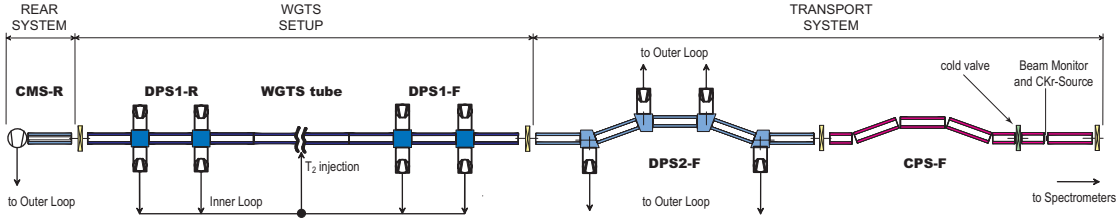


**Figure 2.5: The tritium related parts of the KATRIN experiment.** [Thü07] The figure shows the tritium source (WGTS) with the inner loop of the tritium cycle, the transport system consisting of the DPS2-F and the CPS, and the rear system for monitor and calibration purposes.

### 2.5.1 Differential Pumping Section

The differential pumping section DPS2-F uses turbomolecular pumps to reduce the tritium flow rate by a factor of  $10^5$ . This is called active pumping. At the end of the DPS2-F the tritium flow rate is reduced to  $\approx 10^{-7} \frac{\text{mbar l}}{\text{s}}$ . The tritium flow rate can not be reduced any more with active pumping, because the tritium gas diffuses back through the pumps. To prevent straight trajectories of the tritium molecules into the spectrometer, the DPS2-F consists of five tubes, that are tilted by an angle of  $20^\circ$  (cp. Figure 2.5). The DPS2-F is under construction and will be delivered at the end of 2008.

### 2.5.2 Cryogenic Pumping Section

Subsequently to the DPS2-F, the cryogenic pumping section CPS will be installed. It is operated at a temperature of 4.5 K and its inner walls are covered with argon snow. The argon snow adsorbs the tritium molecules and binds them, see Figure 2.6. The tritium flow rate is reduced in the CPS by a factor of  $> 10^7$ . This has been successfully shown in the TRAP experiment [Eic08]. Argon is the adsorbent of choice, because as an inert gas it does not form chemical bindings with tritium. Furthermore, it is possible to renew the argon frost layer before every measurement phase, so that no tritium inventory is accumulated. The manufacturing of the CPS has been contracted to Ansaldo Superconduttori in spring 2008.

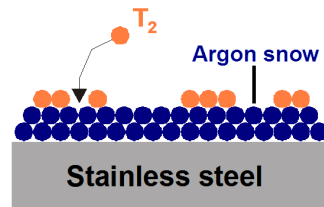
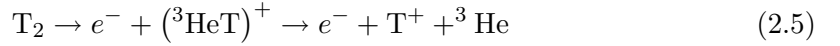


**Figure 2.6: Principle of the CPS.** [Bo07b] Tritium molecules are bound to the argon frost layer by the Van-der-Waals-force.

## 2.6 Tritium Ions in the KATRIN Source and Transport Section

Due to the high pressure in the WGTS of  $p_{max} = 3.35 \cdot 10^{-3}$  mbar, the possibility for the creation of ions is given. Several types of tritium ions are created in the WGTS from tritium  $\beta$ -decay itself and from  $\beta$ -electrons interacting with tritium molecules. The  $\beta$ -decay leads to the generation of  $T^+$ , which is shown in the following reaction<sup>9</sup>:



The  $({}^3\text{HeT})^+$  ions transform into  $T_3^+$  by the reaction:



Further scattering with  $\beta$ -electrons and tritium molecules leads to the creation of the following types of ions:

$$T^+, T_3^+, T_5^+, T^- \quad (2.7)$$

Even larger positive molecules are possible, e.g.  $T_7^+$ ,  $T_9^+$  et cetera. These types of ions are created within the WGTS and follow the magnetic field lines [KAT04]. The total ion flow rate is estimated to be between  $10^{11} - 10^{12}$  /s. The ions leave the WGTS either to the rear or the front side. At the rear side the ions hit the rear wall, where their electrical charge will be neutralized by charge exchange. The ions that leave the WGTS to the front side are bound to the field lines and move into the transport section. They cannot be removed from the beamline neither by the differential pumping section nor by the cryogenic pumping section.

Nevertheless, the tritium ions must be removed from the beamline for the following reasons:

- If the tritium ions ( $10^{11} - 10^{12}$  /s) would reach the spectrometers, they will contribute to the background in two ways:
  - They give rise to residual gas ionization inside of the main-spectrometer, and the secondary electrons can reach the detector.
  - When they decay inside of the spectrometer, the  $\beta$ -electrons can be trapped in the spectrometer and lead to residual gas ionization, which would cause secondary electrons other than from the tritium endpoint region to reach the detector.

If the tritium ions reach the spectrometers the background at the detector would increase by about  $\approx 200$  kHz, but only around  $\approx 1$  mHz are allowed [Glü06].

- Decay electrons from tritium ions have a different endpoint energy. This is, because the binding energy of the daughter molecule is changed by the presence or absence

---

<sup>9</sup>The neutrinos are not written down in the plasma calculations, but are still being emitted.

## 2.6 Tritium Ions in the KATRIN Source and Transport Section

of shell electrons. The endpoint energy of the electrons from any positive tritium ion  $T_i^+$  ( $i = 1, 3, 5, \dots$ ) is lower than from neutral  $T_2$ :

$$\Delta E_0 = E_0(T_i^+) - E_0(T_2) < -18 \text{ eV} \quad (2.8)$$

Therefore, the decay electrons from positive ions only have an impact for the KATRIN measurements farther below the endpoint region of the  $\beta$ -spectrum, i.e.  $\Delta E = E_0 - 50 \text{ eV}$ . Only the negative tritium ions have a  $\beta$ -spectrum with an endpoint energy above the endpoint energy of neutral  $T_2$ :

$$\Delta E_0 = E_0(T^-) - E_0(T_2) = +16 \text{ eV} \quad (2.9)$$

Therefore the presence of negative ions have more influence on the measured  $\beta$ -spectrum. The production rate of negative ions in the WGTS is estimated to be [KAT04]:

$$R(T^-) \approx 6 \cdot 10^5 \text{ cm}^{-3} \text{ s}^{-1} \quad (2.10)$$

Due to recombination processes with positive ions, their storage time is limited. Therefore, their final concentration relative to the neutral tritium density is estimated to be

$$n(T^-) / n(T_2) \leq 2 \cdot 10^{-8} \quad (2.11)$$

This is two orders of magnitude below the critical value, that would create an observable shift in the measurements of the neutrino mass [KAT04]. Therefore, the presence of the negative tritium ions is neglected in the following and only positive tritium ions are treated.

The removal of the positive tritium ions is accomplished in the transport section. The ion density and flow rate will be monitored, while they are removed. The monitoring will be done by an axial Penning trap called FT-ICR<sup>10</sup>. Inside of the FT-ICR the trapped ions are excited to cyclotron motion. The resonance frequency can be measured by mirror currents and from these the mass and charge of the ion can be determined [Ubi08].

To prevent the ions from reaching the spectrometer, it is planned to apply a positive potential of about 100 V at the downstream end of the differential pumping section. The positive ions will be reflected from the positive potential back into the direction of the WGTS. Since they move against a gas flow, they will be reflected again by collisions with other tritium molecules coming from the source. Thus the positive tritium ions are trapped in the front transport section between the gas flow from the WGTS and the positive potential at the DPS2-F [Glü07].

The ions accumulate in the transport section and lead to a high ion density of  $3 \cdot 10^5 / \text{cm}^3$  [KAT04]. This gives rise to plasma oscillations in the transport system. The time-dependent oscillations can change the energy of the  $\beta$ -electrons flying through this plasma. Especially the increase of their energy would falsify the KATRIN measurements.

In order to remove the positive ions from the transport section it is planned to install

<sup>10</sup>Fourier-Transform Ion-Cyclotron-Resonance

a dipole electrode in the DPS2-F. Then the ions can be removed from the beamline by the  $\vec{E} \times \vec{B}$  drift [KAT04]. Two penning traps of the FT-ICR type will be installed to monitor the tritium ions: One in front of the  $\vec{E} \times \vec{B}$  drift, and one behind to check the efficiency of the removal. The FT-ICR is currently under development at the University of Mainz.

These methods to monitor and remove the tritium ions have to be thoroughly tested before their application during the tritium operation. This means, that their functionality has to be investigated, after they have been installed to the DPS2-F. Therefore a test ion source is needed, which imitates the downstream output of the WGTS, i.e. its gas flow rate and ion density. The development of this test ion source is the topic of the present diploma thesis.

### 2.7 Requirements for the Test Ion Source

The test ion source will be installed directly to the upstream end of the DPS2-F. Thereby it has to supply the DPS2-F with an input similar to the output of the WGTS. Therefore, the reference values for the test ion source are deduced from the properties of the WGTS. The requirements for the test ion source are:

- Gas flow rate: The WGTS will emit a flow rate of neutral tritium of about  $\approx 10^{-2} \frac{\text{mbar}}{\text{s}}$ . In order to achieve likewise conditions during the test measurements the test ion source should produce a neutral gas flow of the same order of magnitude.
- Ion flow rate: The produced ion current from the WGTS is estimated to be between  $10^{11} - 10^{12}$  /s. The test ion source should achieve a comparable ion current.
- Ion types: Inside of the WGTS different types of ions are created:  $T^+$ ,  $T_3^+$ ,  $T_5^+$ ,  $T^-$ . Therefore, the test ion source should also produce ion clusters with different masses and charges.

For the design of the ion source the following working conditions have to be considered:

- Tritium: The purpose of the test ion source is to test the mechanisms that prevent a tritium contamination of the spectrometer. Therefore, the test ion source must not be operated with tritium, but with another comparable (and stable) gas.
- Magnetic field: The magnetic field from the superconducting magnets of the DPS2-F is also present at the entrance of the DPS2-F. The field strength is about  $\approx 3.8$  T. Therefore, the test ion source must be able to operate in such a magnetic field.
- Production area: Inside of the WGTS the ions are created continuously over the cross section area. Since the produced ions are bound to the field lines, they also reach the DPS2-F with a continuous spatial distribution. Therefore, the goal of the test ion source is to produce ions also on the whole cross section area, i.e. the ions cannot be fed in from the side.

## *2.7 Requirements for the Test Ion Source*

These are the experimental boundary conditions that have to be considered in the development of the test ion source. The next chapter treats the theory of different ionization processes and possible types of ion sources, which come into question for the realization.

## 2 *The KATRIN-Experiment*

## 3 Investigation of Possible Ion Sources

The previous chapter outlined the details of the KATRIN Experiment and its need for an ion source to test the transport section. The present one gives a survey of the theory of ion production with a special focus on hydrogen gases. This discussion is the basis for the next step, the evaluation of the optimum method for the test ion source.

As it is the purpose of the test ion source to imitate the downstream output of the tritium source without the use of tritium, a different kind of gas must be chosen. Deuterium is the one of choice for the following reasons:

- The chemical behavior is similar, as deuterium and tritium are both isotopes of hydrogen.
- Although they differ clearly in the rotational and vibrational states, the ionization properties of hydrogen, deuterium and tritium are similar, i.e. data can be cross-used if otherwise not available.
- All three isotopes form diatomic molecules ( $H_2/D_2/T_2$ ) in their pure and natural gaseous state.
- Also, deuterium has the closest mass to tritium of all hydrogen isotopes<sup>1</sup>.
- Deuterium is not radioactive, which makes experimental handling easy.

Therefore, the following discussion focuses on gaseous deuterium.

### 3.1 Ionization Process

The ionization of a particle means to remove one or more electrons from its atomic shell. In doing so the particle's charge is reduced and it becomes a positive ion. The addition of electrons is also possible and produces negative ions. Simulations of the plasma in the WGTS have shown that most of the upcoming ions are positive (cp. [Glü06] and Section 2.6). Thus the following explanations focus on the removal of electrons.

In any case the process of ionization needs energy, which can be transferred in various ways, e.g. thermal, optic, electric or kinetic. The amount of energy does not depend on the kind of energy supply. The electrons in the atomic shell have different binding

---

<sup>1</sup>The atomic mass of an ion gives an effect in several places, e.g. the detection in the FT-ICR and cyclotron motion in magnetic fields. Therefore, ions with a mass similar to Tritium are favored. As Tritium is the heaviest of the two hydrogen isotopes ( $m = 3$  u), the second heaviest (Deuterium with  $m = 2$  u) is more suitable for the experiment than the pure hydrogen ( $m = 1$  u). The difference in the charge-to-mass ratio can be bolstered by readjusting the magnetic field strength.

### 3 Investigation of Possible Ion Sources

energies, which are also called ionization energies. The amount of energy that is needed to remove the first (second,  $i$ th) electron from a particle, is called first ionization energy  $W_1$  ( $W_2$ ,  $W_i$ ).

Diatomic deuterium molecules are hold together by a covalent bond of two electrons. Like in the case of the molecular hydrogen this compound is strong; the first ionization energy of deuterium is [Liu04]:

$$W_1(D_2) = 15.4 \text{ eV.}$$

After the removal of one electron the two positive atomic nuclei are repelled from each other by their positive charge, but hold together by the remaining electron. The second ionization step would dissociate the molecule and demands less energy (4.5 eV).

In general the probability for an ionization process depends on three terms: The particle density  $n$ , the length  $l$  of the considered ionization path, and the cross section  $\sigma$ , which depends on the kind of participating particles and their energies. The product of these terms gives the ionization probability:

$$P = nl\sigma$$

The particle density  $n = N/V$  can be transformed with the ideal gas law into the more accessible parameters pressure  $p$  and temperature  $T$ :

$$pV = Nk_bT \Leftrightarrow n = \frac{p}{k_bT}$$

The particle density is determined by pressure and temperature. This changes the formula of the ionization probability to

$$P = nl\sigma \Leftrightarrow P = \frac{pl\sigma}{k_bT} \quad (3.1)$$

In general the product of ionization probability  $P$  and number of primary particles per second  $j_{\text{primary}}$  gives the number of ions  $j_{\text{ions}}$  per second:

$$j_{\text{ions}} = j_{\text{primary}} \cdot P$$

The first step in the consideration of a possible ionization partner is the calculation of the particle current needed to receive a certain ion current:

$$j_{\text{primary}} = \frac{j_{\text{ions}}}{P} = \frac{j_{\text{ions}}k_bT}{pl\sigma} \quad (3.2)$$

The variables of Equation 3.2 can be estimated:

- Ion current  $j_{\text{ions}}$ : The demand of ions per second is given by the estimation for the WGTS [Glü06]. It is between  $10^{11}/\text{s}$  and  $10^{12}/\text{s}$ . For the following calculations the maximum value is assumed ( $j_{\text{ions}} = 10^{12}/\text{s}$ ).

### 3.1 Ionization Process

- Pressure  $p$ : The maximum pressure in the WGTS is  $3.4 \cdot 10^{-3}$  mbar at a temperature of 27 K. This gives the order of magnitude for the calculation ( $p = 10^{-3}$  mbar).
- Temperature  $T$ : For practical reasons the test experiment will be conducted at standard room temperature ( $T = 293$  K).
- Length  $l$ : This is the path length of the primary particle and it is estimated with the typical dimension of an ion source vacuum chamber ( $l = 20$  cm).

With these estimations the ionization probability and the number of primary particles per time can be expressed as a function of the cross section  $\sigma$ :

$$\begin{aligned}
 P &= \frac{pl}{k_b T} \cdot \sigma \\
 &= \frac{10^{-3} \text{ mbar} \cdot 0.2 \text{ m}}{1.38 \cdot 10^{-23} \frac{\text{J}}{\text{K}} \cdot 293 \text{ K}} \cdot \sigma \\
 &= 4.95 \cdot 10^{14} \cdot \sigma \left[ \frac{1}{\text{cm}^2} \right]
 \end{aligned} \tag{3.3}$$

and therefore

$$\begin{aligned}
 j_{\text{primary}} &= \frac{j_i}{P} \\
 &= \frac{10^{12}/\text{s}}{4.95 \cdot 10^{14} \cdot \sigma} [\text{cm}^2] \\
 &= 2.02 \cdot 10^{-3} \cdot \frac{1}{\sigma} [\text{cm}^2]
 \end{aligned} \tag{3.4}$$

Hence,  $P$  (and  $j_{\text{primary}}$ ) can be estimated by a constant times the (inverted) cross section. Both equations, 3.3 and 3.4, are only valid, if the ionization probability  $P$  is smaller than one and the ions are not absorbed by other processes. Since different ionization methods have different cross sections, they will be assessed in the next section.

## 3.2 Different Methods of Ionization

The following ionization methods are well-established in physics and were considered for the development of the ion source [Wol95, Bro04]:

- a) Radio frequency, microwave and electron-cyclotron-resonance ionization
- b) Vacuum discharge ionization
- c) Electron impact ionization
- d) Photoionization
- e) Ion impact ionization

Some of these categories include further variations of the same principle, e.g. electron impact ionizations are realized in many different ways. The first consideration of the principles a) – e) is about their general ability to produce suitable ions for the DPS2-F test experiment:

- a) These types of ionization principles belong to the field of time-dependent ion sources. Energy is coupled into a plasma region to excite electrons, which then do the ionization. These types of ion source are widely available from the commercial sector. The use of time-dependent fields is against the concept of imitating the gas flow from the WGTS, where there are no such fields. The reason for this is, that the electromagnetic fields could influence the behavior of charged particles in the transport section, e.g. disturb the measurements with the FT-ICR. Therefore, this whole class of ion sources is out of question.
- b) Vacuum discharge ion sources can produce high currents of metallic ions. But the operation is usually pulsed, the electrons are not homogeneously distributed, and the production mechanism is not optimum for gaseous ions [Wol95]. Thus, this type of ion source is not considered.
- c)-e) These methods of ionization are not excluded from the beginning, because their principles get along with the boundary conditions of the test experiment. They are considered more detailed in the following.

Standard ion sources of these types are usually not designed to produce ions on a whole cross section area, but for sharp and intensive beams. Thus the following approaches, namely electron impact ionization, photoionization and ion impact ionization, start from scratch without taking examples in ready-made ion sources.

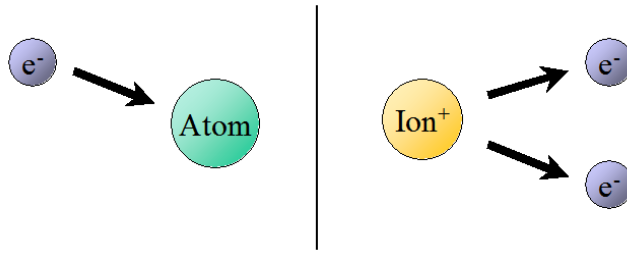


**Figure 3.1: Electron impact ionization.** The primary electron hits the neutral atom(left), and strips away the secondary electron (right).

### 3.2.1 Electron Impact Ionization

The bombardment of neutral atoms (or molecules respectively) with electrons can lead to the ionization of the neutral particle. The reaction is straight forward: The incoming (primary) electron, usually accelerated by an electric field, hits the atom. If the impact transfers enough energy to the atomic shell, a (secondary) electron will be ejected. The basic requirement is that the kinetic energy of the primary electron ( $W_{p.e.}$ ) must be larger or equal than the first ionization potential:

$$W_{p.e.} \geq W_1$$

or the accordant  $i$ th ionization potential  $W_i$  respectively. If enough energy is transferred to the electron, there will be three particles after the collision: The primary electron, the secondary electron and the positive ion. In order to maximize the primary electron's path length it is best to confine them in a potential well, optionally with an axial magnetic field. In that way their ionization path length is increased and therefore also the ionization probability. The electrons constantly loose energy not only by ionizations but also by excitations. When their energy falls below  $W_1$ , further ionization is impossible.

The first step in the consideration of electrons, as a possible ionization partner for deuterium, is the calculation of the number of electrons needed to receive a certain number of ions. The cross-section and therefore the ionization probability is dependent on the primary electron's energy. Figure 3.2 on page 40 shows the dependency of the cross-section from the electron's energy.

For the calculation it is supposed that the electrons have an energy of 50 – 100 eV, so that the cross section can be taken to be at its maximum of  $\sigma = 10^{-16} \text{ cm}^2$ . Then the ionization probability (after Eq. (3.3)) for electron impact on molecular deuterium is:

$$P = 4.95 \cdot 10^{14} \frac{1}{\text{cm}^2} \cdot 10^{-16} \text{ cm}^2 = 5 \cdot 10^{-2} = 5.0 \%$$

With the given probability  $P$  it is now possible to determine the demand of electrons

### 3 Investigation of Possible Ion Sources

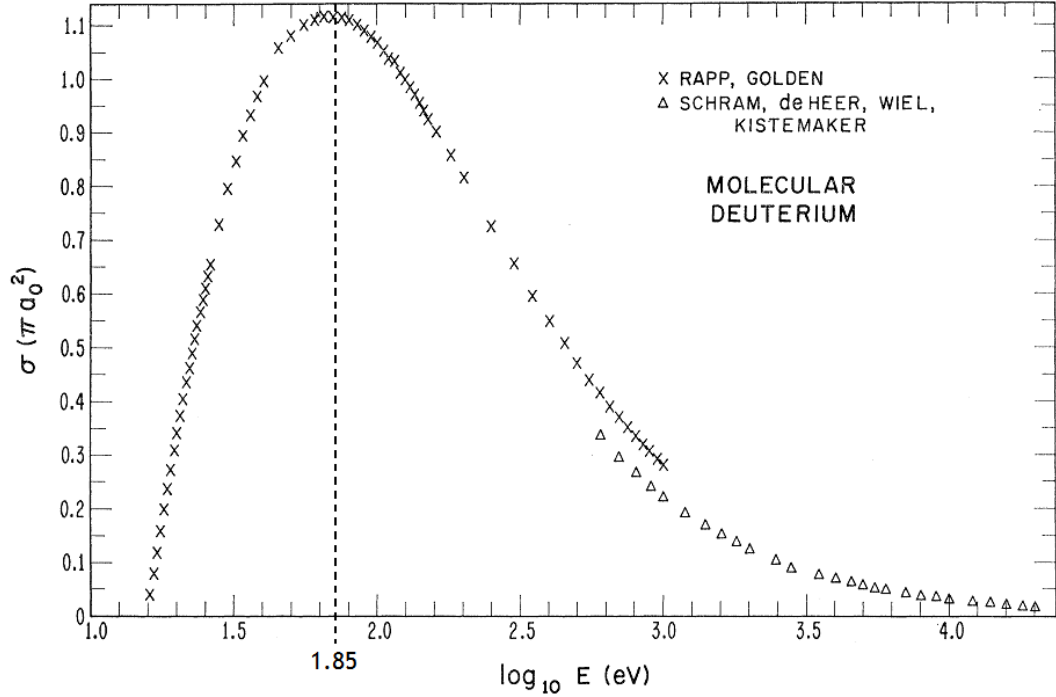


**Figure 3.2: Total cross section data for the electron impact ionization of molecular deuterium.** [Kie66] In general the ionization probability is zero for energies below  $W_1$ ; the maximum probability is usually between the three- and fivefold value of  $W_1$ ; then it decreases with rising energies. For molecular deuterium the most efficient region can be found between 50 – 100 eV. The maximum value of  $\approx 10^{-16} \text{ cm}^2$  is found at 70 eV.

(Conversions: y-axis  $1 \pi a_0^2 \approx 0.9 \cdot 10^{-16} \text{ cm}^2$ ; x-axis  $10^{1.85} \text{ eV} = 70.8 \text{ eV}$ )

for the desired ion current from Equation 3.4:

$$j_{e^-} = \frac{2.02 \cdot 10^{-3} \text{ cm}^2}{10^{-16} \text{ cm}^2} \frac{\text{cm}^2}{\text{s}} = 2 \cdot 10^{13} \frac{1}{\text{s}} \quad (3.5)$$

An electron impact ion source needs of course an internal electron source. The requirements for a hypothetical electron source were calculated above. It has to produce

- at least about  $2 \cdot 10^{13}$  electrons per second
- at an energy of about 50 – 100 eV.

Due to the numerous possibilities to produce electrons in large numbers, it is likely that the above requirements can be met. Electron sources in question will be discussed in Section 3.3.

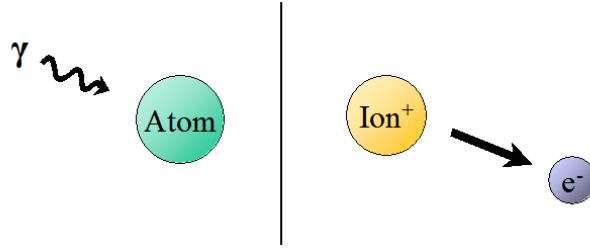


**Figure 3.3: Photoionization.** The energy transfer to the ion is negligible due to its higher mass. The excess energy is provided to the secondary electron; its energy distribution is sharp.

### 3.2.2 Photoionization

In the process of photoionization the ionization energy is provided by a photon. The energy of the photon is determined by the wavelength, thus

$$h\nu \geq W_1$$

Any exceed of the photons energy above the ionization potential will be transferred to the kinetic energy of the electron, see Figure 3.3.

The ionization potentials of the elements are usually in the range of 5 to 15 eV [Bro04]. Taking these for the photon's minimum energy, this results in a typical wavelength between 250 nm (for 5 eV) and 80 nm (for 15 eV). This corresponds to the near ultraviolet and the vacuum ultraviolet region. The total cross section for photoionization is also energy dependent, but different from the electron impact data (see Figure 3.4). The maximum cross section for molecular hydrogen is  $\sigma = 10^{-17} \text{ cm}^2$ . Now the ionization probability can be estimated with (3.3):

$$P = 4.95 \cdot 10^{14} \frac{1}{\text{cm}^2} \cdot 10^{-17} \text{ cm}^2 = 5 \cdot 10^{-3} = 0.5 \%$$

This leads to the needed number of photons per second ((3.4)):

$$j_\gamma = \frac{2.02 \cdot 10^{-3} \text{ cm}^2}{10^{-17} \text{ cm}^2} \frac{\text{cm}^2}{\text{s}} = 2 \cdot 10^{14} \frac{1}{\text{s}} \quad (3.6)$$

Hence, the requirements for a successful application of photoionization for the test ion source are photons

- from the vacuum ultraviolet ( $\lambda \leq 80 \text{ nm}$ )
- with a constant flow of  $j_\gamma \geq 2 \cdot 10^{14} \frac{1}{\text{s}}$ .

Each requirement itself is not difficult to fulfill. Photons of the desired wavelength are usually produced in synchrotrons or gas discharges. The latter can be done on a laboratory scale, usually with helium. Nevertheless, the possible intensities are at

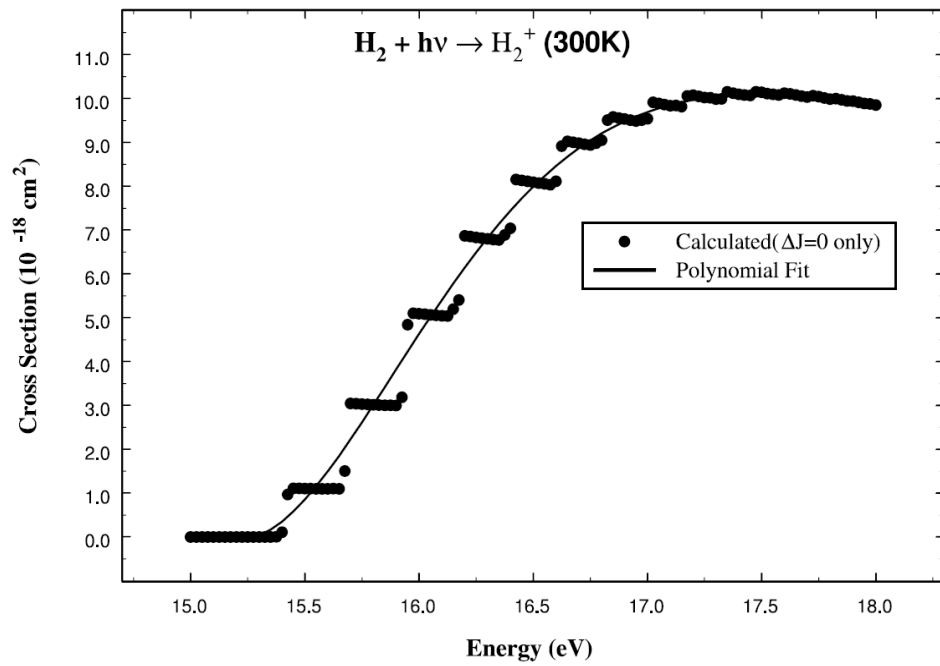


**Figure 3.4: Calculated cross sections for the photoionization of molecular hydrogen.**

[Liu04] After exceeding the minimum energy the cross section rises steeply from zero to the maximum value; not shown is the rather flat decrease with higher energies. For deuterium the minimum energy is 15.4 eV ( $\lambda \leq 80$  nm), the maximum cross section is  $10^{-17}$  cm<sup>2</sup> at 17.5 eV ( $\lambda = 70$  nm). Photons of higher energy have lower cross sections and are more difficult to produce and are therefore of no interest for photoionization. (The steps in the graph originate in the used computational method, cp. [Liu04].)

least two orders of magnitude below the goal [Sch83]. Another possibility would be a frequency multiplied laser, but this is hypothetical, because the needed multiplication is not feasible. This rules out the successful application of photoionization to produce the desired ion current for the test ion source.

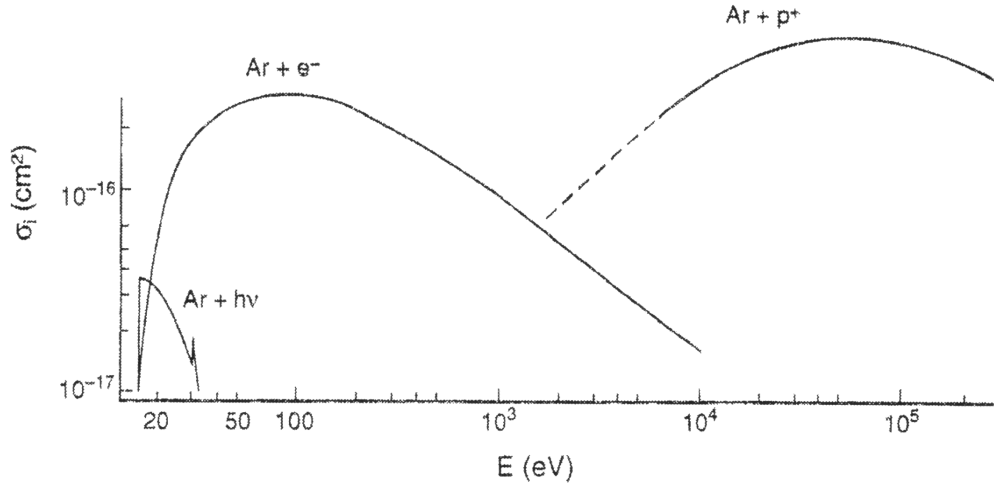


**Figure 3.5: Compared Cross Section Data for Argon.** [Bro04] The figure shows a comparison of cross section data for different ionization methods of argon. Ion impact can reach the highest cross section compared to electron impact ionization and photoionization, but requires more energy.

### 3.2.3 Ion Impact Ionization

To use one kind of ions to produce other ions is not widespread, but possible. The mechanism is based on charge exchange. Usually an energetic, incoming ion ( $10^4 - 10^6$  eV) collides with a low energy neutral atom and takes away an electron, and leaves a slow ion (the impulse transfer itself is small) [Bro04]. The cross section of ion impact ionization can reach decent values of about  $10^{-15}$  cm<sup>2</sup>; e.g. in Figure 3.5 it is shown for the proton impact ionization of argon. This is ten times higher than the maximum value of electron impact ionization and hundred times higher than photoionization. The ion impact ionization with protons is just an example, but it will be the reference value for the following estimations.

The major concern with an ion impact ionization source is the source of primary ions. In order to evaluate the primary ion source the number of needed ions has to be estimated. The estimation of needed particles begins with the ionization probability. With the same values for pressure, temperature and path length as it was mentioned on page 37 it calculates to (with Eq (3.3))

$$P = 4.95 \cdot 10^{14} \frac{1}{\text{cm}^2} \cdot 10^{-15} \text{ cm}^2 = 50 \%$$

Then Equation 3.4 gives the number of primary ions (*p.i.*):

$$j_{p.i.} = \frac{2.02 \cdot 10^{-3} \text{ cm}^2}{10^{-15} \text{ cm}^2} \frac{1}{\text{s}} = 2 \cdot 10^{12} \frac{1}{\text{s}} \quad (3.7)$$

Possible sources of such ion flow rates are now considered.

### 3 Investigation of Possible Ion Sources

- The regarded proton impact ionization for example would need an ion source itself for the supply of the test experiment. Protons again are produced in hydrogen ion sources, which has the same ionization boundary conditions as the deuterium ion source, that is to be build. Therefore the usage of protons for ionization does not solve the problem.
- Another possibility would be the gathering of ions from radioactive alpha decay, usually done with plutonium. The helium nuclei from the decay have an average energy of about 5 MeV and could ionize the deuterium gas. Regarding the needed number of primary ions  $j_{p,i}$ , a radioactive source with an activity of  $10^{12}$  Bq = 10 TBq would be required. This clearly exceeds the laboratory scale. Of course this is only valid, if every primary ion is accounted for only one ionization. A more reasonable source of  $10^6$  Bq = 1 MBq would still demand a  $10^6$ -fold multiple ionization per primary ion. Multiple ionizations in this order of magnitude are beyond the linearity requirements of Eq.(3.1) and physically unrealistic for this test experiment.

These arguments put an ion impact ionization source out of question. Nevertheless, the described charge exchange can be an important loss mechanism in the plasma region of ion sources. This is negligible for this test experiment, because there will be only a single type of isotope in the source and due to inelastic scattering they will only have low energies.

### 3.3 Determination of Optimum Ion Source

As seen in the previous section the primary ionization partner has to be chosen carefully. Both, the photoionization and the ion impact ionization, are unsuited to produce the necessary ion current. The first one, because photons of the necessary wavelength are difficult to be generated in that intensity; the latter, due to the absence of an high intensity ion source. On the contrary, electrons are widely available from matter and their energy is easy to manipulate. In the following the requirements of an electron impact ionization source for this experiment are summarized in order to evaluate the optimum electron source.

- Intensity: The calculations in Section 3.2.1 showed, that a continuous stream of about  $2 \cdot 10^{13}$  electrons per second at low energies of about 100 eV is necessary.
- Production Area: The ions have to be distributed uniformly on the cross section area of the DPS2-F. Because they are strictly bound to the magnetic field lines of the beamline, they have to be generated on the accordant field lines. Hence, the electrons must also be produced on the accordant field lines (see Figure 3.6 on page 45). Calculations showed, that in a distance of 15 cm to the first magnet in DPS2-F the flux tube has increased to an area of about  $300 \text{ cm}^2$  [Glü08]. The electron source in question must be able to produce electrons on an area of about this size.

These are the reference values for the following considerations of possible electron sources.

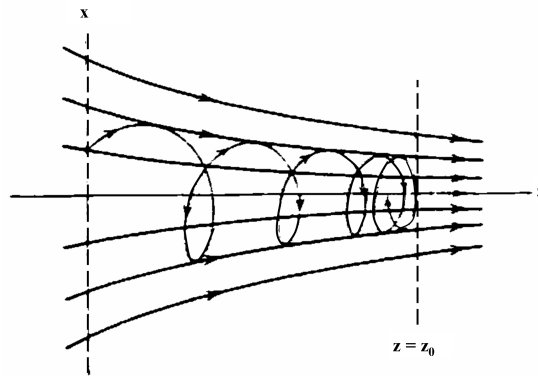


**Figure 3.6: Electron production area in a magnetic field.** [Jac02] Without the magnets of the tritium source the magnetic field in the entrance region of the DPS2-F has a strong gradient. A principle sketch is shown in the figure above, where the DPS2-F is supposed to be on the right side. The production area of the electrons must be in front of the DPS2-F, i.e. to the left side, where the flux tube is increased. As the electrons are bound to the field lines, they must be generated on an area, that is larger than the cross section of the DPS2-F.

### 3.3.1 Electrons from Field and Thermionic Emission

The most used electron emitting process is the field emission, that is also used in many ion sources. Established variants, the hot and the cold cathode, are working either with thermal heating or high electrical fields to extract the electrons from the solid state. Both kinds of cathodes are usually realized as a metal tip. These single tips only emit electrons on an area equal to the size of the tip itself. To reach a larger effective area the only possibility is to use an array of tips, e.g. like in tungsten brushes. This could be used as hot or cold cathode. For a hot cathode a temperature of  $\approx 1000$  K is needed. This would heat up the surrounding gas and is unlike the conditions in the WGTS and DPS2-F (30 K / 80 K). Therefore, the hot cathode is not considered to be a possible choice for the electron source. On the other hand, cold cathodes need high electrical fields of  $10^7$  V/cm to induce electrons to tunnel out of the solid state [Bro04]. The needed number of electrons can be easily reached with this method, but the electrons would have to be de-accelerated to have a more efficient cross section. Otherwise the ions would have to be kept away from the strong potential gradient of  $10^7$  V/cm. The needed potential gradient can be reduced by field emission points of the nano scale. The so-called Field-Emission-Point-Arrays (FEPA) contain large numbers of nano-sized tips on a macroscopic area, e.g.  $1 \text{ cm}^2$  [Bla07]. FEPAs can create electron currents that are appropriate for this experiment with an applied voltage of about 2 kV. The high voltage that is needed makes the electric field emission a possible, but not optimum electron source.

### 3.3.2 Electrons from Photoelectrical Effect

Electrons are held in the solid state body by a certain potential and have to gain an accordant energy to cross it. This threshold is called the work function  $W_0$  and for standard metals it is in the region of 5 eV. But there exist also other metals, e.g. the alkali metals, with low work functions of about 2 eV. Light of a low enough wavelength (high energy per photon) can transmit this energy and unhinge electrons from a metallic surface. This means that the light source must have a spectrum in the near ultraviolet. The excess energy is transferred into the kinetic energy:

$$W = h\nu - W_0 \quad (3.8)$$

The light's frequency determines the energy of the electron. The light's intensity determines the number of electrons per area and time. The depth of which electrons can still be emitted is usually in the order of magnitude as the wavelength of the incident light. The ratio of emitted electrons per incoming photon is called quantum efficiency (QE). It can reach values of up to 20% for multi-alkali compounds (mainly used for photomultipliers). For standard metals it is usually in the broad range of  $10^{-6} - 10^{-2}$ . Furthermore the quantum efficiency is wavelength dependent. If the wavelength is shorter, the photon energy is higher and it is more likely that the photon transfers enough energy to an electron to eject it from the metal. This means, that the quantum efficiency generally rises with higher photon energy.

To receive electrons of low energy it is possible to extract them from a metal surface via the photoelectric effect. The basic requirement for this is a light source with photons, which energies must exceed the work function of the photocathode. Then the photocathode emits electrons continuously distributed and proportional to the incoming light intensity. This is a possible electron source, if enough electrons can be extracted.

The following estimation shows that enough ions for the test ion source can be produced with this principle. Standard ultraviolet lamps (Mercury-Xenon or Deuterium lamps) can irradiate about  $10^{17}$  ultraviolet photons per second on an area of  $300 \text{ cm}^2$  in a distance of 15 cm (calculation based on [Lot04]). With an assumed quantum efficiency of  $10^{-4}$ , this causes about  $10^{13} \frac{e^-}{s}$  to leave the photocathode. This matches the original requirement from Section 3.2.1 and shows that this principle is theoretically feasible. A detailed calculation for the effective number of ions will be found in Section 4.2. It follows a description of the fundamental features of such an ion source, based on the photoelectron impact ionization principle.

### 3.3.3 Basic Concept of a Photoelectron Impact Ion Source

First a gas flow rate has to be created in a vacuum chamber. Therefore, it is necessary to inject the deuterium gas, e.g. through a needle valve, into the vacuum chamber and pump it out at the other end at the same time. In that way a gas flow along the beamline can be created. The pressure can be controlled by the injection rate of the deuterium gas.

An ultraviolet lamp shines through a window into the vacuum chamber and illuminates a metal photocathode, which has a low work function if possible. The emitted electrons are accelerated by an electric potential, which can be applied either to the photocathode itself or to another acceleration electrode. With rising energy they can ionize the surrounding deuterium molecules (see Figure 3.7). The ions are bound to the magnetic field lines and are transported downstream by the gas flow, if the pressure is high enough. The downstream end of the test ion source will be connected to the DPS2-F, so that a neutral gas flow with a fraction of ions is injected into the DPS2-F.

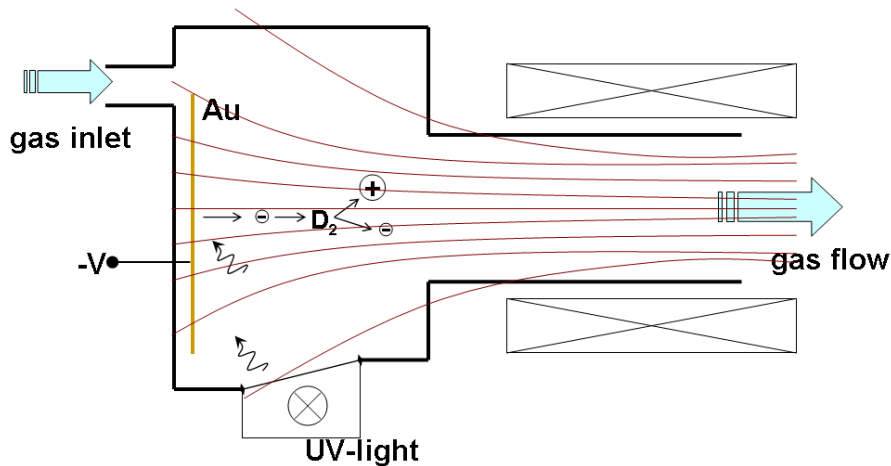


**Figure 3.7: Principle of electron impact ion source with a photocathode.** The photoelectrons are accelerated by a negative potential and ionize the Deuterium molecules. In this example the photocathode is made out of gold. Although the positive deuterium ions are attracted to the negative cathode, they are transported by the gas flow, if the pressure is high enough. All charged particles can only move along the magnetic field lines.

As no ion source of this principle was found in the physics literature<sup>2</sup>, the first experimental setup will be a prototype. It is meant to work as a proof of principle and to get experimental experience. The detailed structure of the prototype ion source, including the actual electron source, the confinement system, and the detector will be outlined in the following Chapter 4.

<sup>2</sup>An intensive search has been done regarding literature back to the 1970's.

### *3 Investigation of Possible Ion Sources*

## 4 Development, Design and Setup of the Prototype Ion Source

The actual chapter starts with a conceptual overview of the prototype ion source test experiment. The development and design of the prototype follows. Finally, the commissioning of the components is described. The proposals and recommendations for the test ion source for the transport section can be found in Chapter 6.

### 4.1 Experimental Overview

Based on the elementary photoelectron impact ion source, which has been introduced on page 47, a prototype ion source is discussed in the following sections. The prototype works after the principle of the elementary ion source, but also needs certain extensions. The basic components are:

- UV-Lamp, Window and Photocathode: As evaluated, an intense ultraviolet lamp shines through a window into the vacuum chamber onto the photocathode. The important properties of these components are the spectrum and intensity of the lamp, the transmission spectrum of the window, and the work function and quantum efficiency of the photocathode.
- Electrode system: The emitted photoelectrons are accelerated and are confined in a system of electrodes. There they ionize the deuterium gas and the deuterium ions are going along the beamline. The purpose of the electrode system is on one hand to confine the electrons, and on the other hand to stop the ions from reaching the cathode, where they would be neutralized.
- Ion Detection: Downstream they will be detected by a charge counter. This makes it possible to distinguish between ions and electrons, but also makes it necessary to separate them in the electrode system.
- Vacuum Setup and Gas Injection: A permanent gas flow has to be initiated; therefore a constant gas inlet as well as a permanent pumping of the vacuum chamber is necessary. The gas is injected through a needle valve and pumped out by a turbomolecular pump. The pressure is measured by a Baratron pressure gauge.
- Magnet: A magnetic field along the beamline is vital to guide the charged particles. Lacking an available magnet, a coil has been designed and built.

The individual components are shown schematically on the following page.

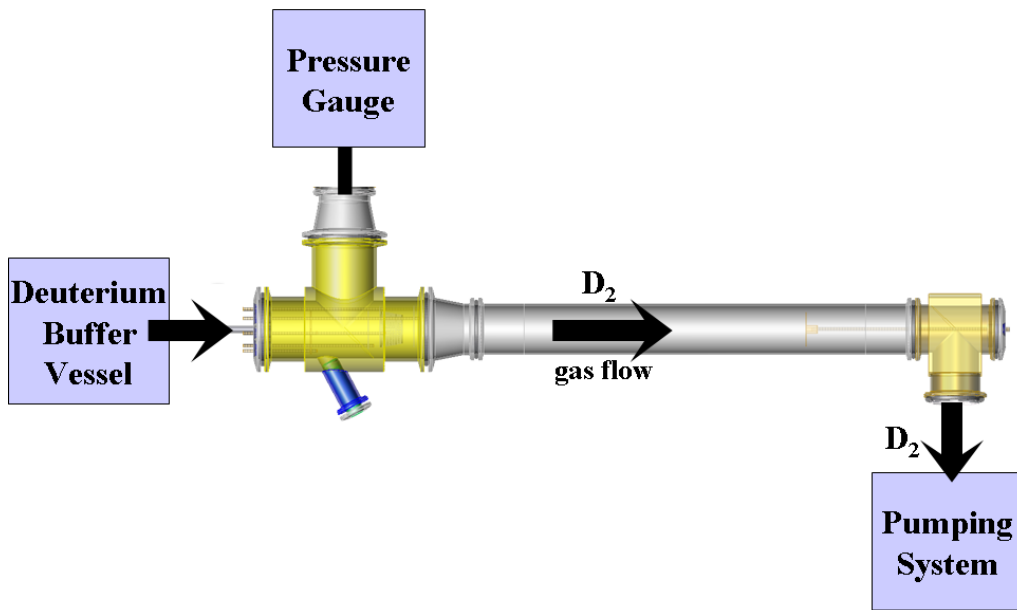


**Figure 4.1: Gas and vacuum setup of the prototype ion source.** The deuterium is stored in a buffer vessel and from there injected into the vacuum chamber. Together with the pumping system a permanent gas flow is created. The pressure is measured by an adjacent pressure gauge.

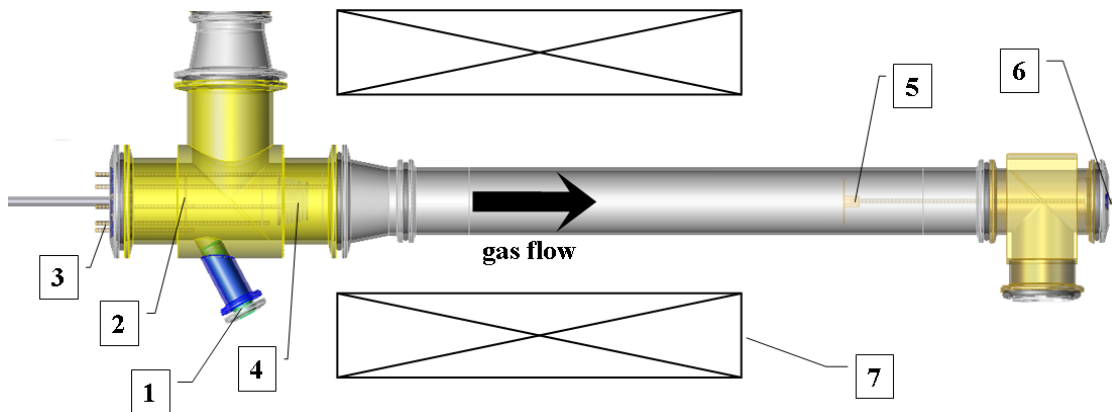


**Figure 4.2: Main components of the prototype ion source.** (1) Lamp holding and window (2) Photocathode (3) Electrical feed-throughs for electrode potentials (4) Electrode system and ionization region (5) Faraday cup (6) Electrical feed-through for current measurement (7) Magnet coil

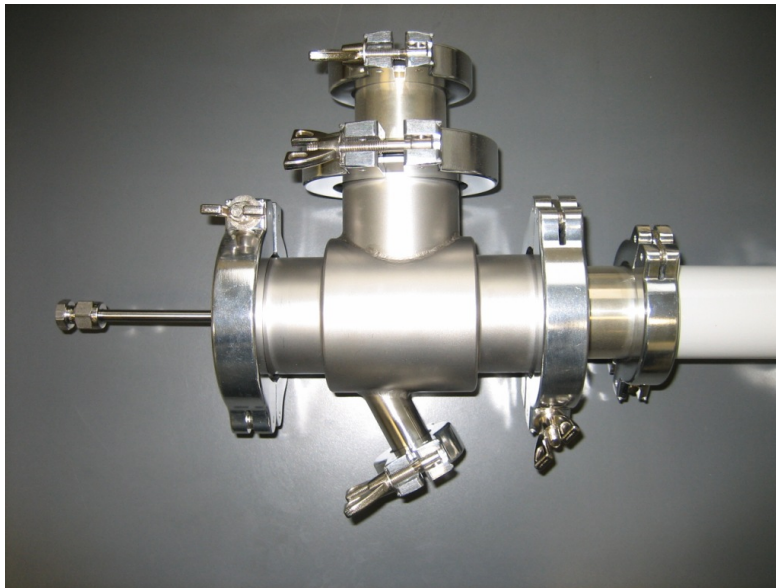


Figure 4.3: Picture of the main vacuum chamber of the prototype ion source. Compare with Fig. 4.2.

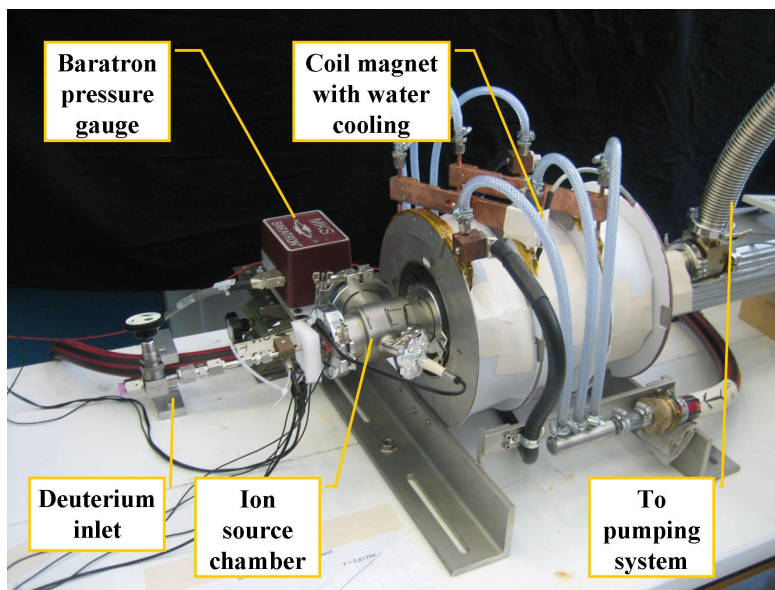


Figure 4.4: Picture of the prototype ion source setup. The ion source is placed in the central axis of the coil magnet. The figure also shows the deuterium inlet (buffer vessel not connected), the pressure gauge and the connection to the pumping system.

## 4.2 Design Parameters of the Prototype Ion Source

The ion source's principle has been theoretically verified. Now the design parameters are determined by a number of boundary conditions. First there are the physical requirements to be recalled.

- A neutral deuterium flow rate of  $\approx 10^{-2}$  mbar · l/s has to be established. The pressure has to be in the region of  $10^{-3}$  mbar.
- An ion flow rate of  $10^{11} - 10^{12}$  /s has to be created.
- A magnetic field is needed to to guide the charged particles along the beamline.

According to the project plan, the idea of the prototype is to achieve a proof of principle if possible - if it is not possible, then to outline why not. Since the prototype ion source should be examined within the scope of this diploma thesis, the setup has to be completed within a time limit. Therefore, the prototype ion source may have certain restrictions compared to the test ion source for the DPS2-F. This means, that for example the physical size of the ion source or the lamp intensity may be below the requirements for the test ion source for the DPS-2F, if it is cheaper and/or faster. The setup consists mainly of parts that were chosen due to their availability. This means, the original requirements have not necessarily to be met by the prototype, as long as the principle is not different and the effects from changes can be estimated.

For this estimation the final current of ions can be calculated by the contemplation of several variables:

- Lamp Intensity (I): The number of emitted photons per second, that are directed towards the photocathode and have enough energy to produce a photoelectron.
- Transmission Function (T): The percentage of photons passing the window without getting absorbed or reflected.
- Quantum Efficiency (QE): The number of ejected electrons per incoming photon.
- Ionization Probability (P): The calculated probability for an electron to ionize a deuterium molecule.

The product of these terms give the total number of produced ions per second:

$$j_{ions} = I \cdot T \cdot QE \cdot P \quad (4.1)$$

Ionized deuterium molecules always have a single positive charge, so that the actual ion flow can be transferred into electrical current by adding the factor of the elemental charge. The detector (Faraday Cup = FC) measures:

$$I_{FC} = e \cdot j_{ions} \quad (4.2)$$

This means, that the original requirements of  $j_{ions} = 10^{12} \frac{\text{ions}}{\text{s}}$  equals to  $I_{FC} = 160$  nA.

## 4.3 Components of the Prototype Ion Source

The total ion current of the prototype ion source can now be estimated.

- Lamp Intensity (I): The lamp intensity is estimated to  $I \approx 10^{16} \frac{\gamma}{\text{s}}$ , cp. calculations in Section 4.3.1.
- Transmission Function (T): For this estimation the transmission function is assumed to be 100 %.
- Quantum Efficiency (QE): The quantum efficiency is taken to be  $QE \approx 10^{-4} \frac{e}{\gamma}$ , cp. Section 4.3.1.
- Ionization Probability (P): From the calculations in Section 3.2.1 the ionization probability is assumed to be  $P \approx 5 \cdot 10^{-2} \frac{\text{ions}}{e}$ .

The total number of produced ions can then be estimated to:

$$\begin{aligned} j_{ions} &= I \cdot T \cdot QE \cdot P \\ &= 5 \cdot 10^{10} \frac{1}{\text{s}} \end{aligned} \quad (4.3)$$

Therefore, the measured electrical current is expected to be about

$$\begin{aligned} I_{FC} &= e \cdot j_{ions} \\ &= 8 \text{ nA.} \end{aligned} \quad (4.4)$$

According to these estimations, the test ion source for the DPS-2F must be upscaled by a factor of  $10-10^2$  compared to the prototype ion source. Each term of Equation 5.1 can be rescaled for single upgrades. E.g., when the photocathode is replaced with a different metal, the effect of changing quantum efficiencies can be easily taken into account.

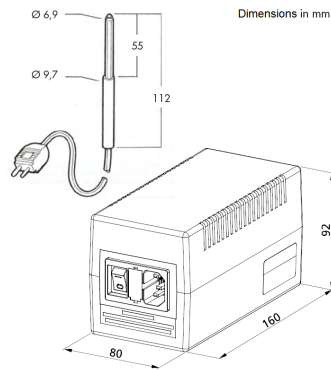
### 4.3 Components of the Prototype Ion Source

The following subsections focus on the development of the single components of the prototype ion source. The chosen design is outlined, while the technical drawings are in the appendix.

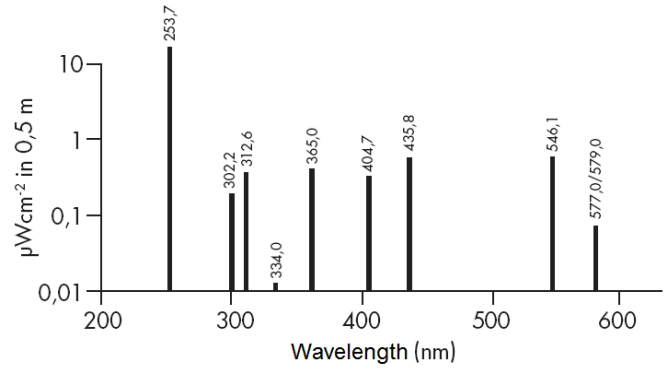
#### 4.3.1 UV-Lamp, Window and Photocathode

The elementary electron source consists of a lamp with a spectrum in the ultraviolet and a photocathode, from which the electrons can be emitted. Since a common UV-lamp is not vacuum compatible and the photocathode has to be inside the vacuum, an additional window is needed. The development and design of these three components are treated together, due to their strong relationship. The lamp has a specific spectrum with varying intensity at different wavelengths. The window has a special transmission function, allowing different wavelengths to pass with different losses. In the end, enough photons with an energy above the accordant work function must reach the photocathode.

## 4 Development, Design and Setup of the Prototype Ion Source



(a) The dimensions of the lamp are comparable to a pen.



(b) The spectrum of the UV-lamp has an intensive peak line at 253.7nm, which equals 4.9eV.

**Figure 4.5: The Pen-Ray Lamp, used in the experiment. [Lot07]** Both figures were taken from the original data sheet from Lot-Oriel.

Therefore, a choice for one of the three components has an impact on the choice of the other two.

### 4.3.1.1 Ultraviolet Lamp

The main property of a light source is the emitted spectrum, i.e. the intensity distribution over the wavelength. The integrated intensity below a certain wavelength (determined by the photocathode's work function) must be high enough to produce enough electrons for the ionization process. For an estimated work function of 5 eV the wavelength of the electrons must be  $< 260$  nm. Possible choices are common mercury, xenon or deuterium lamps. They are commercially available and can supply high intensities in the ultraviolet. Mercury lamps usually emit discrete spectral lines and often have an additional illuminant, e.g. argon or neon, to increase the number of spectral lines. Still the main supply in the region of interest ( $< 260$  nm) comes from the mercury lines. Deuterium lamps in general have lower intensities in the visible spectrum, but a continuous, intensive spectrum in the ultraviolet [Lot04].

For the prototype setup a mercury lamp, that was originally used for calibration purposes, was available. It is labeled Pen-Ray Line-Emitter and is supplied from Lot-Oriel ([www.lot-oriel.com](http://www.lot-oriel.com)). Its lowest wavelength line corresponds to 4.9 eV and is also the most intensive one (see Figure 4.5b). This means that the energy of the photons is higher than the work function of most standard metals,  $\approx 4 - 5$  eV.

The lamp's absolute intensity can be taken from the data sheet. For the only line in the region of interest the absolute intensity  $I$  is [Lot07]:

$$253.7 \text{ nm} \mapsto I = (74.0 \pm 6.1) \cdot 10^{-6} \frac{\text{W}}{\text{cm}^2} \text{ at a distance of 25 cm}$$

### 4.3 Components of the Prototype Ion Source

Assuming a smaller distance of 5 cm for the prototype setup, the intensity increases to:

$$253.7 \text{ nm} \mapsto I = (1.9 \pm 0.2) \cdot 10^{-3} \frac{\text{W}}{\text{cm}^2} \text{ at a distance of 5 cm}$$

The transition from wavelength to the photon's energy is done with:

$$\begin{aligned} c &= \lambda\nu \Leftrightarrow \nu = \frac{c}{\lambda} \\ \Rightarrow E_\gamma &= h\nu = \frac{hc}{\lambda} \end{aligned} \quad (4.5)$$

The number of photons per area and time can be calculated from the above given intensity:

$$i_\gamma = \frac{I}{E_\gamma} = \frac{I\lambda}{hc} \quad (4.6)$$

$$4.9 \text{ eV} \mapsto i_\gamma = (2.36 \pm 0.2) \cdot 10^{15} \frac{\gamma}{\text{cm}^2\text{s}} \text{ at a distance of 5 cm}$$

This value is important for the estimation of the number of photoelectrons, that can be produced.

#### 4.3.1.2 Window

There are many window materials available. Besides their vacuum sealing ability, the most interesting property is the transmission at different wavelengths. In any case the window material should be easy to handle and stable against common mechanical stress. For the prototype test setup standard quartz glass was chosen, due to its availability, good handling and transmission properties (see Figure 4.6). At the wavelength of interest the transmission is  $T > 90 \%$ .

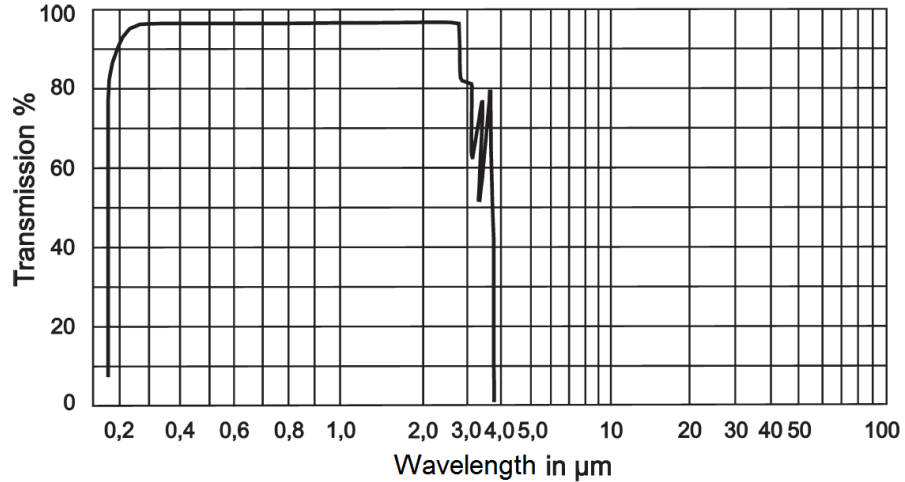


**Figure 4.6: Transmission Function of a Quartz Window.** [Vac07] The transmission in the region of interest around 250 nm is clearly above 90%; concerning Equation 5.1 these losses have only a small influence.

#### 4.3.1.3 Photocathode

The properties of the photocathode have to meet the following requirements:

- The most fundamental one is, that the work function has to be smaller than the energy of the peak line of the light source. That is, as the lamp is already chosen,  $W_0 \leq 4.9 \text{ eV}$ .
- To achieve high currents of electrons, the quantum efficiency should be as high as possible. In general the Q.E. is higher with lower work function.
- The material should be easy to handle and resistant against gas and air exposure. Especially in the test phase the exposure to different atmospheres will occur.

The latter rules out the use of any alkali metals and some compounds. Especially resistant in this sense are gold, nickel and stainless steel; where gold and nickel have higher work functions than the chosen ultraviolet lamp can handle:  $W_{\text{Au}} = 5.1 \text{ eV}$ ,  $W_{\text{Ni}} = 5.0 \text{ eV}$ . But both are interesting options for the upscaled test ion source. The work function of stainless steel is not clearly defined, due the wide range of different kinds. Experiences from the University of Münster have shown that a 265 nm light source is enough to produce electrons [Val08]. Therefore, also the 253.7 nm-line of the Pen-Ray lamp is sufficient. But for reasons of comparability three photocathodes have been built: Stainless steel, copper and aluminum. The latter two tend to get easily oxidized under the exposure of air, but have low work functions.

**Table 4.1: Different Materials for the Photocathode.** Three different metals have been chosen to evaluate them experimentally in terms of electrons, that can be produced. The table shows their properties taken from the literature.

Material	Work Function (eV)	Quantum Efficiency <sup>a</sup>
Stainless Steel <sup>b</sup>	$\leq 4.7$	$\approx 10^{-3}$
Copper <sup>c</sup>	4.7	$10^{-4}$
Aluminum <sup>d</sup>	4.1	$10^{-4}$

<sup>a</sup>at a wavelength of  $\lambda \approx (250 \pm 15) \text{ nm}$

<sup>b</sup>Source: [Val08]

<sup>c</sup>Source: [Dav93]

<sup>d</sup>Source: [Kaw84]

Each of them is built after the same design and has a surface area of  $A_{\text{phc}} = 9.6 \text{ cm}^2$  exposed to the light source. The angle of incidence of about  $30^\circ$  reduces the effective area to  $A_{\text{eff}} = 4.8 \text{ cm}^2$ . With a given surface area the total number of incident photons per time can be estimated with Equation 4.6:

$$\begin{aligned}
 j_\gamma &= A_{\text{eff}} \cdot i_\gamma \\
 &= 4.8 \text{ cm}^2 \cdot (2.36 \pm 0.19) \cdot 10^{15} \frac{\gamma}{\text{cm}^2\text{s}} \\
 &= (1.13 \pm 0.09) \cdot 10^{16} \frac{\gamma}{\text{s}}
 \end{aligned} \tag{4.7}$$

The way how the photocathode is treated after its manufacturing is vital for its efficiency. Each photocathode has been thoroughly polished, cleaned and vacuum-outbaked. The polishing has been done with different strengths of sandpaper in successive steps, beginning with the roughest, then with increasing smoothness of the sandpaper (800, 1000, 1200, 2000, 2400, 3000, 4000) and the additional usage of water. The visible effect of this is clearly shown in Figure 4.7. Afterwards they have been cleaned with acetone and subsequently outbaked at  $200^\circ\text{C}$ . Without these preparations the efficiency of the photoelectrical effect can be about two orders of magnitude smaller. Each photocathode will be tested in Section 5.1.2, regarding their ability to emit electrons from the photoelectrical effect.

### 4.3.2 Electrode System

The design of the electrode system has a high influence on the ionization process. Standard setups foresee a cathode and three further electrodes:

- One electrode in short distance to the photocathode to accelerate the electrons to the desired velocity.
- One in a larger distance on the same potential to have a narrow energy distribution on their ionization path.

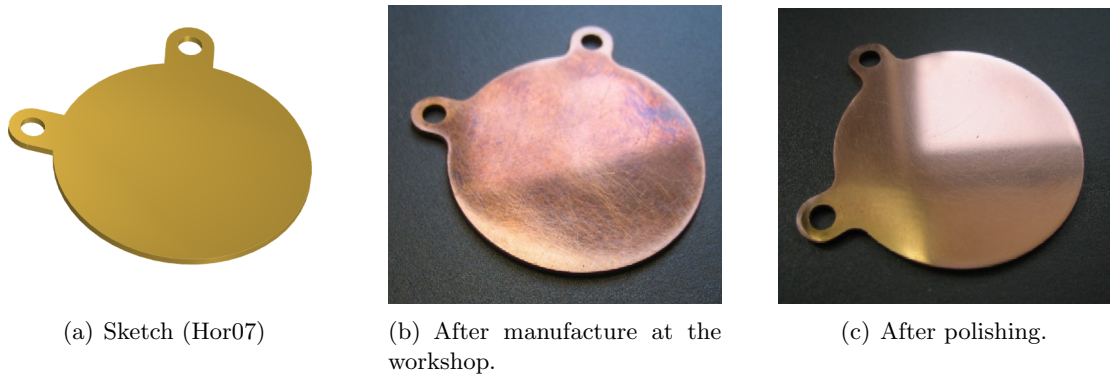


**Figure 4.7: Photocathode made of Copper.** As shown in the pictures, the polishing increases the smoothness and purity of the metal's surface, and therefore the quantum efficiency.

- And a last one after a short distance to de-accelerate or confine them.

In this experiment the electrons are confined for two reasons: They must not reach the Faraday Cup, as their electrical charge would cancel out or even exceed the positive ion current. Second, if they are confined, they will be periodically reflected and their ionization path length increases and therefore also the ionization probability. Furthermore, they could do multiple ionizations, if their energy is high enough.

Taking this standard setup of one cathode and three electrodes as a model and apply it to the present case, gives different roles to the electrodes.

- The first electrode has to extract the electrons from the photocathode. Its potential has to be more positive than the cathode potential, so that the photoelectrons, having only small starting kinetic energy ( $\approx 0.5 - 1$  eV), should be able to fly through it.
- The second electrode has to put the electrons on the ionization potential and also shield the ionization region from the inner walls of the vacuum chamber, which are on ground potential. Therefore, a cylinder geometry has been chosen, see Figure 4.8.
- The third and last electrode has to reflect the electrons back to the ionization region and, if possible, support the extraction of the ions from it.

The optimum potential distribution, in terms of maximizing the ion current, is difficult to predict and has to be determined experimentally.

### 4.3 Components of the Prototype Ion Source

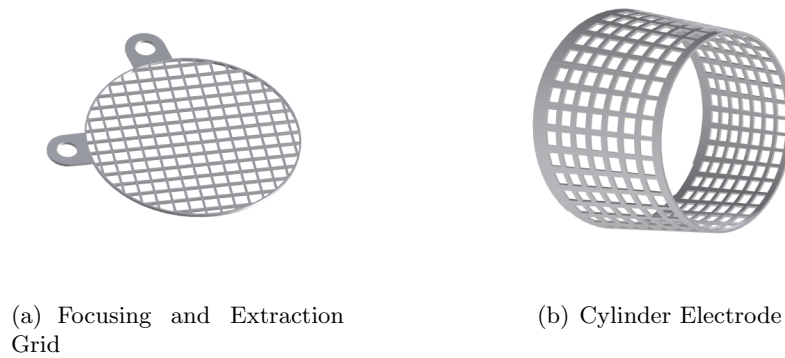


**Figure 4.8: Drawings of the Electrodes.** [Hor07] First and last electrode are constructed as a plain mesh and have a transparency of about 90% (left), the middle electrode is a cylinder with a 100% transparency in the direction of the beamline (right).

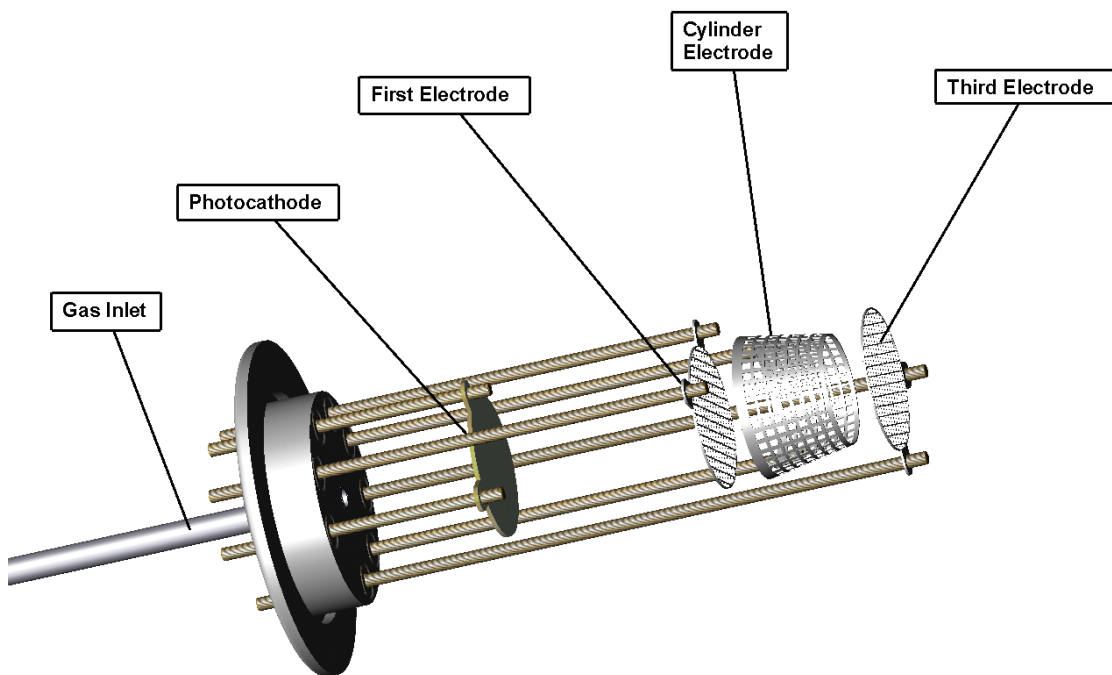
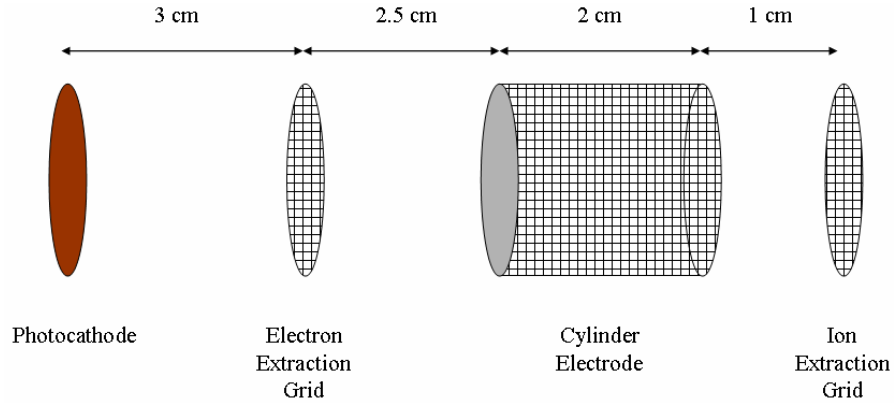


**Figure 4.9: Mounted Photocathode and Electrode System.** [Hor07] The photocathode and the electrodes are mounted on the inside of a flange. The electrical feed-throughs are accessible from the outside.

## 4 Development, Design and Setup of the Prototype Ion Source

The distances between the electrodes are adjustable and the configuration for the test measurements are shown here:



The distance between photocathode and electron extraction electrode is comparatively high to the other distances, to prevent shadows from the first mesh on the surface of the photocathode.

### 4.3.3 Ion Detection

Because the prototype setup has to work as a proof of principle, a simple but reliable detection system was preferred. For this purpose a Faraday Cup, the easiest way for an electrical charge detection, is sufficient. A Faraday Cup is a metal plate, which has its name from the classical cup-form. When charged particles hit the metallic surface, the charged particle either loses its charge due to charge exchange (for the case of ions) or it is absorbed (electrons). The amount and direction of the current can be measured, if a high sensitivity ampere-meter is linked between the Faraday cup and ground potential.

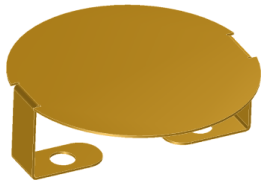


**Figure 4.10: Sketch of the Faraday Cup.** [Hor07] It has the same size as the photocathode.

The direction of the current is determined by the kind of charge (positive or negative), so ions and electrons can be distinguished. However, both currents can also cancel out each other, if arriving at the same time, which is a disadvantage and one of the reasons why ions and electrons must be separated. The advantages of a Faraday Cup are its reliability and robustness. It can measure the absolute ion (or electron) current while being mass independent<sup>1</sup>, and the sensitivity is constant over time. The small sensitivity ( $> 10^{-16}$  A or  $> 10^3 \frac{\text{ions}}{\text{s}}$ ) is a disadvantage. Optionally a suppressor electrode in front of the Faraday cup can be added to force any secondary electrons (from ion impact on the surface) back to the detector. This is not necessary in the present setup, because the ions will only have thermal energy, once they reach the detector.

<sup>1</sup>The mass of the incoming charged particle.

The features that determine the properties of a Faraday cup are its form and material. For this experiment a plain metal plate of the size of the photocathode is sufficient. The choice of the material is important regarding the vacuum compatibility and especially the efficiency. Therefore, it is made out of nickel, which is also resistant against oxidation. To increase the efficiency the Faraday cup was thoroughly polished, analogue to the photocathodes in successive steps with increasing surface smoothness of the sandpaper. Then the absolute efficiency can be taken as  $\approx 100\%$  for low energy particles, as used in this experiment [God67].

#### 4.3.4 Vacuum Setup and Gas Injection

The intended pressure region is  $10^{-3}$  mbar, but for the test experiments a wider range is useful to understand the system's pressure dependencies. Therefore, measurements will be taken in the range of about  $10^{-5} - 10^{-2}$  mbar. The main task of the vacuum setup is to create a constant gas flow. Therefore, a buffer vessel is needed to supply the ion source with deuterium. From this vessel the gas is streaming through a control valve into the vacuum chamber. The gas inlet is behind the photocathode, so that the gas flows around it, cp. Figure 4.9. Adjacent to the ionization region the pressure is measured by a Baratron, which is a high sensitive, capacitive pressure gauge. Further downstream, directly behind the Faraday cup, the connection to the pumping system is made to create a pressure gradient. The pumping system was available from a recently finished experiment and carries a diaphragm pump as well as a turbo-molecular pump, along with two pressure gauges (hot and cold cathode).

**Table 4.2: Pressure gauges in the prototype ion source setup.**

Name	Maximum Range	Minimum Range	Application
Pirani	$10^3$ mbar	$10^{-2}$ mbar	Pump port
Penning	$10^{-2}$ mbar	$10^{-9}$ mbar	Pump port
Baratron	$10^{-1}$ mbar	$10^{-6}$ mbar	Ionization chamber

The electrical feed-throughs for the electrodes are integrated into the flanges and self-made by the on-site workshop. The connections to the electrodes are realized by thin metallic poles out of nickel, that also hold the electrodes in place, see Figure 4.12 on page 62.

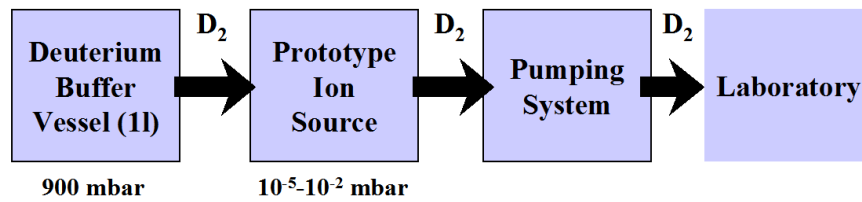
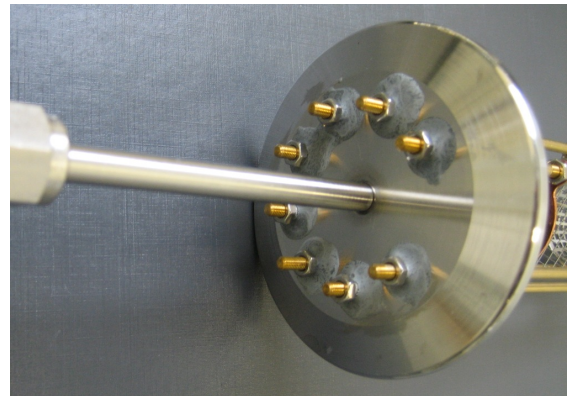


**Figure 4.11: Vacuum diagram of the prototype setup.** The deuterium is stored in a buffer vessel and pumped through the ion source to create a gas flow. The pumping system ejects the gas into the laboratory. Even if the complete stock of deuterium would escape at once into the laboratory system, the critical concentration of hydrogen/deuterium (4.5 vol.-%) in the experimental hall would not be exceeded.



(a) Drawing of Ion Source Flange



(b) Picture of Ion Source Flange

**Figure 4.12: Flanges with Electrical Feed-Throughs.** [Hor07] An electrical potential can be applied from the outside, while each electrode is hold by two poles. Two holding poles per electrode instead of only one have the advantage, that they prevent a rotational shifting of the electrodes.

### 4.3.5 Design of the Magnet

As the prototype setup is supposed to be tested completely without the DPS2-F, it is still necessary to simulate likewise conditions during the test experiment. As mentioned before, this also includes the presence of an axial magnetic field along the beamline. Therefore, a coil magnet is needed to contain the beamline of the prototype ion source. It is appropriate to operate the prototype with a smaller field strength than the original inside of the DPS2-F. Lacking available alternatives the construction of a new magnet was necessary. In order to estimate a smaller, but still satisfying magnetic field strength, the following boundary conditions have been considered:

- The cyclotron radius of all charged particles must not exceed the dimensions inside the vacuum chamber, i.e. the mesh aperture of the grids. In fact, it should be much smaller, in the sub-millimeter region. Because of their higher mass, the deuterium ions have in any case a larger radius, compared to the agile electrons. To guarantee a cyclotron radius for the ions in the range of about  $10^{-6}$  m, and therefore a low loss from cyclotron motion, the magnetic field should exceed 50 mT . This is feasible with a non-superconducting magnet. For comparison, the maximum magnetic field inside of the DPS2-F is 5.6 T resulting in a cyclotron radius in the order of magnitude of  $10^{-8}$  m.
- Due to the magnetic mirror effect a charged particle can be reflected while moving into a region with increasing field strength. The shape of the magnetic field with regard to the ion source is determined by the magnet's geometry and the placement of the ion source. The photocathode and the Faraday cup should be placed as near as possible to the homogeneous region. Furthermore their positions should be symmetrically to the magnet's center, so that they cover the same flux tube. This determines the inner radius of the magnet coil, which must be large enough to contain certain flanges.

These are the basic conditions that have to be fulfilled. On the one hand, the desire for a small cyclotron-radius dictates the strength of the magnet. On the other hand, the magnetic mirror effect has to be reduced, which influences the geometrical design of the magnet.

A magnet coil from the University of Münster [Bau07] was taken as a model and modified to meet the present requirements. The idea was that the windings are not done by a wire, but by a tube. In that way the cooling water can be pumped through the tube, while the electrical current flows through the tube's hull.

The dimensioning of the magnet coil is explained in the following:

1. The inner diameter of the coil was chosen to be 16 cm, so that a 100CF-flange with an outer diameter of 15.9 cm fit inside. This is more than enough for the prototype test setup and it is also the current estimation for the setup of the upscaled test ion source.

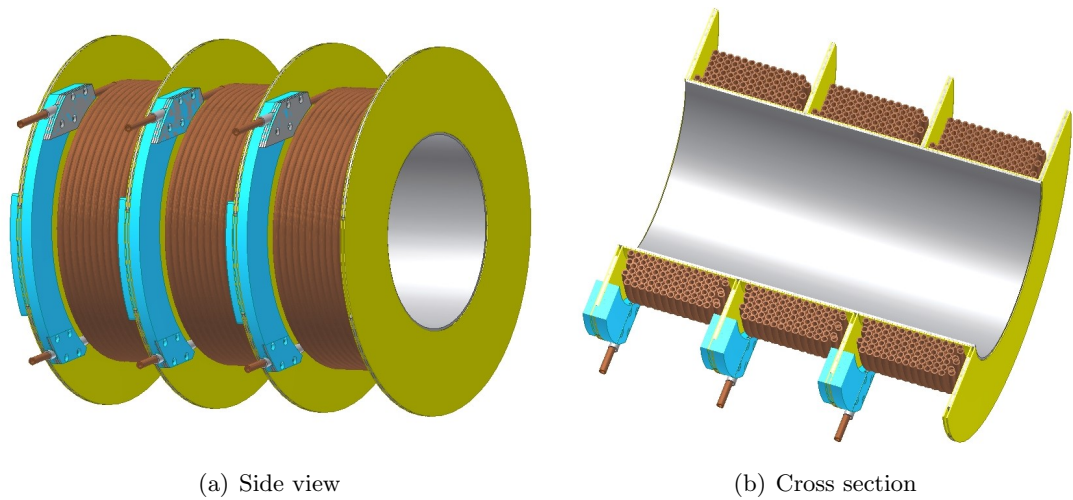


**Figure 4.13: Drawings of the Magnet Coil.** [Hor07] To decrease the needed pressure of cooling water, the magnet is divided into three independent coils. Then the coils can be cooled parallel, while the electrical current flows in series. The side view (a) shows the combined connections for water and electrical current. The cross section (b) shows the layers of the copper tube.

2. The chosen diameter increases the necessary length of the coil, so that the requirements of a typical *long magnet coil* can be met (length  $\gtrsim$  inner diameter). Therefore, the length was chosen to be 30 cm.
3. The windings are copper tubes with an outer diameter of 6 mm and a wall thickness of 1 mm, leaving an inner diameter of 4 mm.
4. From 1.-3. follows, that the coil needs a total tube length of about 150 m to reach approx. 210 windings.
5. The pumping of an appropriate amount of cooling water through a 150 m long and 4 mm thin tube would require a pressure of  $> 10$  bar. To reduce the requirements for the water cooling, the magnet consists of three separated coils. Each coil consists of  $3 \cdot 50$  m pieces, see Figure 4.13 on page 64. Hence, the cooling water can be pumped parallel through the three coils, while the electrical current flows in series through the three coils.

With this setup a working point of 100 mT can be reached at 120 A. An electrical current of 120 A results in a thermal rating of about  $P \approx 3$  kW. This is the minimum cooling power, that is needed for a stable operation of the magnet. Higher currents are possible, dependent on the cooling system. The maximum current, that can be supplied, is 175 A. This corresponds to 145 mT and results in a thermal rating of about  $P \approx 6$  kW.

The challenge in building this magnet was the proper insulation of each winding against its neighbors and against the coil body. Beside the electricity the insulation needs to

resist varying temperatures and water from condensation. The copper tube is double-shielded with Kapton tape, which insulates and also resists long-term temperatures up to 180°C, on short-terms up to 350°C. Due to the double-shielding, there are at least four layers of Kapton between two conductors. This safety measurement is necessary, because the tape is only 0.06 mm thick and easily receives scratches during the winding process. The insulation between of the coil body itself against the windings is done by a 2 mm layer of Teflon.

#### 4.3.6 Data Acquisition and Slow Control

The prototype ion source test experiment has several in- and outputs.

The inputs are:

- Lamp current → light intensity
- Coil current → magnetic field strength
- Electronic needle valve → pressure
- Voltage supplies → potentials on photocathode, electrodes

All inputs are manually controlled over power supplies. The readout of all values is also done manually and directly from the power supply.

The outputs are:

- Pressure → pressure gauge
- Current through Faraday cup → (pico)amperemeter
- Temperature of magnet coil → slow control

The values from the pressure gauge and the amperemeter will be read out manually. The temperature is under constant surveillance by a PT100 thermometer<sup>2</sup>, which has been inserted in the middle coil of the magnet. The thermometer is connected to a computer, that reads the temperature every second and can react to it. If the temperature exceeds a certain value (e.g. 50°C), a warning is showed on the screen. If another, more critical value (e.g. 70°C) is reached, the slow control turns off the magnet's power supplies in successive steps within of ten seconds.

---

<sup>2</sup>A temperature-dependent platinum resistor with 100 Ω at room temperature.

## 4.4 Commissioning

Before assembling the experimental setup, the necessary infrastructure has to be considered. The magnet needs intensive cooling to lead off up to 6 kW of thermal rating as well as a three-phase current supply. The storage of deuterium must follow certain safety regulations. All requirements with regard to safety and auxiliary systems are fulfilled by the Hall 245 on-site of Forschungszentrum Karlsruhe (FZK).

### 4.4.1 Vacuum System and Gas Injection

All vacuum parts were ultrasonically cleaned and baked-out before commissioning. Once mounted, the complete system was also vacuum baked-out. A leak test has had to be exercised to ensure a proper sealing of each valve and flange. Single leaks have been found at the self-made feed-throughs, but could be sealed with an epoxy-resin glue (Bondmaster E3520). Afterwards, an integral leak rate of  $5 \cdot 10^{-10} \frac{\text{mbar}\cdot\text{l}}{\text{s}}$  was measured, which is clearly enough to conduct experiments at  $10^{-5}$  mbar. According to the Penning pressure gauge, the lowest achievable pressure is around  $5 \cdot 10^{-7}$  mbar.

In order to induce a gas flow, the buffer vessel was filled with deuterium at a pressure of 900 mbar and connected through an electronic-controlled valve to the vacuum system. With a special voltage control, the pressure of the gas flow can be controlled, and measured with the Baratron. The Baratron's read-out is precise to 1%, but during a typical measurement the pressure itself can float with  $\pm 10\%$ .

The pressure cannot be readjusted or readout during a measurement, because the magnetic field disturbs the Baratron's functionality. Magnet and Baratron are placed adjacent, because the Baratron has to measure the pressure as close to the ionization region as possible, which itself has to be as close to the magnet as possible. When increasing the magnetic field and crossing a certain threshold, the Baratron's output jumps to a high and arbitrary pressure. When the field is decreased below this threshold again, the malfunction stops and the correct pressure is shown again. The threshold has been estimated, with a field map calculation [Glü08] to  $B_{\text{crit}} \approx 1.5 - 2.0$  mT. Further effects to the KATRIN-experiment are discussed in Chapter 6.

The ion source was inserted into the magnet (Figure 4.14). The placement in the magnetic field is crucial for efficiency. The beamline of the ion source has to be identical with the central axis of the magnet, so that charged particles can travel down along the field lines without hitting the walls. Furthermore, both photocathode and Faraday cup should be as close as possible to the homogeneous region of the magnetic field to minimize the magnetic mirror effect. Due to the flanges of the Baratron pressure gauge the photocathode can not be placed at the entrance of the coil, but ca. 6 cm away. Therefore the distance between the photocathode and the Faraday cup was chosen to be 46 cm, while the length of the magnet is 30 cm. In that way the system can be installed symmetrically with photocathode and Faraday cup each 8 cm away from the entrance region of the coil.

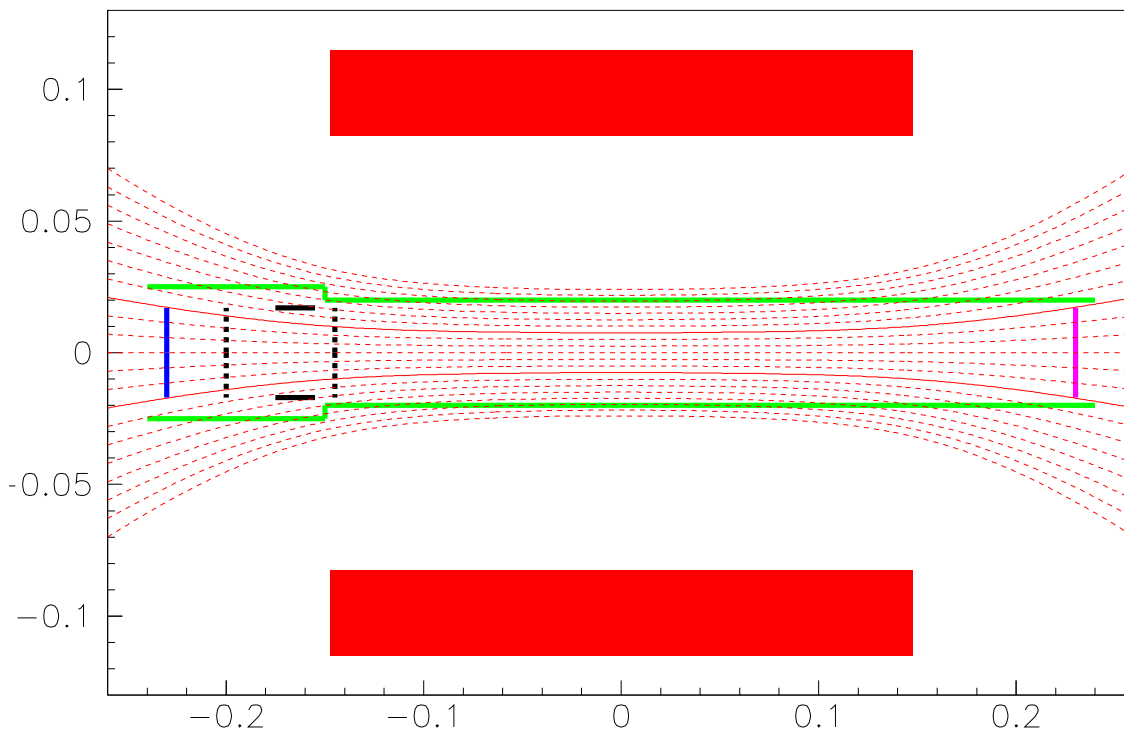


**Figure 4.14: Map of selected magnetic field lines.** [Glü08] The calculation of the field map is based on the dimensions of the magnet. The map shows the ion source vacuum chamber (green) placed inside of the magnet coil (red). On the left hand side the photocathode (blue) and electrodes (black) are shown. The Faraday cup (purple) is symmetrically to the photocathode on the right hand side. The two solid field lines represents the flux tube, that covers the photocathode as well as the Faraday cup. The axis are scaled in [m].

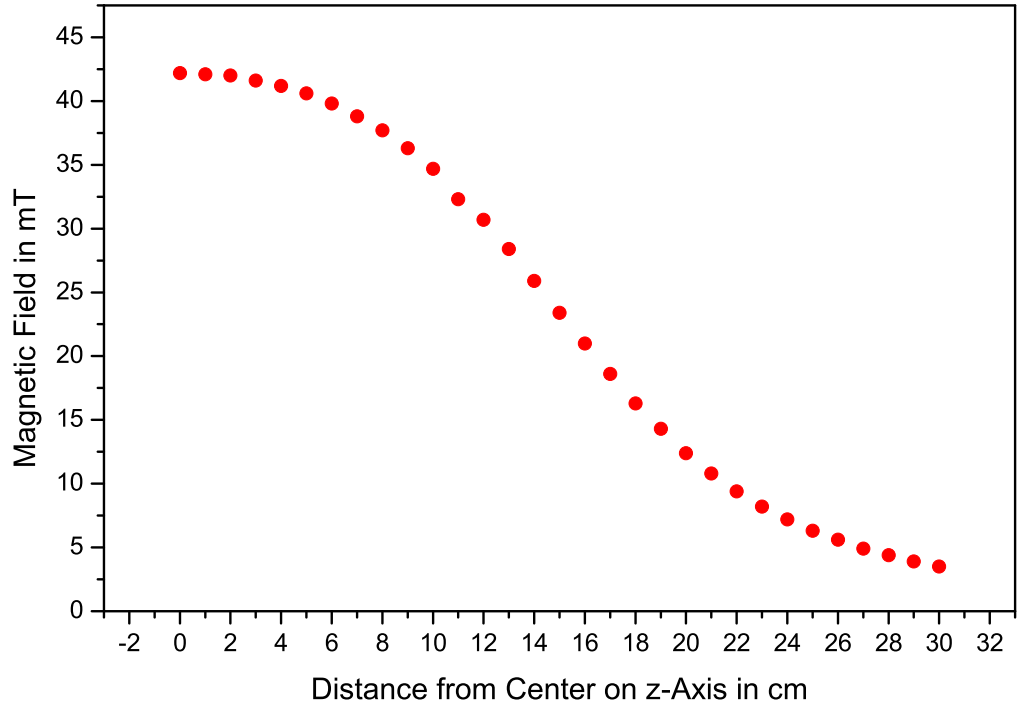


**Figure 4.15: Calculated magnetic field strength along the axis of the coil.** Together with Eq.(4.8) it is possible to determine the magnetic field strength along the axis for a given current from the figure.

#### 4.4.2 Magnet Calibration

The magnet was calibrated with a hall probe in the center of the coil and varying coil current. The calibration measurement itself can be found in the appendix on page 100. The proportional factor was determined from the calibration to

$$a_{\text{center}} = 0.82 \frac{\text{mT}}{\text{A}} \quad (4.8)$$

at the center of the coil. The field strength at the center of the photocathode is smaller by a factor of 19.4 %, cp. Fig.4.15. Therefore, the proportional factor for the magnetic field at the photocathode is:

$$a_{\text{ph.c.}} = 0.16 \frac{\text{mT}}{\text{A}} \quad (4.9)$$

Analogue, the magnetic field strength at any coordinate along the z-axis of the coil can be calculated in relation to the center of the coil.

## 5 Measurements and Results

The measurements are divided into two parts. To understand the generation process of ions it is necessary to examine the production and behavior of electrons preliminarily. The optimum photocathode for the following measurements is determined first. Then the electron production is examined for different pressures, magnetic field strengths, acceleration potentials and light intensities in Section 5.1. When familiar with this principle, the next step is the generation of ions. Here, the influences of pressure, magnetic field and especially the potential distribution on the ion production are studied, see Section 5.2. Conclusions are given after every measurement, while the summary discussion of all results is in the final part of this chapter, Section 5.3.

### 5.1 Photoelectron Production

The first goal of the prototype experiment is to understand the system without the use of deuterium. That means to gain control over the electron production, which is important for the final understanding and control of the ion production.

#### 5.1.1 Experimental Procedure

The absolute amount of the electron current that reaches the Faraday cup and therefore can be measured is dependent on several variables. Hence, a standard configuration is now introduced, that determines all values, except the one that is measured. In this way the different measurements become more comparable. These standard values come from the experience of several test runs.

The standard configuration for electron production is:

- The standard photocathode is made out of copper, as it produces the most electrons (see below).
- The light intensity is maximum, i.e. 20 mA on the power supply scale. A preheating of 3 – 5 min is necessary.
- The magnetic field is set to its maximum, i.e. 145 mT in the center, to decrease the cyclotron-radius of the electrons. This corresponds to 28 mT at the photocathode.
- The potential of the photocathode is put on  $-10$  V, so that the electrons can gain enough longitudinal energy in order to overcome the magnetic mirror effect. The other three electrodes are grounded.

## 5 Measurements and Results

- The pressure is minimal, i.e. below  $10^{-6}$  mbar. When pressure is the observed variable, it is done with deuterium. The pressure is measured with the Baratron pressure gauge.

This is the standard configuration, that is valid for the variables except the one that is measured. However, the configuration of every measurement is separately listed with the results. During all measurements the picoammeter was used in a scale, where it is precise to 0.1 nA. For each measurement the readout was stable, so that usually the error bars are smaller than the printed dots in the plots.

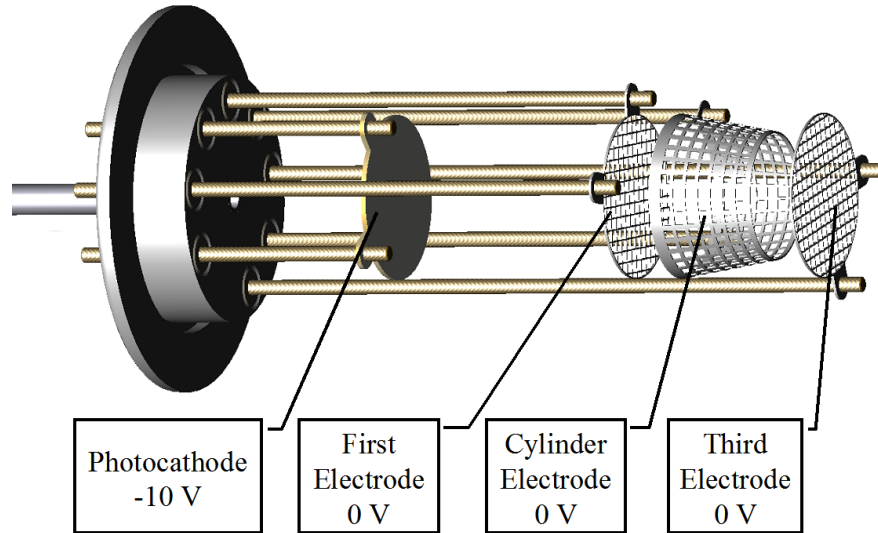


**Figure 5.1: Standard potential distribution for the electron production.** The photocathode is put on negative potential, -10 V. The other three electrodes are grounded, 0 V.

## 5.1.2 Dependencies of Electron Current

### 5.1.2.1 Photocathode Material

Prior to any measurements the three different types of photocathodes have been tested in terms of electron production. All three photocathodes have been installed subsequently in the ion source and tested under the standard conditions mentioned above. The according electron current measurements are listed in the following table.

**Table 5.1: Results of different Photocathodes**

<b>Material</b>	<b>Electron Current</b>
Stainless Steel	3.4 nA
Copper	112 nA
Aluminum	4.6 nA

This is contradictory to the data on page 56, where the stainless steel is expected to have the highest quantum efficiency and therefore the highest electron current. Since it is the aim of the prototype ion source to prove the chosen principle of ionization process, the properties of the different photocathodes have not been investigated any further. Thus, all further experimental data was collected with the copper photocathode.

However, the reached efficiency seems to be age dependent, i.e. with longer gas exposure the reached electron currents can decrease. This means that a copper photocathode is possible but not optimum for long term operation. Therefore, the choice of the photocathode material for the upscaled test ion source needs further research. Possible alternatives are stainless steel, gold or nickel.

**5.1.2.2 Light Intensity**

The lamp's intensity can be varied by the current supply. The lamp's power supply permits the continuous adjustment of the intensity on a range between 0 – 20 mA, where the only indicated ticks are 0, 10 and 20 mA, so that fine-scaling is difficult. Hence, the x-scale error bars were estimated to  $\pm 1$  mA. The current measurement itself is precise to 0.1 nA, i.e. that the y-scale error bars are smaller than the printed dots.

By varying the supply current, the light intensity is changed. This changes the amount of photoelectrons, which is measured. Thus, two different things are measured at the same time: The relation between supply current and lamp intensity as well as the relation between lamp intensity and electron current.

**Table 5.2: Configuration for Electron Current over Lamp Intensity.**

pressure $p$	magnetic field $B_{\text{center}}$	$B_{\text{ph.c.}}$	lamp current $I_L$
$< 10^{-6}$ mbar	145 mT	28 mT	<i>var.</i>

**Table 5.3: Potential Distribution for Electron Current over Lamp Intensity.**

photocathode $U_{\text{ph.c.}}$	first grid $U_{\text{ee}}$	cylinder $U_{\text{cyl}}$	last grid $U_{\text{ie}}$
-10 V	0 V	0 V	0 V

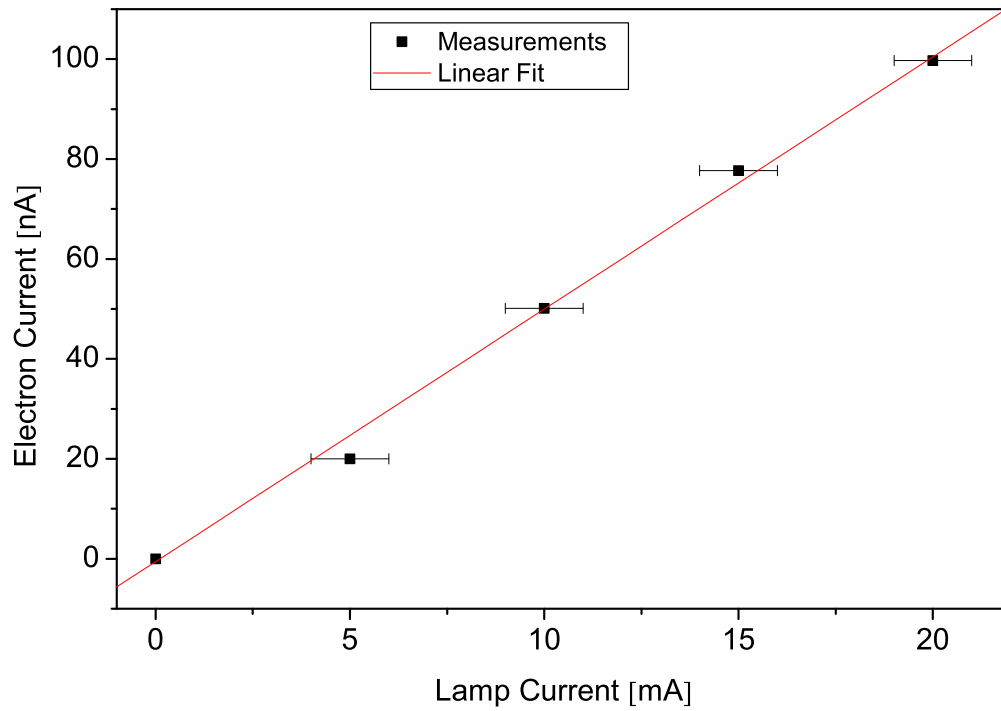


**Figure 5.2: Electron Current over Lamp Intensity.** The amount of photoelectrons is proportional to the lamp's current. The number of emitted electrons is expected to be linearly proportional to the light's intensity. Thus, it can be assumed that the light intensity is proportional to the lamp current. Since the electron current should be as high as possible, the standard setup for other measurements is a lamp current of 20 mA.

**5.1.2.3 Magnetic Field**

The magnetic field is controlled by the power supply, i.e. the applied current. The maximum current is 175 A, corresponding to 145 mT in the center of the coil. The according magnetic field at the photocathode is 19.4 % of the maximum at the center. For the measurements the error is estimated to be 1 A ( $\sim 0.8$  mT), so that the error bars are smaller than the printed dots.

By varying the supply current, the magnetic field strength is changed. A stronger magnetic field reduces the cyclotron radius of the electrons. This means, that collisions with the walls and meshes get rarer. Therefore, the electrons should be guided more efficiently along the beamline. Thus, more electrons should reach the Faraday cup and the measured current should increase.

**Table 5.4: Configuration for Electron Current over Magnetic Field.**

pressure $p$	magnetic field $B_{\text{center}}$	$B_{\text{ph.c.}}$	lamp current $I_L$
$< 10^{-6}$ mbar	<i>var.</i>	<i>var.</i>	20 mA

**Table 5.5: Potential Distribution for Electron Current over Magnetic Field.**

photocathode $U_{\text{ph.c.}}$	first grid $U_{\text{ee}}$	cylinder $U_{\text{cyl}}$	last grid $U_{\text{ie}}$
-10 V	0 V	0 V	0 V

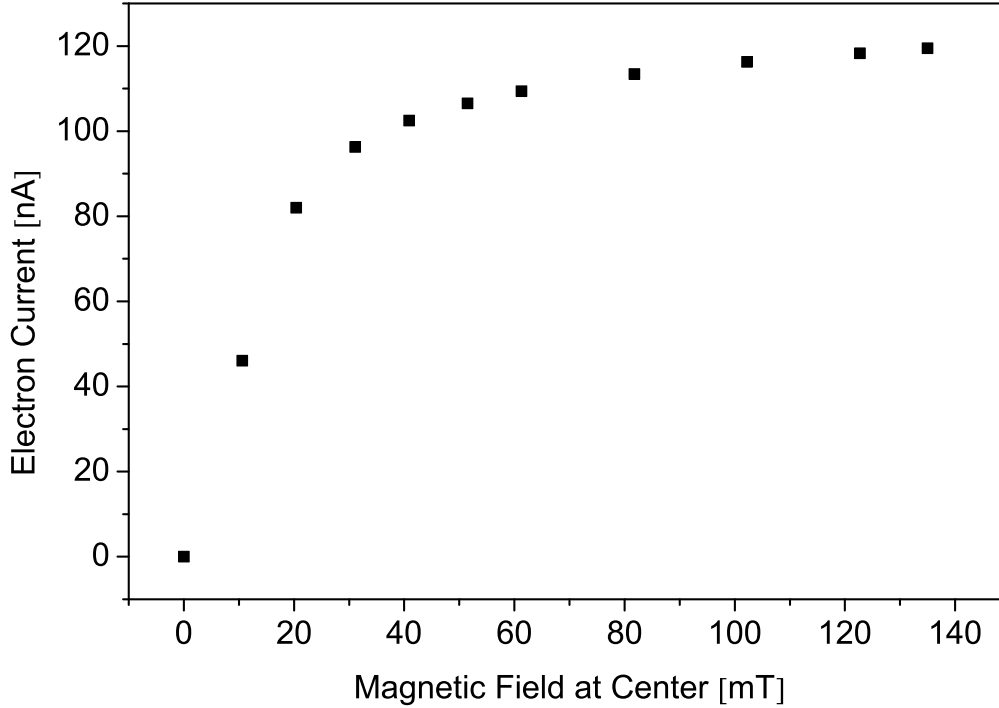


**Figure 5.3: Electron Current over Magnetic Field.** The absence of a magnetic field, 0 mT, results in a measured electron current of 0 nA. Although the electrons are emitted from the photocathode and are accelerated by a 10 V potential difference, they do not reach the Faraday cup. As the electrons are not guided, they follow their starting momentum and are absorbed by either the vacuum chamber or one of the grids.

Computational simulations have shown another reason for the magnetic field dependence [Glü08]. For small magnetic fields  $B_{\text{center}} \leq 50 \text{ mT}$  ( $B_{\text{ph.c.}} \leq 10 \text{ mT}$ ) the electron motion near the cathode is not adiabatic. This results in a non-adiabatic conversion of the longitudinal energy into transversal energy (cyclotron motion). Therefore, the changes for reflection by the magnetic mirror effect is increased.

With increasing field strength, the electron motion is adiabatic and the electron current saturates for  $B \gtrsim 100 \text{ mT}$ . The decreasing cyclotron radius increases the efficiency of the guidance field. Collisions with bulk material become rarer. The presence of a magnetic field is crucial for the effectiveness of the electron production. Therefore, the standard setup for other measurements is 145 mT.

**5.1.2.4 Photocathode Potential**

The potential at the photocathode is applied by a power supply through the electrical feed-throughs. Again, the error bars are too small to be printed, 0.1 V and 0.1 nA.

As the UV-lamp shines on the photocathode, photoelectrons are emitted into the general direction of the Faraday cup, i.e. downstream. Photoelectrons are usually emitted in an arbitrary direction. However, they are not emitted isotropically, but follow an angular distribution. Depending on their pitch angle their further movement is determined. If they are emitted (almost) parallel to the magnetic field lines, they can enter the region of higher magnetic fields. If their pitch angle is large toward to the magnetic field line, they will be reflected by the magnetic mirror effect. Thus, most of them cannot overcome the magnetic mirror effect, if they are not accelerated.

By accelerating them along the beamline more electrons should overcome the magnetic mirror effect and reach the Faraday cup. This is done by putting the photocathode on negative potential, so that the electrons gain energy, while traveling into the region of the grounded chamber. On the contrary, when putting the cathode on positive potential, all electrons with smaller energy are drawn back to it.

**Table 5.6: Configuration for Electron Current over Cathode Potential.**

pressure $p$	magnetic field $B_{\text{center}}$	$B_{\text{ph.c.}}$	lamp current $I_L$
$< 10^{-6}$ mbar	145 mT	28 mT	20 mA

**Table 5.7: Potential Distribution for Electron Current over Cathode Potential.**

photocathode $U_{\text{ph.c.}}$	first grid $U_{\text{eex}}$	cylinder $U_{\text{cyl}}$	last grid $U_{\text{ieex}}$
var.	0 V	0 V	0 V

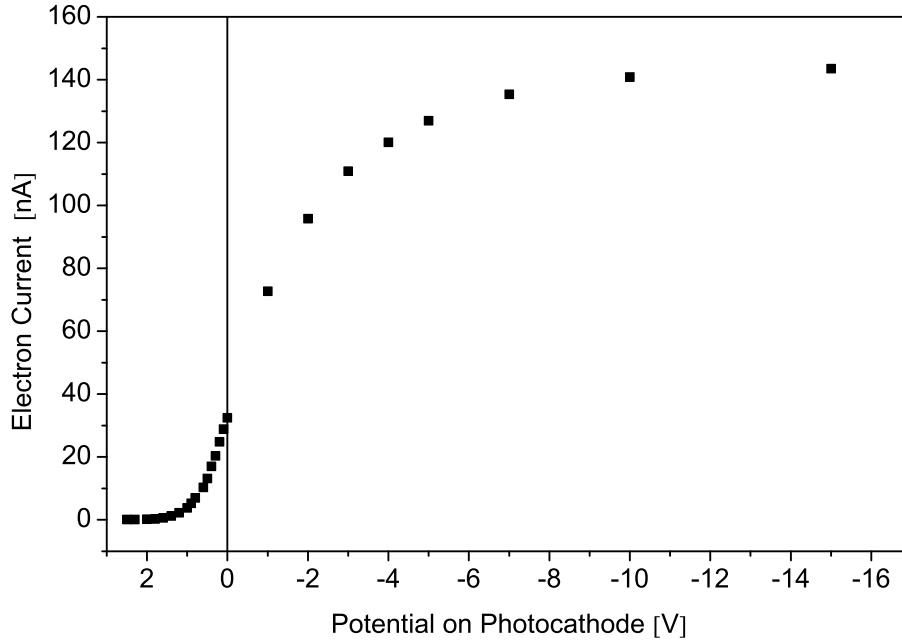


**Figure 5.4: Electron Current over Cathode Potential.** A negative potential rejects the electrons from the photocathode; a positive potential attracts them. At zero potential of the photocathode only the electrons with a small angle of momentum towards the beamline axis reach the Faraday cup, here 32.5 nA. With increasing negative potential the momentum of the electrons is changed and becomes smaller compared to the beamline axis. Therefore, more electrons can pass the magnetic mirror. The percentage of electrons that overcome the magnetic mirror effect is saturated in the region of  $-10$  V and above.

The results for positive potentials are unexpected. The positive potential  $|eU|$  that is needed to zero the electron current normally equals the initial energy of the electrons, and therefore equals the difference of photon energy and the photocathode's work function. Here, it takes about  $+2$  V to attract all electrons back to the photocathode. However, the maximum photon energy is still 4.9 eV, while the photocathode's work function is about 4.7 eV. This means, that the maximum starting energy of the electrons is expected to be about 0.2 eV, so that a retarding potential of 0.2 V should zero the electron current. A similar behavior is known from vacuum tubes, where a space charge can shield the cathode from the retarding potential [Vog95]. Calculations have shown, that the space charge for this measurement is in the order of magnitude of 3 mV [Glü08]. This is not enough to explain the observed behavior.

Since the electron current should be as high as possible, the standard setup for other electron measurements is a photocathode potential of  $-10$  V.

### 5.1.2.5 Pressure

The pressure in the vacuum chamber can be varied with an electronic control valve. This valve connects the vacuum chamber to the deuterium buffer vessel. A voltage supply is connected to the valve and controls it. When the deuterium gas flows through the ion source, the pressure in the vacuum chamber is measured by the Baratron pressure gauge. It has a range of  $10^{-6} - 10^{-1}$  mbar and is precise to 1 %. As the deuterium gas is permanently pumped, the valve stays open during the measurement. For this measurement the pressure is varied between  $5 \cdot 10^{-5} - 5 \cdot 10^{-3}$  mbar. Since the pressure cannot be readjusted or readout during a measurement<sup>1</sup>, the errors of the pressure values are estimated to 10 %.

At the standard pressure of  $10^{-6}$  mbar the mean free path of the electrons is several meters, which is large compared to the dimensions of the vacuum chamber. With rising pressure the mean free path gets smaller, because of the increasing scattering rate of the electrons with gas molecules. The collisions may cause a change of direction of the electrons. Since the electrons are bound to the magnetic field lines, the new momentum of the electron may point it downstream or upstream along the field lines. Thus, the energy transfer is of secondary importance, i.e. if the scattering is elastic or inelastic. However, at higher pressures the number of electrons, which reach the Faraday cup, should decrease.

When the electrons are inelastically scattered, they may loose energy not only to ionization, but also to excitation processes. Then it is possible, that their kinetic energy is not sufficient for further ionization. Thus, the number of electrons, that could possible ionize, decreases with rising pressure. This is important for the ion production, because the ionization probability  $P$  is proportional to the pressure. Still, no ions are produced in this measurement, because the energy of the electrons is below the ionization threshold. Hence, the measured current consists only of electrons and no ions.

**Table 5.8: Configuration for Electron Current over Pressure.**

pressure $p$	magnetic field $B_{\text{center}}$	$B_{\text{ph.c.}}$	lamp current $I_L$
<i>var.</i>	145 mT	28 mT	20 mA

**Table 5.9: Potential Distribution for Electron Current over Pressure.**

photocathode $U_{\text{ph.c.}}$	first grid $U_{\text{eex}}$	cylinder $U_{\text{cyl}}$	last grid $U_{\text{ieex}}$
-10 V	0 V	0 V	0 V

<sup>1</sup>Due to the malfunction of the Baratron pressure gauge, as described in 4.4.1 on page 66.

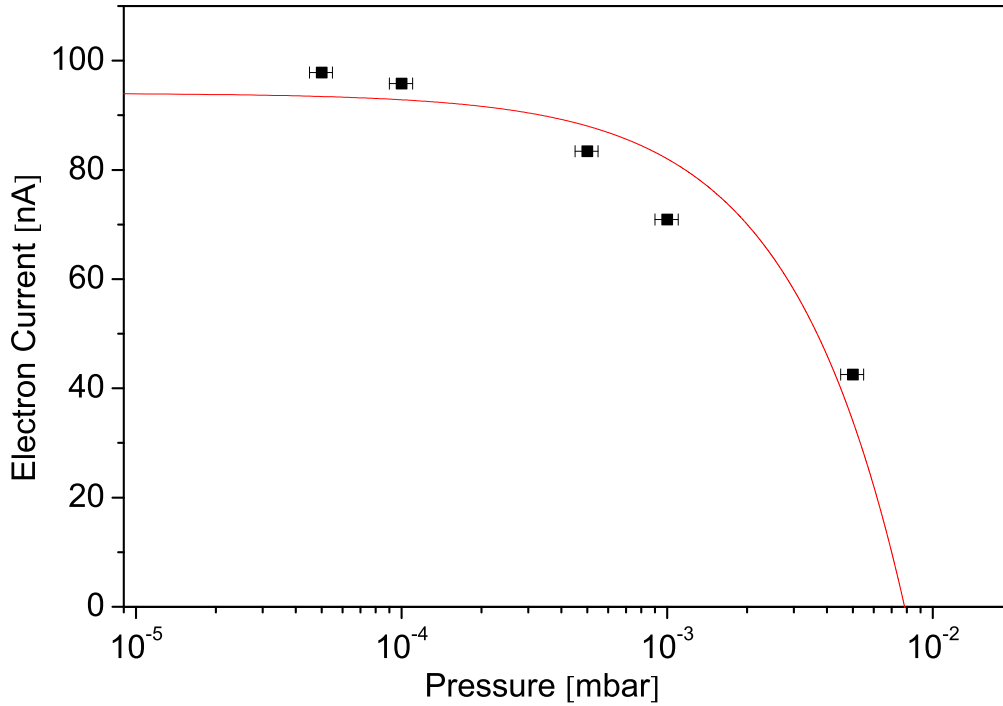


**Figure 5.5: Electron Current over Pressure.** The deuterium pressure inside of the vacuum chamber determines the number of electrons that reach the Faraday cup. The mean free path of particles is anti-proportional to the particle density,  $\lambda_{\text{free}} \sim 1/n$ . Therefore, it is also antiproportional to the pressure,  $\lambda_{\text{free}} \sim 1/p$ . However, the above measurements do not follow the  $1/p$  shape. Electrons of energies  $E \approx 10 \text{ eV}$  have a large cross section of  $\sigma_{\text{elast}} \approx 10^{-15} \text{ cm}^2$  for elastic scattering, which is about ten times higher than the according cross section for inelastic scattering [Tra83]. Therefore, elastic scattering dominates for this measurement. The electrons do not vanish after a collision. The angular distribution of the electron scatterings in this energy range is nearly isotropic. After elastic scatterings with large angles ( $> 90^\circ$ ) the electrons can be reflected, so they do not reach the Faraday cup. An increased number of elastic collisions, increases the chances, that an electron is reflected on its way along a magnetic field line. Based on the cross section for elastic scattering of  $\sigma_{\text{elast}} \approx 10^{-15} \text{ cm}^2$  calculations (solid red line) confirm this explanation [Glü08].

## 5.2 Ion Production

The understanding of the ion production mechanism is the main goal of this work. Therefore, this process and the related measurements are discussed in detail. Analogue to the previous measurements of the electron current the dependencies of pressure, magnetic field and potential distribution are investigated. Furthermore the importance of the gas flow as a transport mechanism for the ions is evaluated. With the present electrode geometry the ion source can also work in a Penning discharge mode. Because of the instability of such a discharge it is an unfavored operating mode. Therefore, the conditions for this mode are also examined.

### 5.2.1 Experimental Procedure

The absolute amount of the ion current, that reaches the Faraday cup and therefore can be measured, is dependent on several variables. In addition to the standard configuration for the electron production, the electrode potentials are also varied. Hence, a standard configuration for the ion production is now introduced, that determines all values, except the one that is measured. In this way the different measurements become more comparable. These standard values come from the experience of several test runs. It results in a measured ion current of 2 nA.

The standard configuration for electron production is:

- The UV-lamp is working at its maximum of 20 mA.
- The material of the photocathode is copper.
- The magnetic field is set to its maximum, i.e. 145 mT in the center, to decrease the cyclotron-radius of the ions. This corresponds to 28 mT at the photocathode.
- The standard potential distribution for the ion production has been arbitrarily chosen. The photocathode potential is not varied during the potential measurements, only different potentials of the electrodes are examined. Thus, the potential of the photocathode is always +5 V<sup>2</sup>. The other three potentials are examined in order to maximize the ion current and understand their role in the ion production. The standard potential of each electrode was determined during test runs:
  - Electron Extraction Electrode:  $U_{\text{ex}} = 25 \text{ V}$
  - Cylinder Electrode:  $U_{\text{cyl}} = 200 \text{ V}$
  - Ion Extraction Electrode:  $U_{\text{dex}} = 60 \text{ V}$

---

<sup>2</sup>If the photocathode is on a higher potential than the (grounded) vacuum chamber, the produced electrons cannot move into the downstream region behind the electrode system.

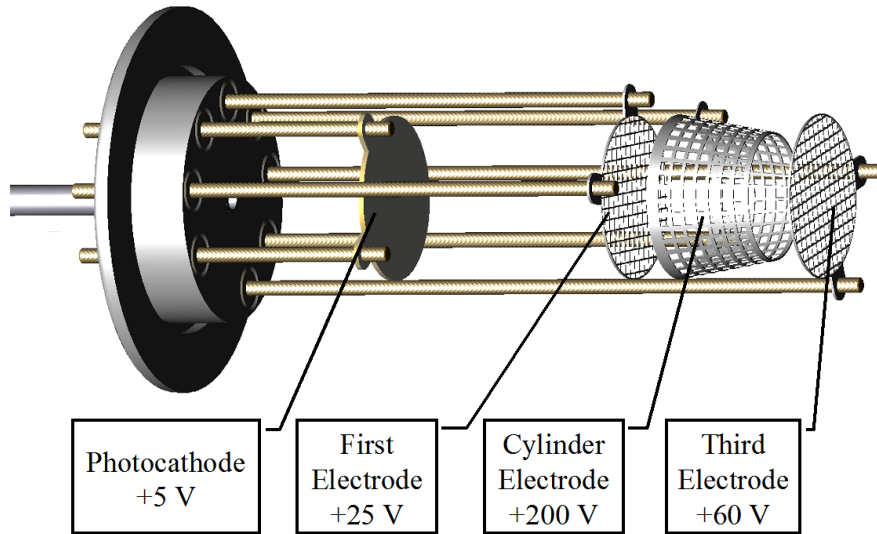


**Figure 5.6: Standard potential distribution for the electron production.** The photocathode is put on positive potential, +5 V, to prevent the electrons from reaching the (grounded) Faraday cup. The three other electrodes have higher potentials as described in the text.

- In any case the experiment needs a deuterium supply to produce deuterium ions. The standard pressure in the ionization region is  $10^{-4}$  mbar. Then the behavior of the gas follows the molecular flow<sup>3</sup>. The pressure is measured with the Baratron pressure gauge.

The current measurement is taken by the same picoamperemeter. If the error bars are too small to be drawn in the plots, they will be given in the description.

<sup>3</sup>This is the case when the mean free path is longer than half of the chamber diameter:  $\lambda > \frac{d}{2}$ .

## 5.2.2 Dependencies of Ion Current

### 5.2.2.1 Magnetic Field Dependence

The magnetic field is controlled by the power supply, i.e. the applied current. The maximum current is 175 A, corresponding to 145 mT in the center of the coil. The according magnetic field at the photocathode is 19.4 % of the maximum at the center. For the measurements the error is estimated to be 1 A ( $\sim 0.8$  mT), so that the error bars are smaller than the printed dots.

When colliding with other gas molecules, the ions may be forced to leave their original field line due to momentum transfer. This may lead to a collision with bulk material and therefore to the neutralization of the ion. With increasing magnetic field, the cyclotron radius of the ions (and the electrons) is reduced and therefore also the number of collision of ions with other molecules. The presence of a magnetic field increases the efficiency of electron and ion measurements.

The magnetic field dependence of the ion current has been measured for two different pressures.

**Table 5.10: Configuration for Ion Current over Magnetic Field.**

pressure $p$	magnetic field $B_{\text{center}}$	$B_{\text{ph.c.}}$	lamp current $I_L$
$< 10^{-4}$ mbar	<i>var.</i>	<i>var.</i>	20 mA

**Table 5.11: Potential Distribution for Electron Current over Magnetic Field.**

photocathode $U_{\text{ph.c.}}$	first grid $U_{\text{ee}}$	cylinder $U_{\text{cyl}}$	last grid $U_{\text{ie}}$
+5 V	+25 V	+200 V	+60 V

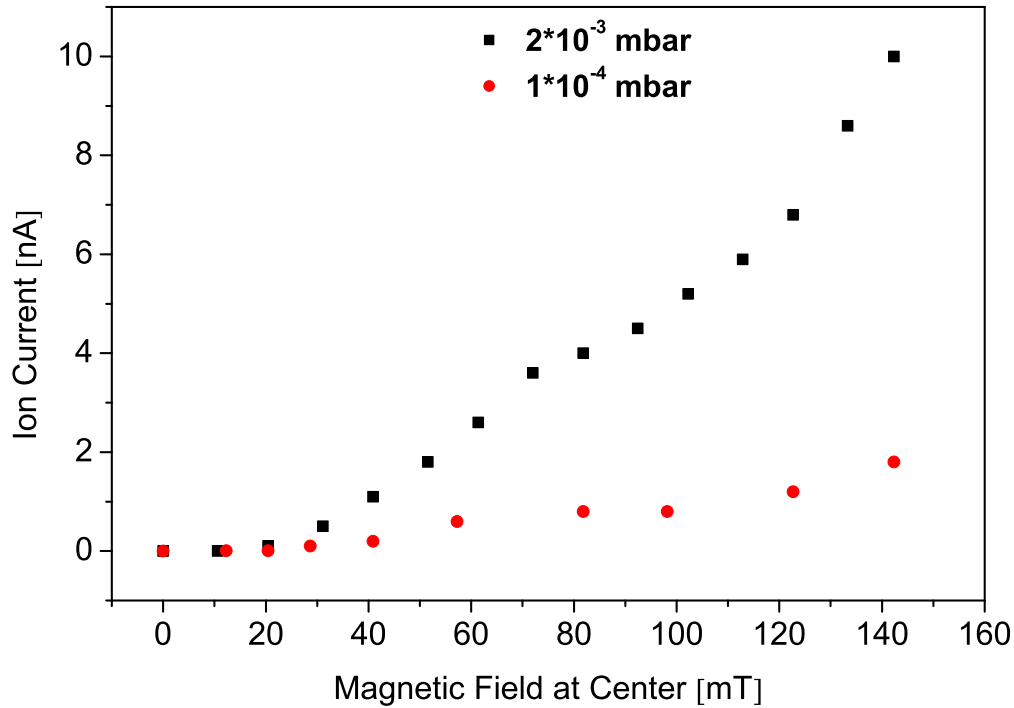


**Figure 5.7: Ion Current over Magnetic Field.** The magnetic field does not only influence the movement of the ions, but also the movement of the electrons. In the absence of a magnetic field neither electrons nor ions are guided along the beamline. Therefore, no current is measured at the detector in this case.

For increasing magnetic field strength the ion current rises. Calculations have shown that the movement of the ions in the magnetic field gradient is non-adiabatic and therefore cannot overcome the magnetic mirror effect. It is even possible that they do not follow the magnetic field lines as their cyclotron radius can become too large. The non-adiabatic motion happens especially at smaller magnetic fields, but is also present for higher fields.

### 5.2.2.2 Potential Dependence

Each of the four electrodes can be operated on different potentials. The potentials are controlled by different voltage supplies. The photocathode is on a constant potential. Experiences have shown that it is optimum for the effective ion current, when the photocathode potential is between +2 V and +5 V. Therefore, +5 V is the standard configuration for all ion production measurements.

The electron extraction electrode is supposed to accelerate the photoelectrons from the cathode to the downstream region. With higher electron extraction potentials more electrons should overcome the magnetic mirror and reach the ionization region. If the electron extraction potential becomes too high, the electrons may gain energy too early, so that they would ionize gas molecules before the actual ionization region. Ions, that are created too early, will not move downstream, but to the photocathode. Therefore, the electron extraction potential must be high enough to guide the electrons downstream, but also small enough to prevent early ionization processes.

The cylinder electrode supplies the electrons with the energy, which they need to ionize the deuterium molecules. The highest cross section is achieved for electron energies of about 70-80 eV. However, at higher energies of a few hundred electronvolt the electrons should be able to do multiple ionizations. The optimum ratio between high cross section and multiple ionizations has to be determined to maximize the ion current.

The ion extraction electrode should confine the electrons and enable the ions to leave the ionization region with the downstream gas flow. Therefore, the potential of this electrode must be below the positive potential of the cylinder (to confine the electrons). However, if the electrode potential becomes too high, the ions will be reflected and gathered in the ionization region.

**Table 5.12: Configuration for Ion Current over Potential Distribution.**

pressure $p$	magnetic field $B_{\text{center}}$	$B_{\text{ph.c.}}$	lamp current $I_L$
$< 10^{-4}$ mbar	145 mT	28 mT	20 mA

**Table 5.13: Potential Distribution for Electron Current over Potential Distribution.**

photocathode $U_{\text{ph.c.}}$	first grid $U_{\text{eex}}$	cylinder $U_{\text{cyl}}$	last grid $U_{\text{ieex}}$
+5 V	<i>var.</i>	+200 V	+60 V
+5 V	+25 V	<i>var.</i>	+60 V
+5 V	+25 V	+200 V	<i>var.</i>

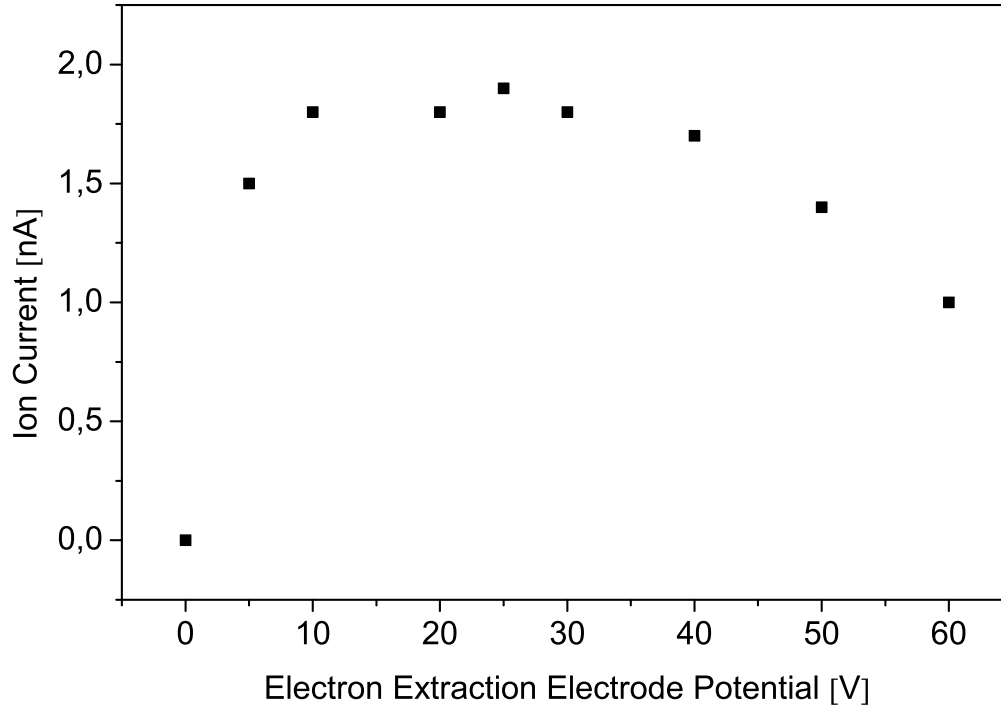


**Figure 5.8: Ion Current over Electron Extraction Electrode Potential.** When the potential of the electron extraction electrode is 0 V, the electrons cannot leave the photocathode, which is on a potential of +5 V. Therefore, neither electrons nor ions are measured at the detector.

Higher potentials between 5-40 V are most efficient to guide the electrons to the ionization region. This is congruent to the photocathode potential dependence of the electron production, where the electron current also saturates above 10 V.

For higher energies of the electrons ( $\gtrsim 50$  eV), the cross section for ionization becomes higher. Thus, the ionization of deuterium is possible before the actual ionization region. Any ions, that are produced in the region between photocathode and first electrode are attracted to the photocathode and cannot move downstream.

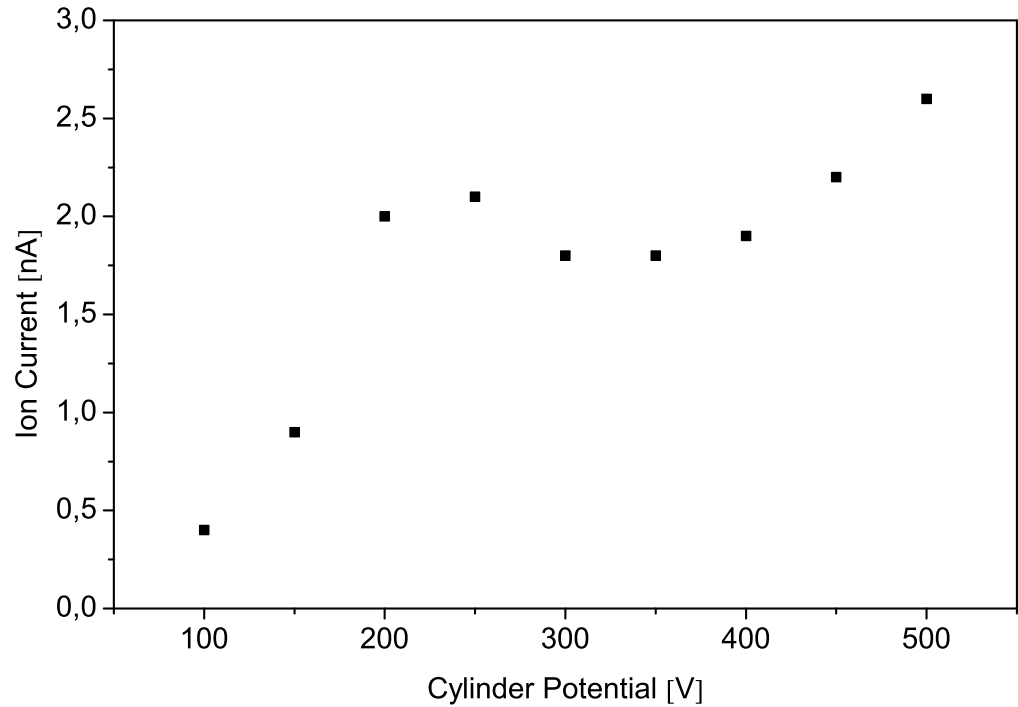


**Figure 5.9: Ion Current over Cylinder Potential.** The ion current is examined for cylinder potentials between 100-500 V. In this range the cross section for ionization is maximum for electron energies of 100 eV. However, the measured ion current increases at higher potentials. In the case of higher potentials, the cross section is smaller, but the electrons receive enough energy to do multiple ionizations. Therefore, the absolute ion current increases for higher potentials. Between 200-250 V the decreasing cross section and the increasing rate of multiple ionizations seem to result in a local maximum of the ion current. For a potential of  $U > 250$  V the cross section becomes smaller and the trapping possibility decreases as the electrons tend to get reflected back to the photocathode. This was confirmed by calculations [Glü08]. For higher potentials of  $\geq 450$  V the measured ion current increases and a non-self-maintained discharge is possible.

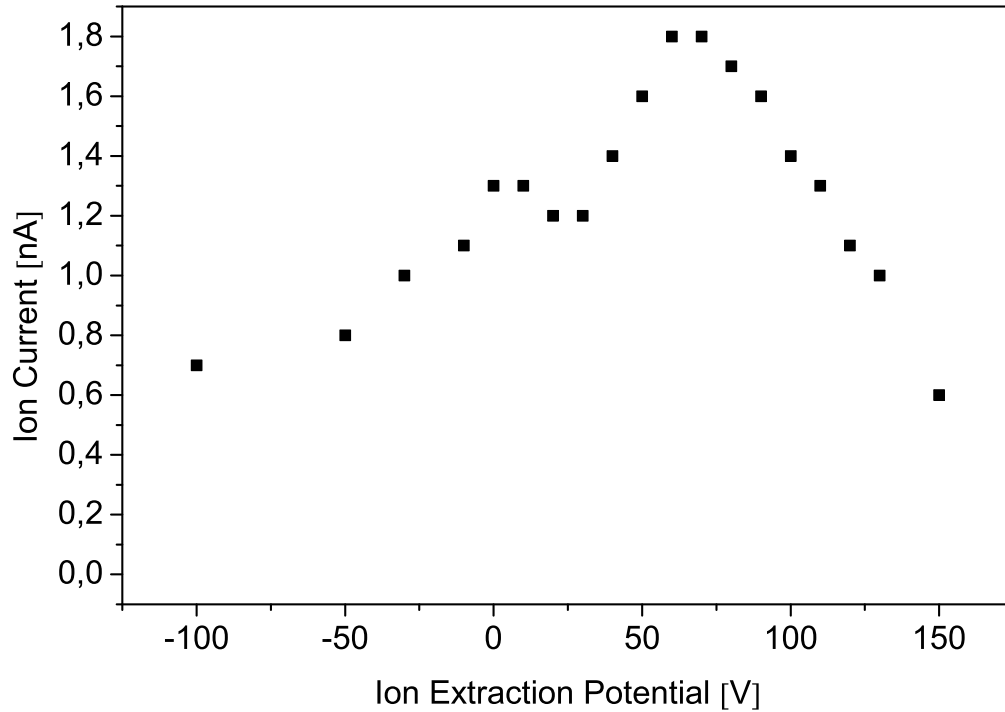


**Figure 5.10: Ion Current over Ion Extraction Electrode Potential.** The potential of the ion extraction electrode has been varied between -100 V and +150 V.

A negative potential on this electrode attracts the ions coming from the ionization region and should prevent them from reaching the detector. Still, some ions can overcome the negative potential by moving downstream with the gas flow. This shows, that the gas flow works as a transport mechanism for the ions.

At a potential of 0 V the ions can leave the ionization region in the direction of the detector.

For positive potentials the ions can still leave the ionization region, as long as the potential is below the cylinder potential (200 V). Furthermore, the effective path length of the electrons is increased, as they can pass the positive potential and are reflected further downstream by the grounded chamber. The maximum ion current is reached at 60-70 V.

### 5.2.2.3 Pressure Dependence

The pressure in the vacuum chamber can be controlled with an electronic needle valve. The absolute pressure in the ionization chamber is measured by the Baratron pressure gauge. It has a range of  $10^{-6} - 10^{-1}$  mbar and is precise to 1 %. As the deuterium gas is permanently pumped, the valve stays open during the measurement. For this measurement the pressure is varied between  $5 \cdot 10^{-5} - 5 \cdot 10^{-2}$  mbar. Since the pressure cannot be readjusted or readout during a measurement<sup>4</sup>, the errors of the pressure values are estimated to 10 %.

The following influences of the pressure on the ion current are possible:

- The ionization probability is proportional to the particle density and therefore also to the pressure<sup>5</sup>. Hence, more ions are produced and a rise in the ion current is expected for increasing pressure.
- The transport of ions by the gas flow is expected to be more efficient for higher pressures. Hence, more of the produced ions reach the detector and a rise in the ion current is expected for increasing pressure.
- The probability for collisions of ions with gas molecules increases with rising pressure. Hence, ions may be pushed to the wall of the vacuum chamber and neutralized. This would result in a decrease of the measured ion current.

For a rising pressure these effects will result in a general increase of the measured ion current. Furthermore, the influence of the gas flow on the ion current is examined. Measurements with and without gas flow are conducted in order to show the importance of the gas flow for the ion transport along the beamline.

**Table 5.14: Configuration for Ion Current over Pressure.**

pressure $p$	magnetic field $B_{\text{center}}$	$B_{\text{ph.c.}}$	lamp current $I_L$
<i>var.</i>	145 mT	28 mT	20 mA

**Table 5.15: Potential Distribution for Electron Current over Pressure.**

photocathode $U_{\text{ph.c.}}$	first grid $U_{\text{eex}}$	cylinder $U_{\text{cyl}}$	last grid $U_{\text{ieex}}$
+5 V	+25 V	+200 V	+60 V

<sup>4</sup>Due to the malfunction of the Baratron pressure gauge, as described in 4.4.1 on page 66.

<sup>5</sup>at a constant temperature

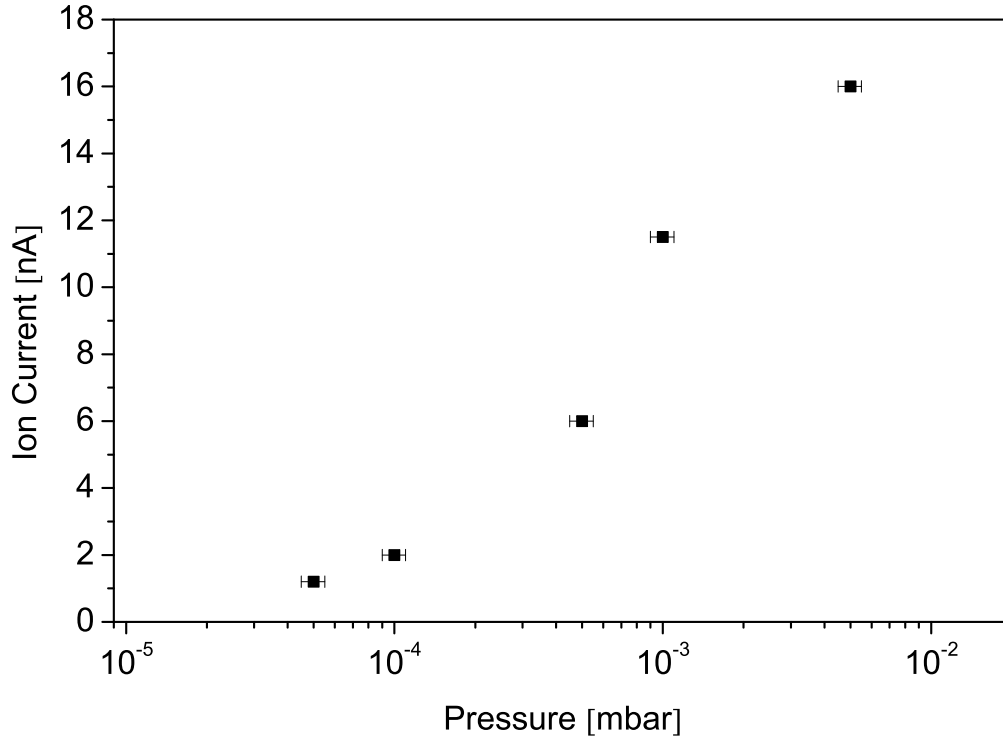


**Figure 5.11: Ion Current over Pressure.** The deuterium pressure inside of the vacuum chamber influences the mean free path of the electrons, the ionization probability and the movement of the ions.

The interpretation of these results is not straight forward, especially as the different pressures cause different types of flows: The viscous flow ( $\lambda \ll d$ ), the Knudsen flow ( $\lambda \approx d$ ), and the molecular flow ( $\lambda \gg d$ ) with  $\lambda$ : mean free path of the gas particles;  $d$ : diameter of the vacuum chamber.

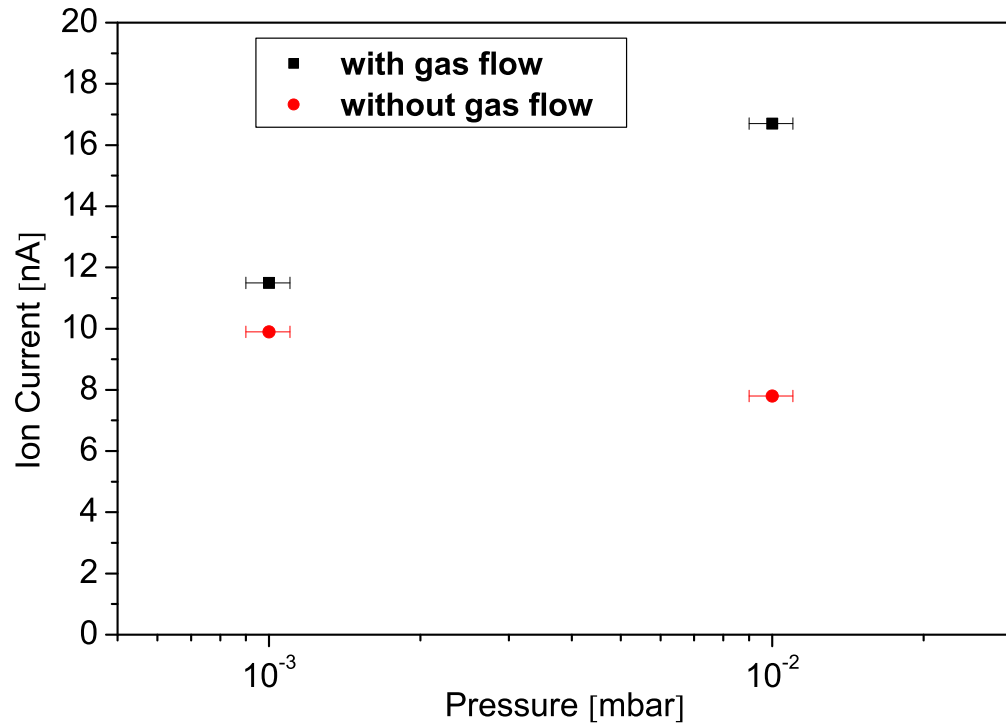


**Figure 5.12: Ion Current with and without Gas Flow.** The presence of a flow rate influences the measured ion current. Measurements with and without gas flow at the same absolute pressure are compared. The presence or absence of a gas flow has no major influence on the ion production itself, but on the ion transport to the detector.

At a pressure of  $10^{-3}$  mbar the presence of a gas flow has only little influence on the ion current on the Faraday cup. The general direction of the gas flow increases the ion current at the detector by about 15 %.

At a pressure of  $10^{-2}$  mbar the gas behaves viscous, therefore the transport by the gas flow is more important. Without gas flow the ions are trapped in the ionization region. With gas flow they are swept along the beamline. The measured ion current is increased by the gas flow by about 200 %.

#### 5.2.2.4 Penning Discharge

The design of the present prototype ion source enables an operation in a Penning discharge mode. Penning ion sources constitute an own class of ion sources, which usually produce high ion currents. The intensity of the produced ion beam usually fluctuates during the operation and the energy distribution of the ions is not sharp. Due to the properties of a Penning discharge, this kind of operation is unwanted. Therefore the conditions, which lead to a discharge are investigated. The variables that favor a Penning mode are high pressure, high potentials and strong magnetic field.

A self-maintained Penning discharge in the prototype ion source can be identified by the measurement of an unusual high current at the Faraday cup ( $I_{FC} \gg 100 \text{ nA}$ ). In fact currents of  $5 \mu\text{A}$  have been measured. A self-maintained Penning discharge has been measured under the following conditions:

- Pressure:  $3 \cdot 10^{-3} \text{ mbar}$
- Lamp intensity:  $20 \text{ mA}$
- Magnetic field:  $145 \text{ mT}$  at center
- Potential distribution:  $U_{\text{phc}} = 2 \text{ V}$ ,  $U_{\text{eex}} = 15 \text{ V}$ ,  $U_{\text{cyl}} = 500 \text{ V}$ ,  $U_{\text{tex}} = 40 \text{ V}$

Then it is possible, but not mandatory, that a Penning discharge ignites. It can be evidenced that it is a self-maintained discharge by varying the lamp intensity. When the lamp supply current is varied or even turned off, the measured ion current at the Faraday cup keeps constant, i.e. it is a self-maintained discharge.

Once the discharge maintains itself, it is possible to operate without an UV-lamp. However, the discharge is dependent on the magnetic field strength. When the magnetic field is gradually reduced and goes below about  $70 \text{ mT}$  in the ionization region, the discharge stops entirely. Increasing the magnetic field again above this threshold did not cause another ignition.

Although a discharge has been observed under the conditions mentioned above, it is not easy to reproduce. In the majority of the tests no discharge was found.

### 5.3 Discussion of Measurements

The results were separated in electron and ion measurements. The electron measurements showed that it is possible to produce electron currents of 100-140 nA. This corresponds to a particle current of about  $6 \cdot 10^{11} - 9 \cdot 10^{11}$  /s. With an assumed quantum efficiency for copper of about  $10^{-4}$  the number of incident photons can be estimated to be nearly about  $10^{16}$  /s. This is congruent with the predictions from Section 4.3.1. However, the understanding of the influences of potential, magnetic field and pressure on the measured electron current is not straight forward. First calculations have already supported the understanding and more are exercised at the moment [Glü08].

The ion measurements also confirmed the theoretical predictions from Section 4.2. There a total ion current of 8 nA was estimated for a pressure of  $10^{-3}$  mbar; typical values of the prototype ion source were measured to be 10-12 nA.

However, with an increased cylinder potential of 500 V and a pressure of  $10^{-3}$  mbar stable ion currents of  $>130$  nA were measured. The calculations have shown that the non-adiabatic motion of the charged particles in the magnetic field gradient of the ion source is responsible for a non-negligible reduction in the particle flow. This effect is reduced for higher magnetic field strengths [Glü08]. Since the final test ion source will be installed directly to the DPS2-F with its maximum magnetic field strength of 5.6 T, the non-adiabatic motion will be minimized.

The total ion flow rate is given by (cp. Section 4.2):

$$j_{ions} = I \cdot T \cdot QE \cdot P \quad (5.1)$$

The effects of the upscaling of the prototype to the test ion source are now estimated:

- Due to a stronger lamp the increase of the light intensity is estimated to be at least x10. This also increases the absolute amount of relevant photons  $I$  that reach the photocathode by the same factor.
- The total area of the photocathode will be increased by a factor of at least x40. This increases the absolute amount of relevant photons  $I$  that reach the photocathode by the same factor.
- The effects of a different photocathode material on the quantum efficiency still needs further investigation. Stainless steel, gold and nickel are recommended for long term operation under gas exposure, even if copper has shown a higher electron production capability.

Therefore, it can be concluded that it will be possible to produce the proper ion current for the DPS2-F with a photoelectron impact ion source. The following issues should be considered for the design of the upscaled test ion source:

- Since in the prototype setup the light from the UV-lamp comes from aside, the photocathode is not homogeneously illuminated. The part of the photocathode,

which is closer to the UV-lamp, receives more photons and therefore produces more electrons. Hence, also the ions follow this spatial distribution. There are several possibilities to control the homogeneity of the electron and ion distribution:

- The usage of two or more lamps (expensive).
  - The usage of a parabola mirror to change the light distribution.
  - The usage of a detector with spatial resolution to measure the electron/ion distribution.
- The poles that hold the photocathode and the electrodes in place are not cylinder symmetric and change the potential distribution of the whole system, e.g. the poles for the cylinder are on the same potential as the cylinder itself and are adjacent to the photocathode. A Faraday shielding of the poles should be considered.
  - Since the DPS2-F already includes devices to detect ions and measure the pressure, it could be possible to design the test ion source in a way that it consists of a flange, which can be directly installed to the DPS2-F entrance flange. In this case the magnetic flux tube is automatically covered. However, it would be necessary to illuminate the photocathode from behind, i.e. a thin gold layer on a window.

## 5 *Measurements and Results*

## 6 Summary and Outlook

The goal of the Karlsruhe Tritium Neutrino Experiment (KATRIN) is the determination of the neutrino mass in an absolute scale - i.e. it does not depend on theoretical models as for example the Standard Model of particle physics. The experiment is built on-site of Forschungszentrum Karlsruhe by an international collaboration. The aimed sensitivity of 0.2 eV is an improvement of one order of magnitude compared to the preceding experiments in Mainz and Troitsk. In order to achieve this goal, the tritium  $\beta$ -spectrum shape near the endpoint has to be precisely measured. For that, several technical and physical challenges have to be accomplished.

The high luminosity tritium source (WGTS) must create a highly stable column density to create a constant decay rate. All related parameters, i.e. pressure, temperature and tritium purity, must be known exactly down to  $10^{-3}$ . Then the electrons are guided by magnetic field lines along the beamline through the transport section, where at the same time the tritium flow is reduced by the factor of  $10^{14}$ . Finally the spectrometers work as an energetic high pass filter with high resolution and at extreme ultra high vacuum, in order to screen out all electrons that do not belong to the examined endpoint region. In order to minimize the background of the measurements the tritium has to be prevented from reaching the spectrometers. When it comes to the removal of tritium, one has to distinguish clearly between neutral and charged tritium, because the charged tritium is bound to the axial magnetic field of the beamline. The neutral tritium is removed with a combination of turbomolecular and cryogenic pumping. The charged tritium is observed by the FT-ICR and removed by a dipole electrode.

Before their application, these charged tritium reduction mechanisms need to be examined first - without the use of a tritium source. Therefore, a test ion source is needed, which imitates the output of the original tritium source in terms of gas flow rate, ion flow rate and similar types of ions.

The presented thesis demonstrated the successful proof of principle for a prototype ion source for the KATRIN experiment. First, the possibilities for the realization of this test ion source have been theoretically considered. Due to its similarity to tritium, deuterium is the working gas of choice. For the evaluation of the optimum ionization method the boundary conditions were determinative. The needed flow rate of deuterium ions of  $\approx 10^{11} - 10^{12}$  /s can best be reached by electron impact ionization. However, the deuterium ions must be distributed over the whole cross section area of the beamline. The presence of an axial magnetic field makes it necessary that the ions are already being created on the same field lines, which they are supposed to follow. Therefore, also the electrons, which are also bound to the field lines, must be produced on the same field lines. All charged particles, before and after the ionization process, are bound to the magnetic field line on which they were created and cannot leave it. This renders

## 6 Summary and Outlook

the electron production difficult, because they must be produced on an extensive area instead of on a common tip.

This gives rise to a new concept: The electron production for the electron impact ion source can be done via the photoelectrical effect. An ultraviolet lamp shines through a window into a vacuum chamber on a photocathode. The photocathode covers the same magnetic flux tube, on which the electrons and the ions should be distributed. Therefore, the photoelectrons are distributed across the cross section area of the flux tube.

The theoretical considerations showed, that the demand of electrons for the test ion source can be met with this principle. Since no other ion sources of this principle were found in the literature, the development and test of a prototype was necessary.

The design and setup of the prototype ion source included:

- The ionization device itself, consisting of
  - an UV-lamp,
  - the photocathode,
  - and an electrode system.
- A detector, i.e. a Faraday cup, to detect electrons and ions.
- A vacuum system with deuterium gas injection.
- A coil magnet to simulate the magnetic field of the DPS2-F.
- A slow control to readout the magnet's temperature and react to it.

As mentioned above, this ion source is meant as a prototype, i.e. a proof of principle from which an upscaled test ion source for the KATRIN transport section can be developed. The prototype has been tested in terms of electron and ion production. The presented measurements confirm the theoretical predictions and even exceed them in terms of absolute ion current.

The aim of 160 nA for the test ion source (for the DPS2-F) was not reached by the prototype ion source, but that was not intended anyway. Instead the predictions for the prototype ion source were about 8 nA of ion current at a working pressure of  $10^{-3}$  mbar. The results confirmed this with a measured ion current of about 12 nA. However, ion currents of  $>130$  nA could be reached with potentials of 500 V and a pressure of  $10^{-3}$  mbar.

The dependencies of the produced electron and ion currents from the variables pressure, magnetic field strength and potential distribution is not easy to understand. In the frame of this work the major part of the measurements could only be qualitatively explained. Since some of the interpretations have already been confirmed by calculations [Glü08], further understanding from computational methods is expected. These are currently under development.

On the basis of these calculations an upscaled test ion source for the KATRIN transport section will be designed. For this purpose the presented work can be used as a

guideline. The presented results let assume that the upscaled test ion source can achieve and even exceed its aim of 160 nA. Thus, the intended proof of principle was successful.

## *6 Summary and Outlook*

# Appendices

## A: List of Equipment

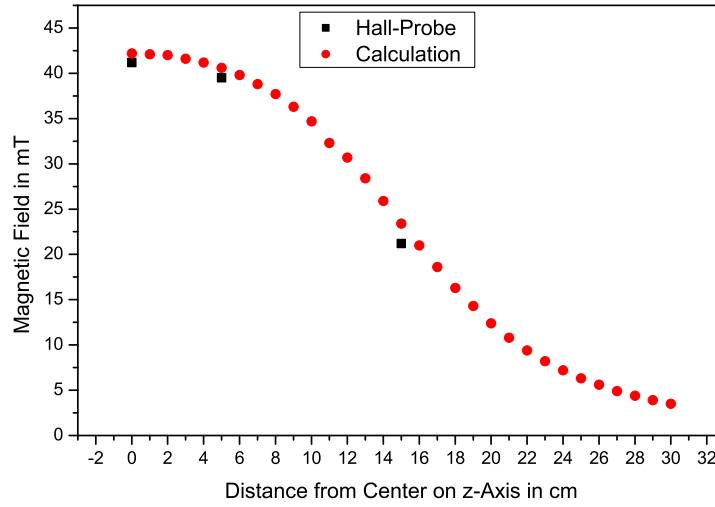
### Power Supplies

- Beha NG309: Photocathode Potential
- EA PS 2332-025: Electron Extraction Electrode Potential
- EA PSI 6150-01: Ion Extraction Electrode Potential
- Keithley 6487: Cylinder Electrode Potential, Faraday Cup Readout
- Lot-Oriel 6060: Pen-Ray Lamp Supply
- Agilent E3631A: Valve Supply and Control
- MKS Type 670: Baratron Supply and Readout
- Delta Elektronika SM 15-200D: Magnet Supply (2x)

### Vacuum Equipment

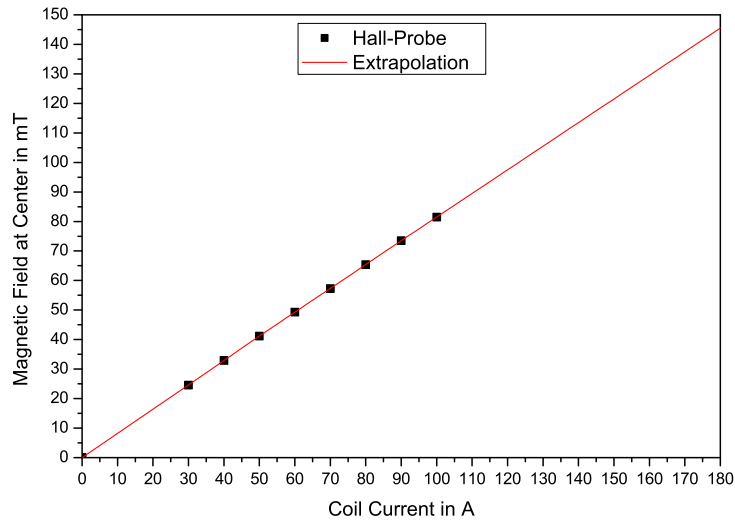
- MKS Type 148: Proportioning Solenoid Valve
- MKS Type 1249A: Valve Driver
- MKS Baratron 690A.1Tr: Pressure Gauge (Ion Source)
- Penning Pressure Gauge
- Pirani Pressure Gauge
- Combivac CM31: Penning / Pirani Supply and Readout

## B: Magnet Calibration



The field strength along the magnet's axis was checked with an hall probe and compared to calculations from Ferenc Glück in order to check for short circuits inside of the coil.

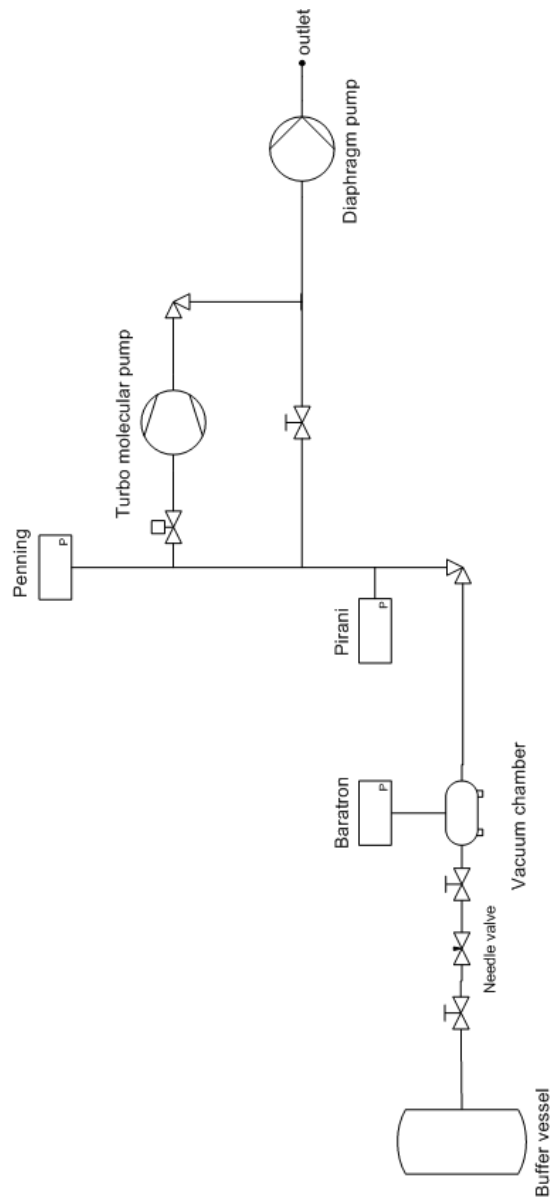
---



The linearity of the magnet has been calibrated with a hall probe and then extrapolated with a linear fit. The proportional factor is  $B = 0.82 \cdot I \cdot \left[ \frac{\text{mT}}{\text{A}} \right]$ .

### C: Flow Diagram of the Prototype Ion Source

# FLOW DIAGRAM PROTOTYPE ION SOURCE



## D: Technical Drawings

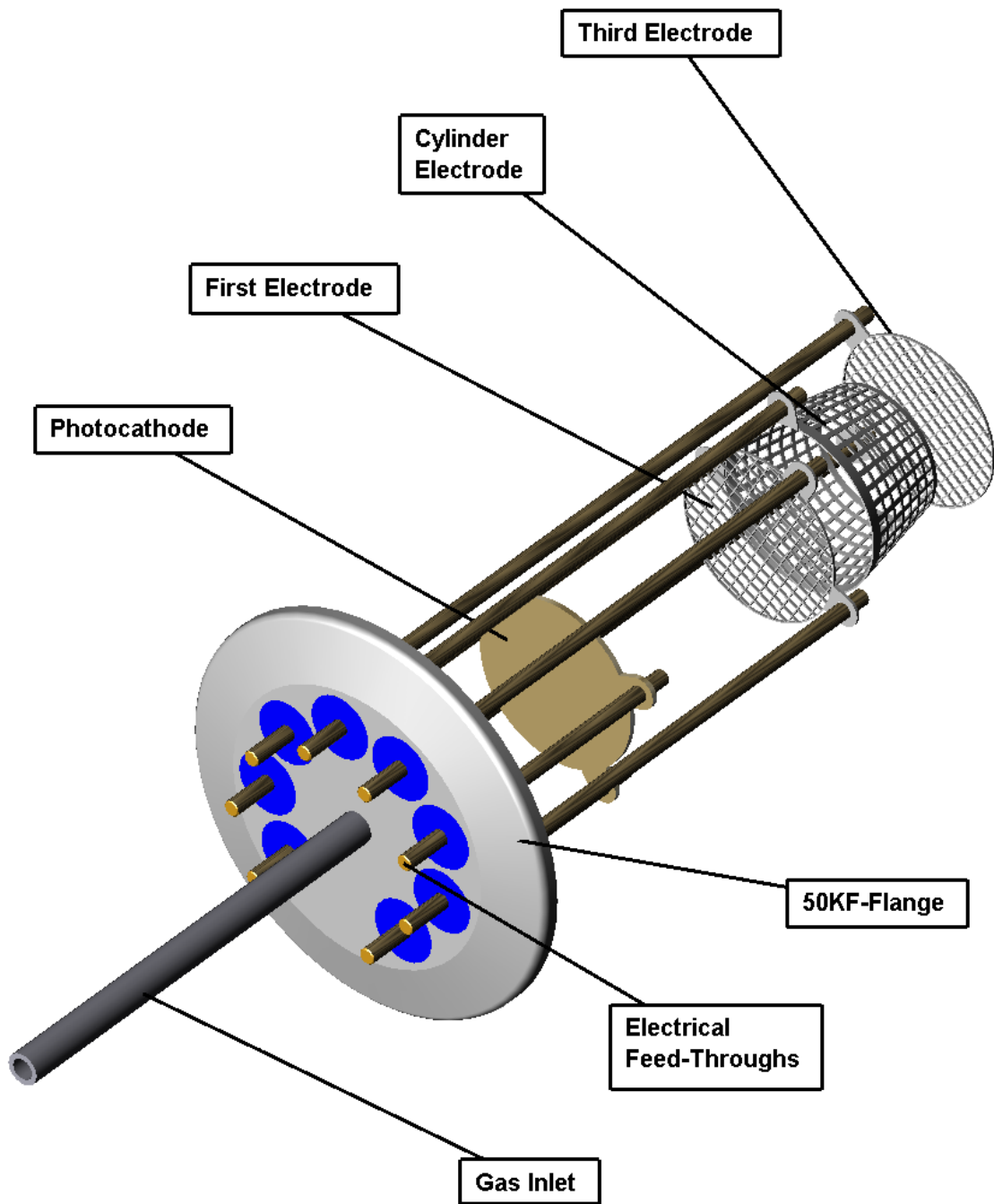


Figure 6.1: Drawing of Electrode System

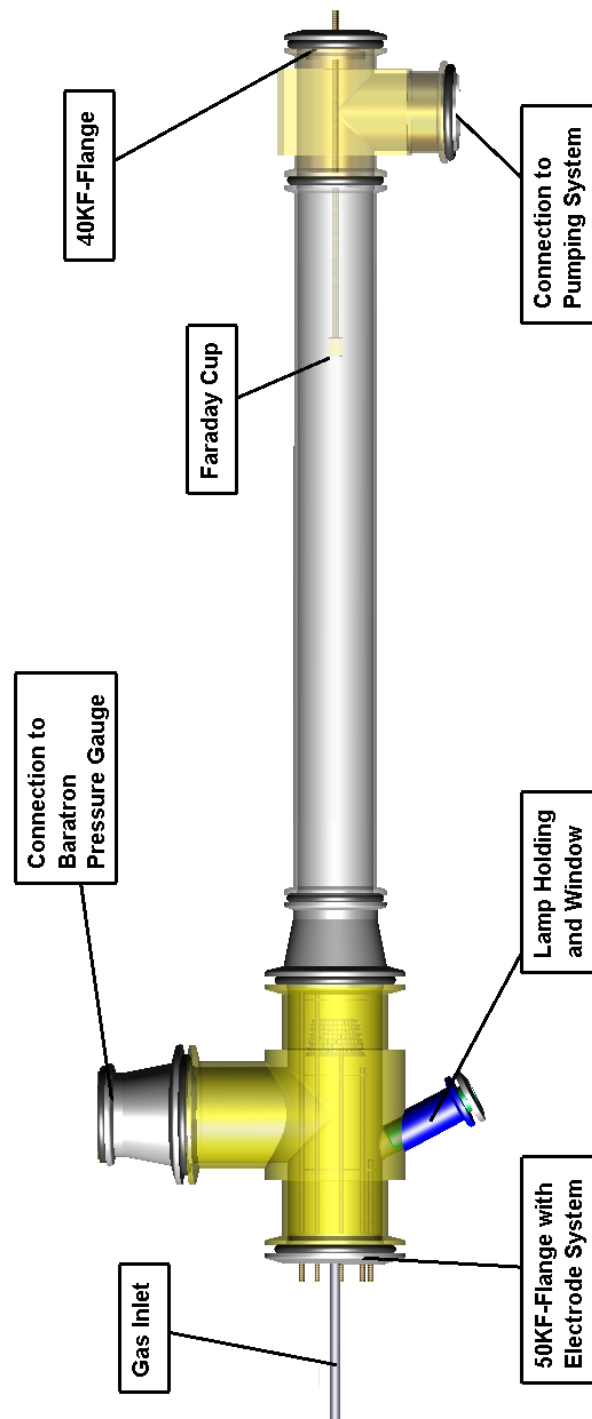


Figure 6.2: Drawing of Ion Source

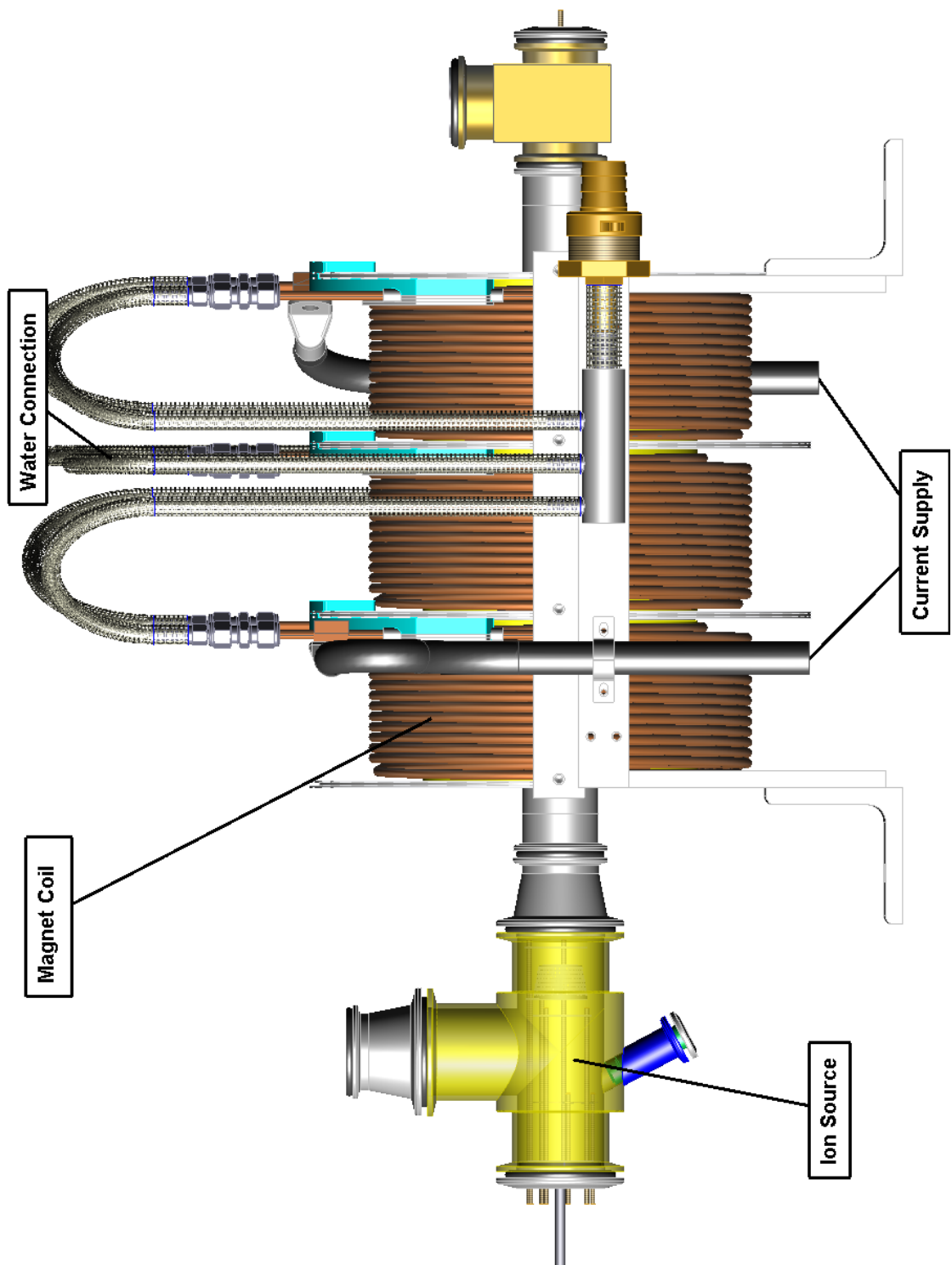


Figure 6.3: Drawing of Ion Source with Magnet

# Bibliography

- [Abd04] Abdurashitov, J. N., et al., 1994, Physics Letters B, 328, 234
- [Alt03] C.Weinheimer, Laboratory Limits on Neutrino Masses - G. Altarelli and K. Winter (Neutrino Mass, Springer 2003)
- [Bar98] R. Barate et al. (Eur. Phys. J. C2 395, 1998)
- [Bau07] Magnet coil from Helmut Baumeister
- [Beg08] Slow Control from Armen Beglarian (2008)
- [Bla07] The Nano Wire Field Emission Point Array - Klaus Blaum (University of Mainz, 2007)
- [Bo07a] Determination of neutrino mass from tritium beta decay - Beate Bornschein (Institute for Technical Physics, Tritium Laboratory Karlsruhe - 2007)
- [Bo07b] Status of the KATRIN tritium source - Beate Bornschein (Talk at TransRegio SFB 27, July 2007)
- [Bro04] The Physics and Technology of Ion Sources - Ian G. Brown (Wiley-VCH, 2004)
- [Dav93] Quantum Efficiency Measurements of a Copper Photocathode in an RF Electron Gun - P. Davis et al. (Electrical Engineering Department, UCLA, 1993)
- [Dav94] R. Davis (Prog. Part. Nucl. Phys., Vol. 32, pp. 13-32, 1994)
- [Egu04] K. Eguchi et al. (Phys.Rev.Lett. 92, 071301, 2004)
- [Eic06] CPS Specification: Basic Requirements and Input Data from TRAP - F. Eichelhardt & O. Kazachenko (2006)
- [Eic08] F. Eichelhardt (Dissertation, 2008)
- [Eid04] S. Eidelman et al. (Physics Letters B592, 1, 2004)
- [Fuk06] M. Fukugita et al. (*astro-ph/0605362 v1*, 2006)
- [Gel79] Supergravity - M. Gell-Mann, P. Ramond, R. Slansky (North Holland, Amsterdam, Editors P. van Nieuwenhuizen, D. Freedman, 1979)
- [Gli06] Background from positive ions - Ferenc Glück (Talk at Collaboration Meeting, September 2006)

## Bibliography

- [Glü07] Positive ions and dipole electrodes in DPS2-F - Ferenc Glück (Talk at Collaboration Meeting, October 2007)
- [Glü08] Personal conversations with and calculations from Ferenc Glück during the experiment (IK FZK, 2008)
- [God67] Faraday cup and secondary-emission monitor calibration - T.F. Godlove, M.E. Toms, D. W. Jones and K.M. Murray (Nuclear Physics Division, U.S. Naval Research Laboratory Washington, D.C., 1967)
- [Ham99] W. Hampel et al. (Physics Letters B 447 1999 127-133, 1999)
- [Han04] Neutrinos in Cosmology - S. Hannestad (2004)
- [Han06] S. Hannestad (*astro-ph/0607101 v1*, 2006)
- [Hor07] Technical Drawings from the Group of S. Horn (Institut für Kernphysik, FZK, October - December 2007)
- [Jac02] Klassische Elektrodynamik - John David Jackson (de Gruyter, 2002)
- [KAT04] KATRIN Design Report (2004)
- [Kaw84] Generation of relativistic photoelectrons induced by excimer laser irradiation - Y. Kawamura, K. Toyoda, M. Kawai (Appl. Phys. Lett. 45 (4), 1984)
- [Kaz07] Internal KATRIN Document about the TILO experiment - Dr. O. Kazachenko, Norbert Kernert, Frank Eicherhardt, Michael Sturm (2007)
- [Kie66] Electron Impact Ionization Cross-Section Data for Atoms, Atomic Ions, and Diatomic Molecules: I. Experimental Data - L.J. Kiefer, Gordon H. Hunn (Reviews of Modern Physics, Vol. 38, No.1, January 1966)
- [Kla04] H.V. Klapdor-Kleingrothaus, I.V. Krivosheina, A. Dietz, O. Chkvorets (Physics Letters B586, 198-212, 2004)
- [Liu04] Ionization of Molecular Hydrogen - Xianming Liu and Donald E. Shemansky (The Astrophysical Journal, 614: 1132–1142, 2004 October 20)
- [Lot04] Lampenspektren und Bestrahlungsstärke - Datasheet from the Lot-Oriel website ([www.lot-oriel.com](http://www.lot-oriel.com), 2004)
- [Lot07] Pen-Ray Line-Emitter - Datasheet from the Lot-Oriel website ([www.lot-oriel.com](http://www.lot-oriel.com), 2007)
- [Moh02] Lectures on Theoretical Aspects on Neutrino Masses and Mixings - R.N. Mohapatra (ICTP, 2002)
- [Pau30] Letter to the Physical Society in Tübingen (4. Dezember 1930) - W. Pauli (printed in L.M. Brown, Phys. Today 31 (1978), 23)

- [PDG04] Particle Physics Booklet - Particle Data Group (Extracted from the Review of Particle Physics, S. Eidelmann et al., Phys. Lett. B592, 1, 2004)
- [Rab97] Neutrino Masses, How to add them to the Standard Model - S. Raby, R. Slansky (Los Alamos Science Number 25, 1997)
- [Rei59] Phys. Rev. 113 (1959), 273 - F. Reines and C.L. Cowan (1959)
- [Rin05] A. Ringwald (*hep-ph/0505024 v1*, 2005)
- [Sch83] A capillary discharge tube for the production of intense VUV resonance radiation - G. Schönhense, U. Heinzmann (J. Phys. E: Sci. Instrum., Vol. 16, 1983)
- [Sch97] Neutrino-physik - N. Schmitz (Teubner Verlag, 1997)
- [Sel04] U. Seljak (Phys. Rev. D71 103515, 2005)
- [SNO02] Direct Evidence for Neutrino Flavor Transformation from Neutral-Current Interactions in the Sudbury Neutrino Observatory - The SNO Collaboration (Phys. Rev. Lett. volume 89, No. 1, 011301, 2002)
- [Stu07] Bestimmung der Tritiumflussreduktion einer Tritium-Argon-Frostpumpe für das Neutrino-massenexperiment KATRIN - Michael Sturm (Diplomarbeit, Januar 2007)
- [Thü07] Präzisionsüberwachung und Kalibration der Hochspannung für das KATRIN-Experiment - Thomas Thümmler (Dissertation, 2007)
- [Tra83] Electron Scattering by Molecules II. Experimental Methods and Data - S. Trajmar, D.F. Register, A. Chutjian (Physics Reports, Review Section of Physics Letters, 97, No. 5219-356, 1983)
- [Ubi08] Development of a non-destructive Fourier Transform-Ion Cyclotron Resonance detection system for KATRIN - Marta Ubieto Diaz (Diploma thesis, September 2008)
- [Vac07] Vakuumschaugläser - Excerpt from the Vacom Product Catalogue (*www.vacom.de*, 2007)
- [Val08] Personal Email from Kathrin Valerius (April 2008)
- [Vog95] Gerthsen Physik - H. Vogel (Springer, 18. Auflage, 1995)
- [Wol95] Handbook of Ion Sources - Bernhard Wolf (CRC Press, 1995)
- [Yan78] T. Yanagida (Prog. Th. Physics B135 (1978) 66, 1978)
- [Yao06] W.-M. Yao et al. (*http://pdg.lbl.gov*, Particle Data Group, J. Phys. G 33, 1, 2006)

## *Bibliography*

# Acknowledgment (Danksagung)

Der erste Dank gebührt natürlich Prof. Dr. Christian Weinheimer und Prof. Dr. Guido Drexlin dafür, dass sie die Mühe auf sich genommen haben diese Arbeit organisatorisch überhaupt zu ermöglichen.

Da unmittelbar am Gelingen dieser Arbeit beteiligt, gilt ein eigener Dankesausspruch dem Team um Dr. Beate Bornschein. Das unkomplizierte Arbeitsklima, der stete Rat und die Hilfsbereitschaft sind namentlich zu verdanken: Dr. Oleg Kazachenko, Dr. Strahinja Lukic, Norbert Kernert (auch nochmal für meine allererste Übernachtung in Karlsruhe!), Michael Sturm, Frank Eichelhardt und Aleksandra Gotsova. Ganz besondere Anerkennung meinerseits hat sich Dr. Beate Bornschein selbst verdient für die intensive Betreuung und die unglaublich lehrreiche Zeit, die sie mir immer wieder bescherte.

Der Aufbau und die Durchführung des Experiments wären ohne die Erfahrung und Ideenreichtum der Teams um Siegfried Horn und Hans Skacel sicherlich nicht gelungen. Vielen Dank für die Unterstützung, nicht nur durch technische Zeichnungen, sondern auch durch permanente Bereitschaft zu Rat und Tat!

Absichtlich einzeln erwähne ich an dieser Stelle meinen ganz besonderen Tischnachbarn Dr. Ferenc Glück, von dem man nicht nur viel über Physik lernen kann.

Für die scharfsinnige und wiederholte Durchsicht dieser Arbeit geht eine eigene Dankeseile an: Dr. Beate Bornschein, Dr. Thomas Thümmler, Dr. Ferenc Glück und Marie-Christine Kauffmann.

Privater Dank für private Kurzweil in Karlsruhe: Dem Black Rebel Motor Gourmet Club, d.h. Adam, Adrian und Marie, für die gemeinsame Erfahrung der kulinarischen Errungenschaften regionaler und internationaler Küchen. Außerdem ganz besonders an Sponge-Markus für alle Arten und Unarten von Kultur (und nur wenig Physik).

Der Zustand dieser abgeschlossenen Diplomarbeit geht jedoch noch auf weit frühere Begebenheiten zurück ohne die alles Wesentliche anders wäre. Eine Gewichtung der zugehörigen Menschen ist da ziemlich sinnlos, eine alphabetische Reihenfolge etwas weniger: André, Andrea, Angelika, Christina, Daniel, Flo, Henry, Holger, Jan, Julia, Katharina, Malte, Thorben - die teilweise ihren Beitrag vielleicht gar nicht erkennen und es zusammen auf geschätzte 142 Jahre Freundschaft bringen. Nicht zu vergessen sind diejenigen, die hier nicht genannt wurden.

Der letzte Dankesausspruch geht an meine Familie, besonders meine Eltern, die das Studium und die Diplomarbeit auf einer viel grundsätzlicheren Ebene überhaupt erst ermöglicht haben und deren Unterstützung an Selbstaufgabe grenzt.